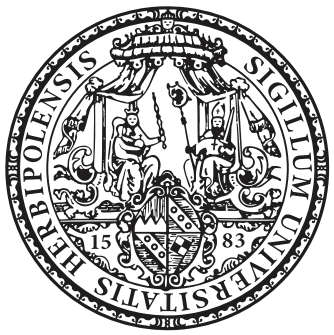

Characterization of Novel Magnetic Materials: Ultra-Thin (Ga,Mn)As and Epitaxial-Growth MnSi Thin Films

Dissertation

zur Erlangung des
naturwissenschaftlichen Doktorgrades
der Julius-Maximilians-Universität Würzburg

vorgelegt von
Jennifer Anne Constantino
aus Manila \ Philippinen

Würzburg 2013

Eingereicht am: December 10, 2013

bei der Fakultät für Physik und Astronomie

1. Gutachter: Prof. Dr. Laurens W. Molenkamp

2. Gutachter: Prof. Dr. Matthias Bode

der Dissertation

Vorsitzende(r)

1. Prüfer: Priv.-Doz. Dr. Charles Gould

2. Prüfer: Prof. Dr. Matthias Bode

3. Prüfer: Prof. Dr. Reinhold Oppermann

im Promotionskolloqiums

Tag des Promotionskolloquiums: January 21, 2014

Doktorurkunde ausgehändigt am: ...

Contents

Zusammenfassung

Um einerseits ein fundamentales Verständnis magnetischer Wechselwirkungen zu erhalten und andererseits neue Effekte für zukünftige Anwendungen zu finden, ist es entscheidend, magnetische Phasen spintronischer Materialien zu untersuchen. In dieser Arbeit fokussieren wir uns auf grundlegende elektrische und magnetische Transporteigenschaften zweier Materialsysteme. Das sind zum Ersten ultradünne (Ga,Mn)As Filme mit parabolischen Dotierprofilen, und zum Zweiten epitaktisch gewachsene Dünnschichten aus MnSi, einem helimagnetischen Metall, dessen Entwicklung seit Kurzem in unserer Gruppe vorangetrieben wird.

In dem ersten Teil dieser Arbeit konzentrieren wir uns auf die magnetischen Anisotropien in ultradünnem (Ga,Mn)As mit neuartigem parabolischen Dotierprofil unter Einfluss eines von Außen angelegten elektrisches Feldes. Ziel ist es, die magnetischen Eigenschaften während des Metall-Isolator Übergangs zu untersuchen. Dieser wird durch eine Ladungsträgerverarmung hervorgerufen, die wiederum durch das elektrische Feld gesteuert werden kann. Um ein grundlegendes Verständnis für den ferromagnetischen Halbleiter (Ga,Mn)As zu erhalten, betrachten wir seine strukturellen und magnetischen Eigenschaften (z.B. magnetische Anisotropien). Das ultradünne Wachstum resultiert letztlich in einer magnetokristallinen Anisotropie. Weiterhin geben wir auch einen Einblick in die Transporteigenschaften von (Ga,Mn)As während des Metall-Isolator Übergangs und einen kurzen Überblick über Leitwertfluktuationen in diesem Materialsystem aus früheren Arbeiten.

Um eine Ladungsträgerverarmung zu erreichen, ist es notwendig die ultradünnen (Ga,Mn)As Schichten zu *gaten*. Hierfür verwenden wir eine Halbleiter p-n Tunnelbarriere. [Owen 09] Die verwendeten Proben bestehen aus einer makroskopischen Hall Struktur, sowie aus einer Corbino Struktur für Vierleitermessung, und sind jeweils mit einem DC-*Back Gate* ausgestattet. Die Magnetowiderstandsmessungen an der Hall Struktur wiesen verstärkt Beiträge der harten uniaxialen Achsen auf. Dies deutet darauf hin, dass die Probe nahe am *Hopping*-Regime und somit nahe an dem Metall-Isolator Übergang ist. [Rush 06, Jung 06] Wir beobachten eine monotone Veränderung der uniaxialen Beiträge, die auf eine verringerte Asymmetrie zwischen den uniaxialen harten Achsen zurückzuführen ist. Außerdem fällt auch das Hall-Signal mit steigender Gate-Spannung ab. Auch dieses Verhalten ist konsistent mit Proben, die sich dem nicht-magnetisch isolierenden Zustand

nähern.[Ohno 00]

Die Vierleiter Corbino Struktur ist geeignet, um die rein kristallinen Beiträge des Magnetowiderstands zu isolieren. In der verkleinerten Struktur werden die Leitwertfluktuationen deutlich sichtbar und sie beeinflussen letztlich das magnetische Verhalten des Materials. Der *in-plane* und *out-of-plane* Magnetowiderstand zeigt nicht monotone Veränderungen der uniaxialen Beiträge zur Anisotropie. Dies widerspricht dem linearen Verhalten der größeren Hallstrukturen. Entlang der uniaxialen Achse können diese Fluktuation auch durch das *Gate* beeinflusst werden. Thermisch hervorgerufene Alterungseffekte zeigen zudem, dass die Fluktuationen stark von der Störstellenkonfiguration abhängen.

Ein Nebenprojekt (Kapitel 4) beschäftigt sich mit dem Thema, einen größeren *Gate*-Spannungsbereich für zukünftige Messungen zu erreichen. Hierfür wird ein epitaktisches Lift-off-Verfahren verwendet, das es ermöglicht, die Kompatibilität verschiedener *Gate*-Barrieren mit (Ga,Mn)As zu testen. Wir konzentrieren uns auf paraelektrisches Strontiumtitanat (STO), das auf hochdotiertem Si gewachsen wird. Bei vom Substrat gelösten Schichten beobachteten wir Änderungen der magnetischen Anisotropie und des Magnetotransports, die durch die Relaxation hervorgerufen werden. Bei den verwendeten Transferprozessen bleiben die grundlegenden magnetischen Anisotropien des verwendeten 70 nm Films allerdings unverändert. Unglücklicherweise scheint die STO/Si Grenzfläche basierend auf Berechnungen und Messungen - eine Leitungsband-Diskontinuität nahe Null aufzuweisen.[Cham 01]

Im zweiten Teil dieser Arbeit behandeln wir die Charakterisierung von epitaktisch gewachsenen MnSi Dünnschichten, die in unserer Gruppe entwickelt wurden. Das ferromagnetische Übergangsmetall MnSi ist mit seiner nicht kollinearen Spinstruktur und seinen topologischen Transporteigenschaften sowohl für das fundamentale Verständnis von Effekten wie dem anomalen Hall Effekt (AHE) [Naga 10], als auch für Anwendungen wie bspw. *Spin-Transfer-Torques* mit geringer Stromstärke, von Interesse. [Joni 10] Epitaktisch gewachsene MnSi Filme sind dabei erst vor kurzem in den Fokus des Interesses gerückt [Karh 10]. Zunächst wird eine kurze Einführung in das Material gegeben (Kapitel 5), wobei wir uns hier auf die Transporteigenschaften und die Entstehung von Skyrmionen konzentrieren. Letztere sind topologische Spinstrukturen, die jüngst großes Interesse hervorgerufen haben [Fert 13]. Charakterisierungsmessungen an unserem Material zeigen Übereinstimmung mit verfügbaren Literaturwerten von MnSi Volumenmaterial und Dünnschichten. Dies bestätigt somit ein erfolgreiches Wachstum. Die etablierten Messungen werden auch in Zukunft zur Charakterisierung von MnSi Dünnschichten in unserer Gruppe genutzt.

Abschließend untersuchen wir die Transporteigenschaften der gewachsenen MnSi Filme in Abhängigkeit eines Magnetfeldes entlang verschiedener Kristallrichtungen. Wir beschränken unsere Analyse auf zwei MnSi Schichten mit unterschiedlichen Dicken (12 nm und 20 nm). In Kapitel 7 vergleichen wir die Hall Parameter und die topologischen Hall Signale mit Ergebnissen des Volumenmaterials. Dabei legen wir besonderes Augenmerk

auf die anomale topologische Komponente des Hall Effektes. Bei beiden Filmen weisen die Ergebnisse für den normalen Hall Effekt eine qualitative Übereinstimmung mit den Resultaten für MnSi Volumenmaterial auf. Es wird jedoch eine größere anomale Hall-Komponente für die dünnere Schicht beobachtet. Dies könnte durch veränderte Spin-Spin Wechselwirkungen [Enge 12], erhöhte lokale Beiträge zum Hall Effekt für dünne Schichten [Gerb 02] oder die Netto-Chiralität [Tata 02] erklärt werden. Allerdings tritt für den dünneren Film ein Vorzeichenwechsel auf, der möglicherweise durch Änderungen in der Bandstruktur, einhergehend mit einer Beeinflussung der Spinpolarisation, hervorgerufen wird [Jeon 04, Li 13].

Neben dem angelegten Feld wurden auch weitere Parameter variiert,um die Magnetisierungsstruktur in den gewachsenen Schichten zu untersuchen. *Minor-loop* und Temperaturmessungen wurden ebenfalls durchgeführt, um die besondere Dynamik der Magnetisierung und die Phasen in den MnSi-Dünnschichten zu verstehen. Dabei zeigen die *Minor-loop* Messungen das Vorhandensein mehrerer Magnetisierungszustände mit unterschiedlichen Relaxations- und Sättigungsparametern in der 20 nm Schicht [Wind 12]. Die Temperaturmessungen weisen auch Besonderheiten im Hall Signal bei $T \approx 10$ K und nahe der Curietemperatur ($Tc \approx 45$ K) auf. Dies deutet auf eine verbreiterte A-Phase, wie sie auch etwa in dünnen MnSi Scheiben [Tono 12] und für epitaktische Schichten [Li 13] zu finden ist, hin. Dies muss aber durch weitere Messungen verifiziert werden.

In Kapitel 8 untersuchen wir das Magnetisierungsverhaltens in kleinen *in-plane*-Magnetfeldern. Hierfür werden longitudinale Magnetowiderstandsmessungen und planare Hall Messungen an MnSi-Filmen durchgeführt. Die Magnetowiderstandsmessungen zeigen spinglasartiges Verhalten für die 20 nm Schicht, das möglicherweise durch das Vorhandensein beider chiraler Domänen innerhalb des Films herrührt. [Karh 10] Aufgrund der Form-Anisotropie ist es mit Magnetowiderstandmessungen nicht möglich, die Effekte der unterschiedlichen berechneten uniaxialen Anisotropien beider Filme zu detektieren [Baue 12]. Sie können möglicherweise dennoch, bei geringen magnetischen Feldstärken, die Unterschiede der verschiedenen Typen magnetischer Domänen aufzeigen. [Mori 85] Es wird gezeigt, dass der planare Hall Effekt eine zum angelegten Feld antisymmetrische Komponente aufweist, die eventuell durch einen Hall Term zweiter Ordnung entsteht (Umkehr Effekt). Dieser könnte aus der Spin-Chiralität und der Kristallsymmetrie des Systems hervorgehen und weitere Beiträge zum anomalen Hall Effekt leisten [Mudu 05, Frie 06].

Summary

The study of magnetic phases in spintronic materials is crucial to both our fundamental understanding of magnetic interactions and for finding new effects for future applications. In this thesis, we study the basic electrical and magnetic transport properties of both epitaxially-grown MnSi thin films, a helimagnetic metal only starting to be developed within our group, and parabolic-doped ultra-thin (Ga,Mn)As layers for future studies and applications.

In the first part of this thesis we focus on the study of the magnetic anisotropies in ultra-thin (Ga,Mn)As with a novel parabolic doping profile and the effects of an applied electric field. The main goal is to observe the magnetic properties of the material as it is driven to the metal-insulator transition by charge depletion. The first section introduces the ferromagnetic semiconductor (Ga,Mn)As and its properties, focusing particularly on the concepts important for this work. Aside from basic information regarding its structural and magnetic properties (e.g. magnetic anisotropies), we describe the effects of ultra-thin growth of this material on the magnetocrystalline anisotropy. We also look at the behavior of its transport properties as it is driven through the metal-insulator transition and also give some detail on previous work on conductance fluctuations in (Ga,Mn)As.

For our work on electrical gating of ultra-thin (Ga,Mn)As, we use an all-semiconductor p-n tunnel barrier.[Owen 09] We used both standard macroscopic Hall bar and four-terminal Corbino structures for our measurements with DC back-gate. Our experiments on the Hall bar device have shown increased contributions by the hard uniaxial anisotropies in magnetoresistance measurements. This is consistent with transport properties of samples near the hopping regime and in the vicinity of the metal-insulator transition.[Rush 06, Jung 06] Monotonic change is observed in the uniaxial contributions for the large Hall bar structure, showing decreasing asymmetry between the uniaxial hard axes. For Hall measurements, we also see monotonic decrease in the Hall signal as the gate voltage is increased, again consistent with the sample being driven closer to the non-magnetic insulating state.[Ohno 00]

We also make use of a four-terminal Corbino structure to extract pure crystalline contributions to the magnetoresistance. Reducing the dimension of the device is shown to drive the system into a conduction regime wherein the fluctuations become prominent and finally affect the magnetic behavior of the material. The magnetoresistance (in-plane and

out-of-plane) measurements show non-monotonic changes in the uniaxial contributions to the anisotropy for the small structures, compared to the linear resistance increase with applied gate voltage in the larger Hall bar structure. The fluctuations are also shown to exhibit gate effects along the uniaxial magnetic hard axes and heavily influenced by the impurity configuration of the material as shown by aging effects after thermal cycling.[Papp 06]

As a side study (Chapter 4) intended for increasing gate voltage range in future work, epitaxial lift-off was used to test the compatibility of different gate barriers, in our work the paraelectric Strontium Titanate (STO) grown on highly doped n-type Si, with(Ga,Mn)As. We observed changes in the magnetic anisotropies and magnetotransport for lifted-off layers due to strain relaxation, but the process used to transfer the free-standing film preserved the basic magnetic anisotropies of the 70 nm films used in the fabrication process. Unfortunately, the STO/Si interface appears to have near-zero conduction band discontinuity from calculations and experiment.[Cham 01]

For the second half of this work, we concentrate on characterizing epitaxially-grown MnSi thin films being developed in our group. Itinerant ferromagnetic metal MnSi, with its non-collinear spin structure and topological transport properties, is of interest for both fundamental understanding of concepts such as the anomalous Hall effect (AHE) [Naga 10] and applications such as low-current spin transfer torque [Joni 10]. Epitaxially-grown MnSi films have only been recently the focus of new interest.[Karh 10] A short introduction is first given for the material (Chapter 5), focusing on transport properties and formation of Skyrmions, topological spin structures currently subject of intense interest for applications.[Fert 13] Preliminary data analyzing material properties of the grown thin film MnSi within our group prior to transport measurements are discussed in Chapter 6. We have shown that extracted parameters from our thin films are consistent with available MnSi bulk and thin film literature values, supporting our work on growing MnSi thin films. This also establishes the basic list of techniques to be used for characterizing MnSi thin films grown by our group in the future.

Finally, we study the magnetotransport properties of the grown MnSi films with magnetic fields along different configurations and crystal directions. We focused our analysis on two grown MnSi films of different thickness (12-nm and 20-nm). In Chapter 7, the high field extracted Hall parameters and topological Hall signals are measured and compared to results from bulk, particularly focusing in the topological anomalous component of the Hall effect. The results for the ordinary Hall component show qualitative agreement with bulk MnSi results for both films. However, a larger anomalous Hall component is observed in the thinner film, which could possibly be explained by changes in the spin-spin interactions[Enge 12], increased local contributions to the Hall effect for thin films[Gerb 02] or the net chirality[Tata 02]. Extracted topological Hall values for both films are consistent with results from bulk[Neub 09a] and thin film results[Li 13]. However, a sign reversal is observed for the thinner film, possibly explained by changes in

bandstructure affecting the spin polarization.[Jeon 04, Li 13]

Aside from the applied field, other parameters were also changed to further characterize the magnetization structures within the grown films. Minor loop and temperature measurements were also performed to understand the interesting magnetization dynamics and phases in the MnSi thin films. Minor loop measurements show the presence of multiple magnetization states with different relaxation and saturation parameters within the 20-nm film.[Wind 12] Temperature measurements also show features in the Hall signal at $\approx$ 10K and near T_c ($\approx$ 45K), consistent with the broadened A-phase observed in [Tono 12] for thinned MnSi plates and in [Li 13] for epitaxial films, but should be confirmed by further measurements by other techniques.

Finally, low in-plane magnetic field characterization is also tested as a tool for probing the magnetization behavior in Chapter 8. Longitudinal magnetoresistance and planar Hall measurements are done for MnSi films. Magnetoresistance measurements show spin glass-like behavior for the 20-nm film, which could possibly arise from the presence of both chiral domain types within the film.[Karh 10] Magnetoresistance measurements are unsuccessful in detecting the effects of the different calculated uniaxial anisotropies of both films due to shape anisotropy effects [Baue 12], but possibly show the difference between the type of magnetic domains present within the films through low-field dependence.[Mori 85] The planar Hall effect or PHE is shown to have an antisymmetric component with the applied field, possibly arising from a second order Hall term (Umkehr effect), which could arise from spin chirality and crystal symmetry in the system and tied to additional contributions to the anomalous Hall effect.[Mudu 05, Frie 06]

Chapter 1

Introduction

Spin electronics or spintronics makes use of the spin degree of freedom of electrons or holes to manipulate the electrical properties of materials, wherein these two are strongly coupled. Ferromagnetic semiconductors (FS) and metals are such materials with this strong spin-charge coupling. Interest in FS stems from the possibility of combining ferromagnetic and semiconducting properties within the same device. This does away with the problems arising from incompatibilities between magnetic and electrical architecture in devices such as memory elements. Thus, the electrical control of the magnetic properties of these materials and vice versa are important in the development in integrated magnetic - semiconductor architectures. A prototype material is the diluted ferromagnetic semiconductor (DMS) (Ga, Mn)As. Recent developments in the study of this material include TAMR-based (Ga, Mn)As logic devices, wherein the magnetic state is accessed and modified through electrical currents.[Mark 11]

Because of the Zener double-exchange interaction between holes and the localized moments in (Ga, Mn)As, the magnetic properties of the material is sensitive to hole concentration. [Diet 00] A number of studies have been done establishing material behavior and microscopic processes within the metallic (Mn concentration = 2 –9%) and insulating ($\ll$ 1%) regimes. The metal-insulator transition (MIT) or hopping transport regime and its effects on the magnetic properties has not been explored fully, but has been suggested to contain a combination of regions of different magnetic character.[Sawi 10] The study of the magnetic phase transition and the material behavior in this regime for (Ga, Mn)As can be an interesting step in the fundamental understanding of the material and possibly DMS. It can provide fundamental insights into the electrical and magnetic processes within the material. With this knowledge, materials can be designed for better properties. This can also give ideas for future industrial applications.

Coupling ferromagnetism with other magnetic effects has also been of interest recently. For example, ferromagnetic/ferroelectric interfaces have been shown to modify the magnetic anisotropy of the ferromagnet through the magnetoelectric effect.[Duan 08] Aside

from epitaxial lattice-matched growth, the combination of different materials through methods such as epitaxial lift-off (ELO), with a thick sacrificial layer, may allow for such combinations.[Yabl 90] This technique has already been performed successfully in (Ga, Mn)As epilayers for observing strain effects on its magnetic properties.[Greu 11]

As the search for materials for future spintronic applications becomes more competitive, unconventional materials with characteristics such as non-collinear spin structures are being studied. Intermetallic compound MnSi have recently come to interest with the recent discoveries of novel non-Fermi liquid behavior at high pressures[Pfle 01] and predicted observation of Skyrmions in a small region near the magnetic transition (A-phase).[Mueh 09, Papp 09] This material has helical spin structure as its ground state. The spin helix is stabilized by the competition between normal exchange ferromagnetism and the Dzyaloshinskii-Moriya interaction due to the lack of inversion symmetry of its B20 crystal structure.[Mori 76]

It was only recently that the magnetic properties of these materials as thin films were first studied and has been shown have a richer magnetic structure than bulk.[Karh 10] The epitaxial growth introduces a strain which has been predicted to stabilize the magnetic Skyrmion lattice phase. Aside from benefits from the fundamental study of such structures, this promises device applications such as reduced current density requirements [Joni 10] and, based on predictions from bandstructure calculations[Jeon 04], possibly spin injection and detection.

The following chapters show the results of this work on two important materials, ferromagnetic semiconductor (Ga,Mn)As and weak itinerant ferromagnet MnSi.

In **Chapter 2 - 4**, details of our work on the electrical control of the magnetotransport properties of ultra-thin (Ga, Mn)As films near the metal-insulator transition are presented. After a brief introduction to the properties of ferromagnetic semiconductor (Ga,Mn)As particularly ultra-thin films near the metal-insulator transition, changes in the anisotropy and conductance fluctuations with respect to the Fermi level are analyzed. Some focus is also given on basic properties of the dielectric SrTiO3 (STO) used as substrate for epitaxially lifted-off bulk (Ga, Mn)As films)and results on the magnetic properties of epitaxial lift-off (ELO) bulk 70 nm (Ga, Mn)As films on quantum paraeletric STO.

Chapter 5 - 8 presents our work on MnSi thin films, particularly low-temperature magnetotransport data. A brief literature survey of properties weak itinerant ferromagnet MnSi is given, particularly focusing on anomalous magnetotransport behavior, and transport models used for analyzing the effects of the helical spin structure. We show in our results that magnetotransport can be possibly used to identify the existence of chiral

states in the MnSi.

Chapter 9 finally summarizes all the important results from this work and possible directions in the future.

Chapter 2

Diluted Ferromagnetic Semiconductor (Ga, Mn)As

The complete understanding of the properties of diluted magnetic semiconductors (DMS) has been of interest due to the possibilities of combining both electrical and magnetic functionalities for device applications. (Ga, Mn)As has been used as the prototype DMS material, with its properties well-studied in the metallic and insulating regimes. Control of the magnetic anisotropies of (Ga, Mn)As has been done with the application of an electrical gate with several techniques employed for fabricating the gated structures. In this chapter, we discuss the basic properties of the dilute ferromagnetic semiconductor (Ga,Mn)As to preface the following results.

2.1 Basic properties of (Ga,Mn)As

(Ga,Mn)As is a III-V dilute magnetic semiconductor with a zinc blende structure (Figure 2.1) with $E_{gap} \sim 1.5$ eV. Mn as a dopant (Mn^{2+} configuration and localized magnetic moment S = 5/2) substitutes a Ga atom, behaving as a shallow acceptor, or attaches itself to the unit crystal interstitially, acting as a double donor and reducing the hole concentration.[Yu 02, Edmo 04] As the Mn concentration is increased, Mn impurity levels sufficiently overlap to form a *metallic* ground state, where the hole states are delocalized.(Figure 2.1) For low doping concentrations (<<1%), the Mn is isolated with impurity binding energy of $E_a^0 \sim$113 meV and shows insulating character at low temperatures.

At Mn concentrations $\approx$ 1%, the material switches from insulating to metallic electrical behavior. Usually at 2% to 9% Mn concentrations the holes propagate quasifreely throughout the system. The first experimental observation of ferromagnetic (Ga,Mn)As was by [Ohno 96] and the theoretical description of (Ga,Mn)As, the p-d mean field Zener model, was developed by [Diet 00]. In this model, the Zener double-exchange magnetic interaction among holes and Mn moments create the hole-mediated ferromagnetism in

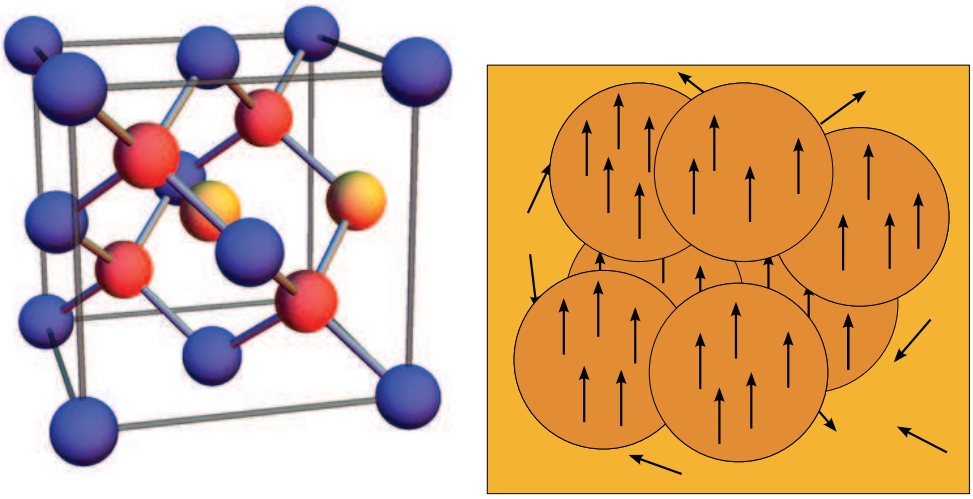

Fig. 2.1: Crystal structure and ferromagnetism in DMS (Ga,Mn)As. On the left is the (Ga,Mn)As unit crystal with Mn atoms (orange) occupying Ga sites (red) subsitutionally (Mn_{Ga}) or interstitially (Mn_I). As atomic positions are denoted by the blue spheres. On the right is the Zener picture of the (Ga,Mn)As metallic state wherein the free holes drive the Mn moments into a low energy long-range ferromagnetic state.[Diet 00] Images appropriated from [MacD 05]

(Ga,Mn)As.

The magnetic system of (Ga,Mn)As minimizes its energy by aligning its magnetization M along preferred directions. These preferred directions, due to the nature of the Mn wave function [Diet 01b, Schm 07], are anisotropic. (Ga,Mn)As layers under compressive strain (e.g. GaAs buffer with larger lattice constant) show in-plane magnetic easy axis, meaning the magnetization lies in-plane at zero applied field. Tensile strain (e.g. using an (In,Ga)As buffer with lattice constant $a_{GaAs} \geq a_{InGaAs}$) causes the strained layers to have an easy axes perpendicular to plane. Strain-free (Ga,Mn)As layers can be obtained through alternative methods such as epitaxial lift-off (ELO) [Yabl 87], where the (Ga,Mn)As layer is lifted off a sacrificial layer and deposited back onto a different carrier material. [Greu 11] studied the effects of transferring these released films onto different substrates[Yabl 90], resulting in changes in the magnetic anisotropies of the material, particularly the out-of-plane anisotropy.

The magnetic properties of the biaxial (Ga,Mn)As layer at low temperatures are dominated by two magnetic easy axes parallel to the (Ga,Mn)As [100] and [010] crystal directions, along with two weaker uniaxial second anisotropy components parallel to the [$\bar{1}$10] and [010] crystal directions [Papp 07b]. [Papp 07a] gives a phenomenological description of the anisotropy energy including all three anisotropy components as:

$$E = \frac{K_{cryst}}{4} sin^2(2\vartheta) + K_{uni[\bar{1}10]} sin^2(\vartheta - 135^{\cdot}) + K_{uni[010]} sin^2(\vartheta - 90^{\cdot}) - MH cos(\vartheta - \varphi), \quad (2.1)$$

where ϑ denotes the angle between magnetization and [100] crystal axis and φ is the angle between an applied magnetic field and [100]. The first term on the right hand side gives the biaxial anisotropy along the [100] and [010] crystal directions. The conversion from an anisotropy constant K to an anisotropy field is given by: $H_a = \frac{2K}{M}$. The second term in Equation 2.1 accounts for a much weaker uniaxial anisotropy term along a $[\bar{1}10]$ crystal direction [Sawi 04]. The third term stands for a small uniaxial anisotropy parallel to the [010] crystal direction [Goul 04]. All three anisotropy constants are temperature-dependent [Goul 07]. The last term $MHcos(\vartheta - \varphi)$ is the Zeeman term and accounts for the energy interaction between an external field and the internal magnetization of the sample.

(Ga,Mn)As also exhibits a strongly anisotropic magnetoresistance (AMR) [Edmo 03], where the resistivity $\rho_\perp$ for current flowing perpendicular to the direction of magnetization is greater than $\rho_\parallel$ for current along the magnetization [Baxt 02] (negative AMR). The sign of the AMR effect depends of the ratio between the effective strengths of the non-magnetic and magnetic scattering [Rush 09]. As a result of this anisotropy in the resistivity tensor, the longitudinal magnetoresistivity ρ_{xx} is given by [Jan 57, McGu 75]:

$$\rho_{xx} = \rho_\perp - (\rho_\perp - \rho_{||}) \cos^2(\vartheta), \tag{2.2}$$

where ϑ is the angle between the direction of magnetization and the current. Note that there is also a dependence of the resistivity on the angle between the direction of magnetization and the underlying crystal orientation [Rush 07]. For thin films however, a uniaxial crystalline term was shown to dominate the magnetic response.

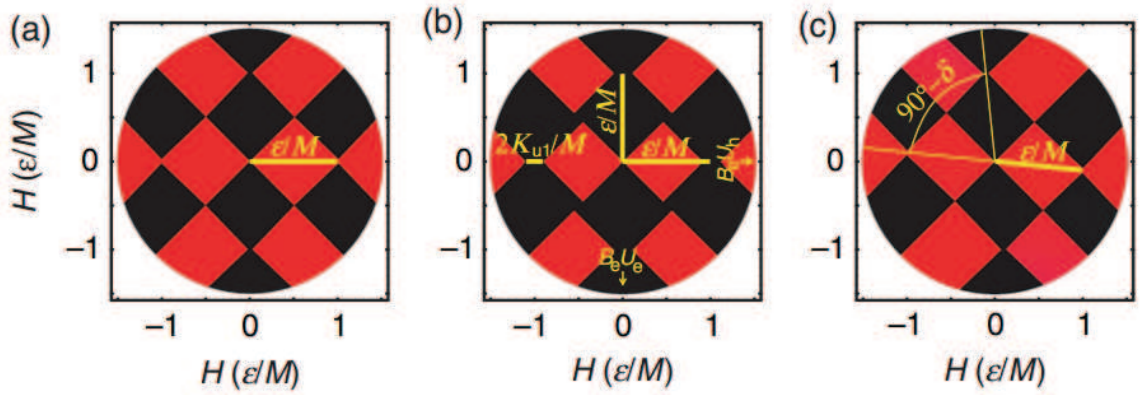

Fig. 2.2: Resistance polar plots for (a) purely biaxial (Ga,Mn)As with easy axies along the [100] (0°) and [010] (90°) directions, material with uniaxial anisotropy contribution along [010(b) and $[1\bar{1}0]$(c). Red denotes a high resistance state, while black represents a low resistance state. Image reprinted from [Papp 07b]

A way of visualizing these anisotropy terms was developed in [Papp 07a]. Sample resistance polar plots (RPP) for different collections of anisotropies are shown in Figure 2.2. In these plots, the innermost region (low-field) part is the most important for calculating the anisotropy strengths. This lower field region would form of a square with corners along the easy axis for a pure bixial anisotropy and the domain wall nucleation energy is calculated from the length of the half diagonal ϵ/M.(Figure 2.2.a) Figure 2.2.b shows the the model now including uniaxial terms, where the additional effects elongate the square into a rectangle. The strength of the uniaxial anisotropy constant in the $[\bar{1}10]$ direction $K_{\bar{1}10}$ (U_h) relative to the biaxial anisotropy constant K_{cryst} can be obtained from the angle δ (Figure 2.2.c).

With a uniaxial anisotropy term parallel to one of the biaxial easy axes (i.e. $K_u^{[010]}$, U_e), an asymmetry arises in the switching energy between the two biaxial easy axes. (e.g. the energy required to switch towards the easier of the two biaxial easy axis is less than to switch towards the second biaxial) [Goul 08] The ratio of $K_{cryst} : K_{110} : K_{010}$ is usually of the order of 100 : 10 : 1. [Papp 07b] This ratio can easily be modified via changing parameters such as hole concentration or temperature. [Sawi 04, Papp 07b]

2.2 Ultra-thin (Ga,Mn)As films

Because of increasing surface and finite-size effects, the behavior of ultra-thin films of many materials differ significantly from the bulk. [Rush 07] observed a marked difference of the AMR response between 5 and 25 nm (Ga,Mn)As layers showing an increased crystalline contribution to the magnetic response, particularly a large uniaxial component

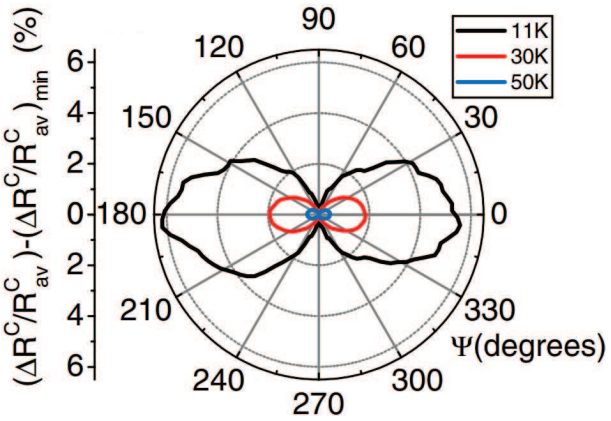

Fig. 2.3: Anisotropic magnetoresistance measurement for a device with Corbino geometry from a 5 nm (Ga,Mn)As film with 5% nominal Mn concentration. The applied field is maintained at saturation value and rotated along different angles. [Rush 07] used a phenomenological model to fit the magnetic response and found unaxial crystalline terms dominating the measured magnetoresistance, confirmed by this measurement. Reprinted from [Rush 07].

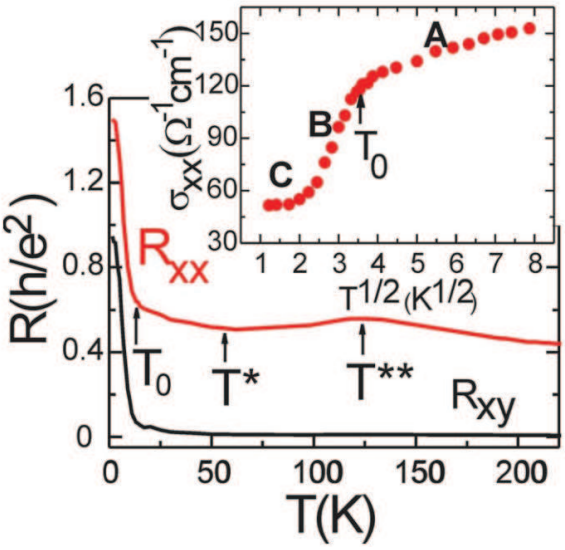

Fig. 2.4: Zero-field cooled temperature dependence of the longitudinal and transverse resistance for a 5-nm (Ga,Mn)As layer with 5% nominal Mn concentration. T^{**} indicates the maximum resistance before T_c, T^* the minimum metallic resistance and T_0 the characteristic temperature of the hopping conduction (see [Efro 75] and references therein). Reprinted from [Gare 10].

using their phenomenological model. (see Figure 2.3) They attribute this to the proximity of the material to the metal-insulator transition (MIT) with the anisotropic interactions increasing as the hole stay closer to the parent Mn ions.[Jung 06]

Giant magnetic response was also observed by Gareev et. al [Gare 10] on ultra-thin (Ga,Mn)As films in the insulating regime. The temperature dependence is shown in Figure 2.4. They attribute the large crystallographic plane-dependent AMR to the anisotropic spin-orbit interaction of localized magnetic clusters below the quantum transition, consistent with the analysis from [Rush 07].

2.3 Electrical Control of Magnetization in (Ga,Mn)As

Few works have been done so far in the electrical gating of (Ga,Mn)As, particularly due to the high carrier concentration ($\geq 10^{20}/\text{cm}^3$) in the material even at the lowest metallic doping regime, thus low gating efficiencies. The first gating experiments were done by Ohno et. al. and Chiba et. al on (Ga,Mn)As using top-gate geometry. [Ohno 00, Chib 03, Chib 06a, Chib 08] Figure 2.5 shows the experimental set-up used in their studies.

With an applied electric field, the magnetization of (Ga,Mn)As is rotated and changes with the hole concentration and consequently the density of states (DOS) of the material, following the hole-mediated Zener model of ferromagnetism in [Diet 00]. Wanting

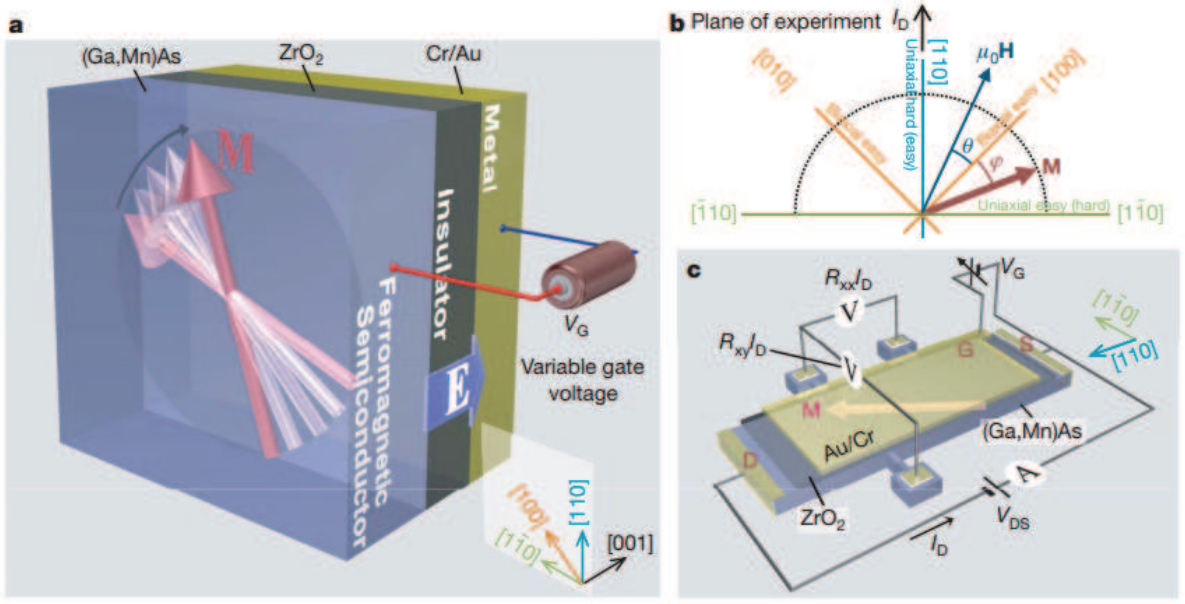

Fig. 2.5: Gating device and setup diagrams reprinted from [Chib 08]. (a) shows the rotation of the magnetization as a variable electric field is applied to the ferromagnetic material through a top-gate with (b) as guide to the notations on the plane of experiment. (c) shows a four-terminal Hall device used for the gating measurements in [Chib 08].

to increase the gating efficiency, an all-semiconductor p-n junction back-gate structure was proposed by [Owen 09], which uses a fully-semiconductor barrier composed of AlAs as p-type barrier and $Al_xGa_{1-x}As$ (x $\approx$ 30%) as n-type barrier. They used a 5-nm thin (Ga,Mn)As film with nominal concentration of $\approx$ 2%, placing it near the MIT and highly-doped n-type GaAs buffer layer for the back gate. They used a two-terminal Corbino structure to lower the contact resistance. They observed higher gating efficiencies, with low applied voltage increasing the channel resistance almost 200% from R(V_g = -1V). (see Figure 2.6)

A more comprehensive review of gating experiments in (Ga,Mn)As can be seen in [Diet 13]. We see that the (Ga,Mn)As magnetic state can be driven to near MIT through depletion of free holes within the system, consistent with the predictions in [Diet 00]. However, once near the quantum transition and localization playing a more dominant role in defining the magnetic interactions within the material, the transport picture and theories surrounding the transport mechanisms diverge from its metallic counterparts. (see: [Sheu 07] and [Diet 01b])

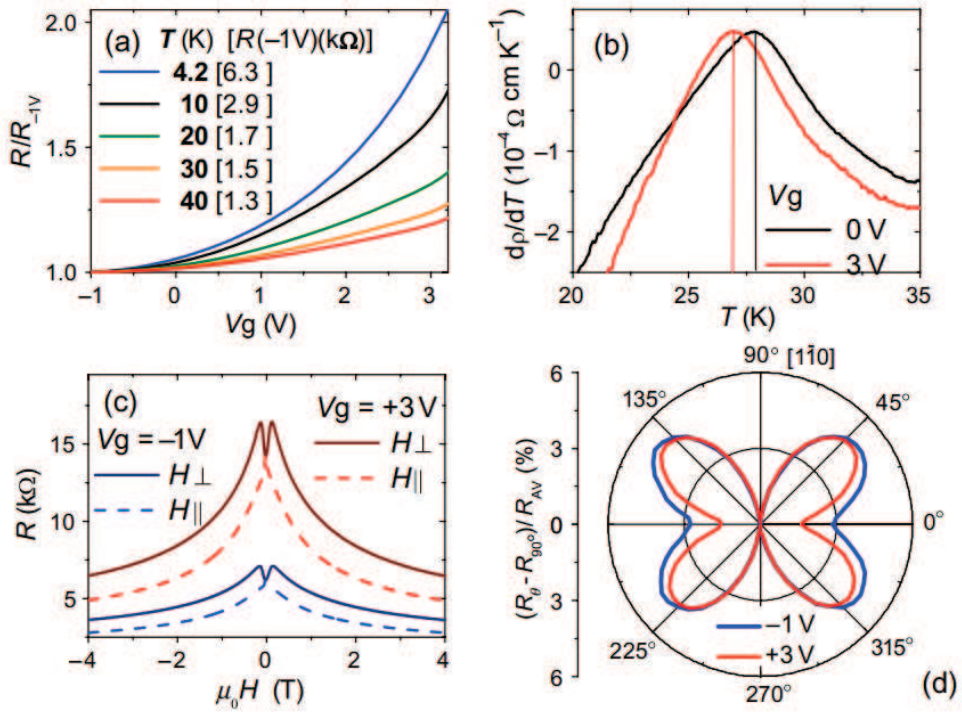

Fig. 2.6: Results from the low-voltage gating Corbino device from [Owen 09]. (a) shows the gate voltage dependence at different temperatures. (b) shows a change in the Curie temperature T_c with applied gate voltage. (c) shows the in-plane ($H_{\parallel}$) and out-of-plane ($H_{\perp}$) sweeps for V_g = -1V and +3V. (d) shows rotating in-plane AMR measurement at saturation field (4T) for V_g = -1V and +3V. Reprinted from [Owen 09].

2.4 (Ga, Mn)As and the Metal-Insulator Transition

As previously noted, the non-magnetic isulating and the ferromagnetic metallic states in (Ga,Mn)As are described by an array of different theories, most of which only deal with one particular conduction regime. In the insulating regime of (Ga,Mn)As, most treatments of the material focus on the isolated moments interacting via percolation and local fluctuations in the Mn binding energy [Sheu 07, Kami 02, Kami 03], while the metallic regime pictures a sea of free holes driving the moments into a low energy ferromagnetic state [Diet 00]. The transition between the ferromagnetic metallic regime and the non-magnetic insulating regime in (Ga,Mn)As is of interest for the purpose of reconciling these differing pictures. There is also interest in the Anderson-Mott transition ([Mott 68b, Mott 72, Abra 96]) and its effects on the magnetic correlations within the material.

Different approaches have been made in order to picture this magnetic phase in (Ga,Mn)As. Shown in Figure 2.7 is the structure used in [Papp 06] for tunneling anisotropic magnetoresistance (TAMR) observations in (Ga,Mn)As. In this experiment, they observed the

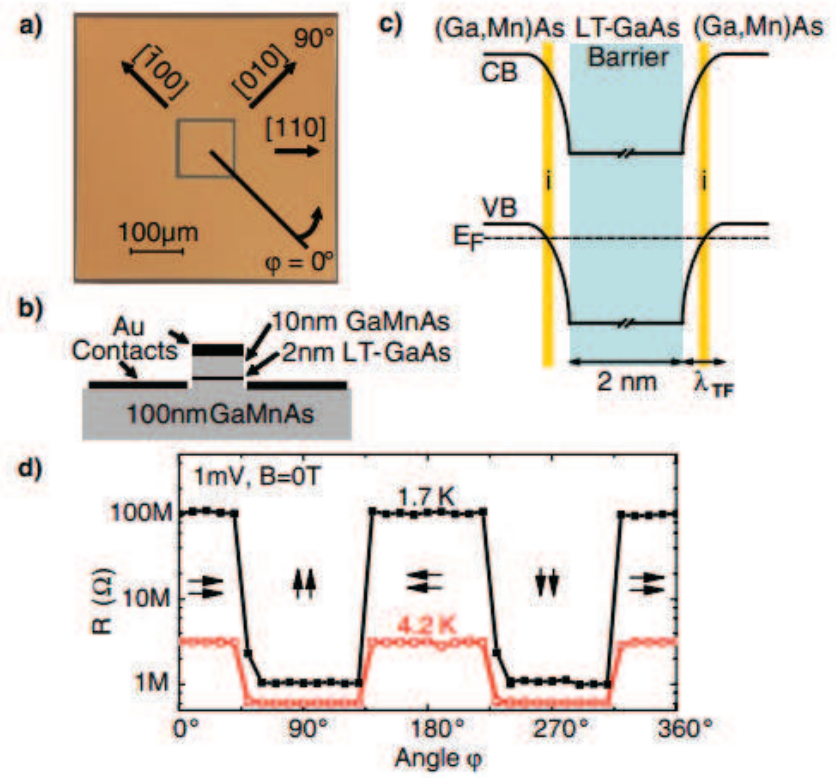

Fig. 2.7: TMR device used for magnetization-induced MIT switching in (Ga,Mn)As. (a) shows the crystal direction with respect to magnetic field direction used in the experiments, (b) the schematic diagram of the TMR device and (c) the material layers in the structure. The observed tunneling transport goes through a thin injection barrier near the MIT between the (Ga,Mn)As layer and the LT-GaAs. (d) shows the dependence of the tunneling behavior on the direction of the magnetic field with respect to crystal direction and the temperature. (4.2K and 1.7K) Reprinted from [Papp 06]

near-MIT behavior of a thin injection barrier formed between the (Ga,Mn)As layer and the low-temperature MBE grown GaAs (LT-GaAs) barrier layer.(Figure 2.7)

[Papp 06] showed in their work that a thin (Ga,Mn)As layer can be also be driven to the MIT via an applied magnetic field.(Figure 2.7) The magnetization facilitates the formation of an Efros-Shklovskii Coulomb gap (ES gap), where the DOS in the material forms a gap near the Fermi energy due to the Coulombic interaction between states. [Efro 75, Shkl 79] Calculations in [Schm 07] show that the extension of Mn bound hole state is modified by the application of a magnetic field along different crystal directions. The wavefunction overlap between the localized states determine the magnetic state of the material. This effect can also be used to explain the switching behavior observed in a junction between uniaxial (Ga,Mn)As nanobars, wherein different magnetization configurations between nanobars switch the junction from the metallic to hopping regime and

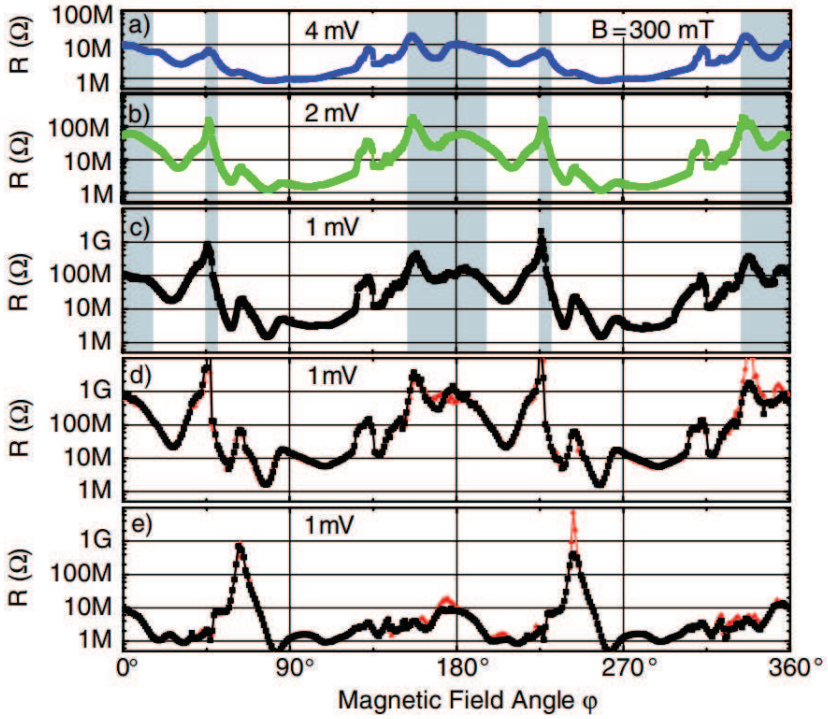

Fig. 2.8: Conductance fluctuations observed during cooling and thermal cycling of a GaMnAs/LT-GaAs/GaMnAs TMR structure used for measurements switching the (Ga,Mn)As layer through the metal-insulator transition by an applied magnetic field. The fluctation patterns change after a full thermal cycling, possibly due to changes in the impurity configuration of the system. Reprinted from [Papp 06].

vice versa.[Papp 07c]

Aside from a magnetization-driven ES gap arising from the anisotropy of the local moment wavefunctions in the TMR structure, reproducible conductance fluctuations were also observed.[Papp 06] (Figure 2.8) Thermal cycling changes the fluctuation distribution, suggesting change in the impurity configuration.[Papp 06] (see Figure 2.8) Unfortunately, no further analysis was done on these fluctuation within the study, citing the relative complexity of the relation of the Fermi level with respect to magnetization for (Ga,Mn)As.

Similar reproducible conductance fluctuations have been observed in other systems and usually attributed to the hopping transport regime. The distribution of these fluctuations have been modeled defining the "transparency" of the tunneling barrier and the random distribution of "punctures" or significantly large but widely-spaced fluctuations in the tunneling probabilities through the barrier.[Raik 87] Statistical analysis of the fluctuations in [Hugh 96] showed changes in the shape of fluctuation distribution function with respect to the geometry of the hopping path as the sample is driven by an electric field. (one or two-dimensional) They are attributed to non-averaging hopping paths within the

sample for mesoscopic systems.[Webb 86] These reproducible conductance fluctuations were also observed to occur for large metal-oxide-semiconductor samples [Popo 90], however no particular explanation was given as source of these observed transport signatures.

Another approach used to probe the MIT is by electrically driving the material through the MIT by hole depletion. [Diet 00] Sawicki et. al probed this magnetic state with global magnetization measurements (i.e. SQUID) using an applied electric field to deplete the material into the MIT.[Sawi 10] They observe, at the onset of localization, the formation of a superparamagnetic-like spin arrangement. As their (Ga,Mn)As channel is depleted, the material forms magnetic and non-magnetic regions. This is actually consistent with the multifractal clustering of metallic and insulating regions observed using Scanning Tunneling Spectroscopy (STS) on (Ga,Mn)As in [Rich 10]. The existence of both metallic and insulating regimes near the magnetic transition was also observed in magnetic field-dependent STS measurements on manganites, wherein they suggest that the transition should be viewed as a percolation of metallic ferromagnetic regions.[Fth 99] (see Figure 2.9)

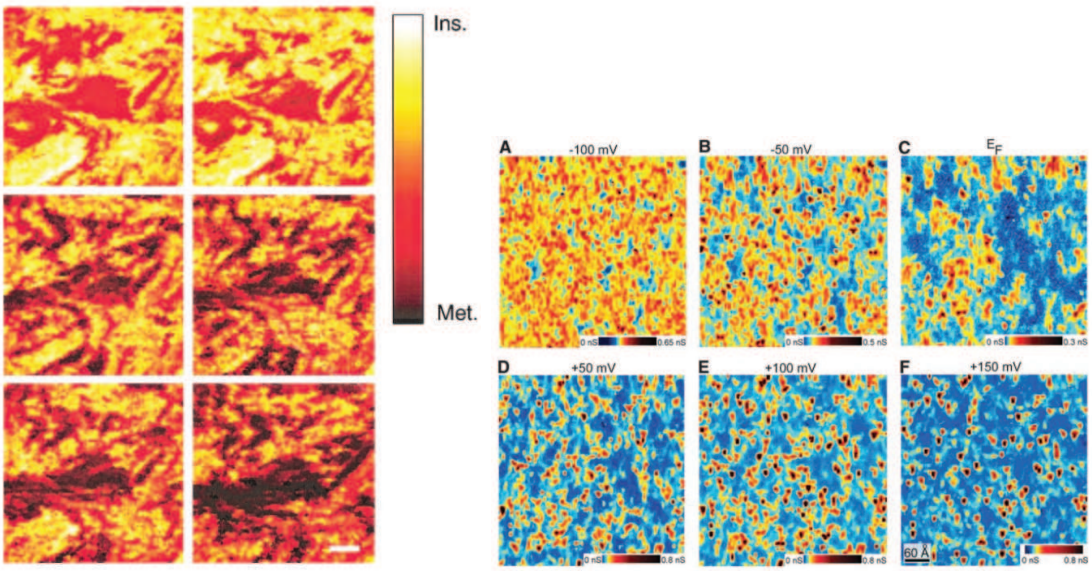

Fig. 2.9: Scanning tunneling spectroscopy measurements showing the formation of metallic and insulating regions within manganite $La_{1-x}Ca_xMnO_3$ (right)and (Ga,Mn)As (left). The manganite is driven near the ferromagnetic-paramagnetic state by heating near T_c and subjected to different magnetic fields where increasing metallic behavior is observed with increasing magnetization. In (Ga,Mn)As, increasing applied field changes the spatial variation in the LDOS, increasing the gaps between conducting states as the sample is driven to the MIT. STS measurements on the manganite taken from [Fth 99] and on (Ga,Mn)As reprinted from [Rich 10].

2.5 Summary

A brief introduction into the important concepts regarding (Ga,Mn)As and its basic properties and current state-of-the-art research shows the needed understanding for the following studies. In the next chapters, we discuss the results of electrical manipulation of ultra-thin (Ga,Mn)As films and discuss the magnetic behavior of such materials.

Chapter 3

Electric Control of Magnetization in Thin (Ga,Mn)As Layers

A number of studies have already explored the control of magnetic properties of (Ga,Mn)As by means of charge depletion.[Ohno 00, Chib 08, Owen 09] In this chapter, we show the results of our work in controlling the magnetotransport properties of ultra-thin (Ga,Mn)As grown in a novel way with a parabolic distribution of Mn dopants. We show that these layers show interesting magnetotransport behavior as they are driven closer to the metal-insulator transition (MIT) via an applied electric field.

3.1 Experimental Methods

The ultra-thin (Ga,Mn)As samples used for this study were grown by L. Ebel of EPIII using low-temperature molecular beam epitaxy (MBE) for (Ga, Mn)As growth on n-type GaAs (001).(Figure 3.1) The GaMnAs layer grown is parabolic-doped with ultra-thin (Ga, Mn)As layers grown in between thin GaAs spacer layers. The total thickness of the (Ga,Mn)As layers is $\approx$ 4 nm. The main advantage of this growth technique is the relatively low resistance of the film for its total thickness.($\mathcal{O}(10^5\Omega)$) After growth of a 200 nm Si-doped buffer layer, 10 nm AlAs and 10 nm $Al_xGa_{1-x}As$ (x = 0.3) layers are grown to serve as an all-semiconductor tunnel barrier for the gating experiments following Owen et. al.[Owen 09] (Figure 3.2)

The devices used for this study follow (1) the standard Hallbar geometry patterned using optical lithography and (2) the Corbino structure (diameter d = 16 μm with annular rings 1 μm in diameter) fabricated using electron-beam lithography techniques, both with back contacts on top of the conducting n-GaAs substrate. (Figure 3.3) The Corbino structure is used to eliminate the effect of current direction and directly extract crystalline contributions to the magnetoresistance.[Rush 07] For a detailed description of the process developed for defining the four-terminal Corbino structure using e-beam lithography, see

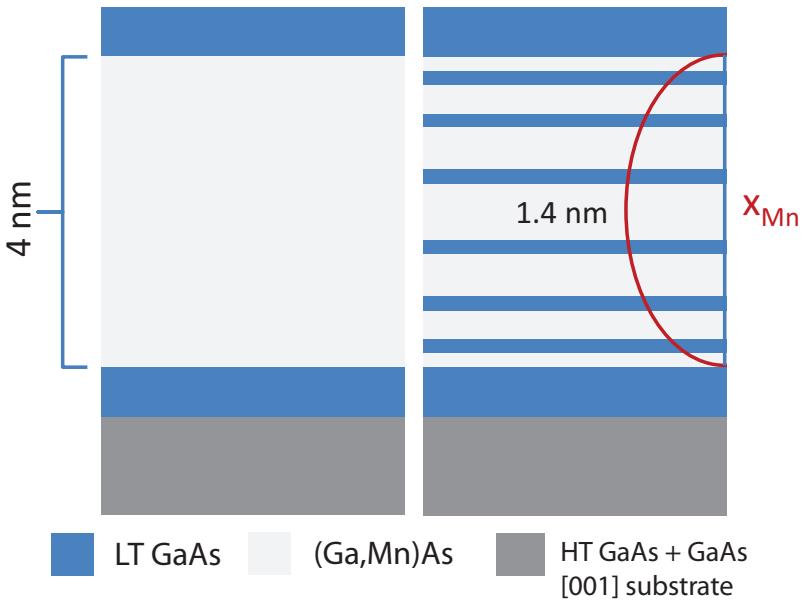

Fig. 3.1: Schematic diagram of the bulk 4-nm and parabolic-doped ultrathin (Ga,Mn)As layers. A total thickness of 4nm is calculated for the DMS region of the parabolic layer, with the highest doping concentration at the center (1.4 nm (Ga,Mn)As layer.) The samples are grown using low-temperature MBE.

appendix A. For the Hall bar, we used a layer with Mn concentration of $\approx 1.8\%$ and the Corbino $x_{Mn} \approx 2\%$, both values extracted by SQUID measurements. To test the electrical and magnetotransport properties of the sample, a He-cooled cryostat with an XYZ vector magnet with maximum resultant field of 300 mT is used. The AC measurements are done using a standard lock-in (EGG Stanford Research Systems Model 124 analog lock-in amplifier) setup at 13Hz.

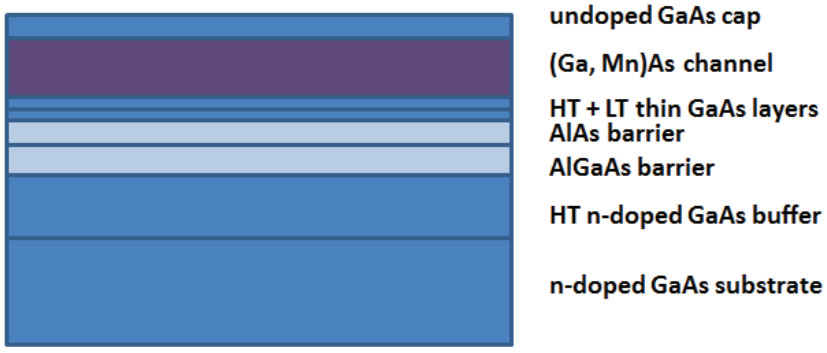

Fig. 3.2: Schematic diagram of the all-semiconductor p-n junction gating structure based on [Owen 09]. The (Ga,Mn)As channel in our experiments is the parabolic-doped (Ga,Mn)As layer.

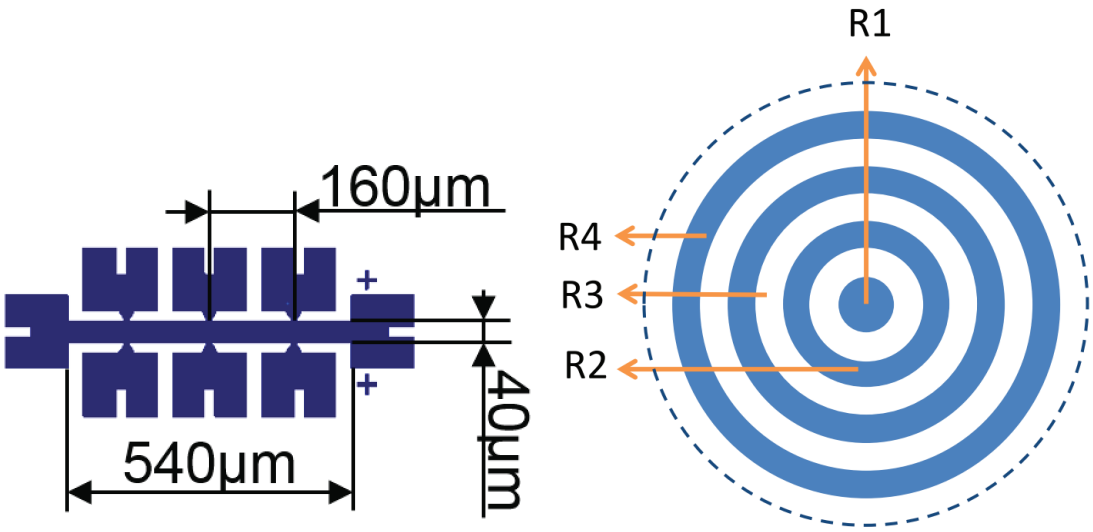

Fig. 3.3: Diagrams of the devices used for the gating experiments. On the left is the Hall bar mask used for optical lithography with dimensions. On the right is the four-terminal Corbino structure, where the current flows along R1 and R4 and the voltage drop is measured between rings R2 and R3. The rings and the mesa for the Corbino structure are all defined by electron-beam lithography.

3.2 Electrical control of magnetization in parabolic-doped (Ga,Mn)As thin films

3.2.1 Electrical Gating of Ultra-Thin (Ga,Mn)As

To test the material, zero-field cooling measurements were done to observe the temperature dependence of the parabolic layers and infer the transport mechanisms present in the material. The observed behavior (Figure 3.4) is consistent with [Gare 10], which places the parabolic samples near the MIT. The SQUID measurements show borderline metallic Mn concentrations, which somewhat supports this assertion. This temperature-dependence also means that the sample is at hopping transport and subsequent analysis of transport would focus on increased contributions of the uniaxial anisotropies, following [Rush 06, Rush 07].

As first electrical test for the gating structures, gate voltage sweep measurements were done to test the voltage range which can be applied through the barrier before a significant leakage current. For the Hall bar structure, the applied DC gate voltage is swept until 2V. (Figure 3.5) For the gating measurements using the Hall bar, the current is along $[\bar{1}10]$ (0°). Comparing the results with Owen, et. al, a similar change in resistance is observed for the Hall bar structure.[Owen 09]

The resistance response with applied gate voltage through the AlAs-AlGaAs tunnel bar-

rier junction for the Hall bar structure shows almost linear change until beyond 1.5V, wherein the leakage current seems to dominate the electrical measurement. A measurement of the leakage current is shown in Figure 3.6. The current through the sample is of the order 10^{-9} A, which places the leakage current at less than 1% at 1V gate. Extrap-

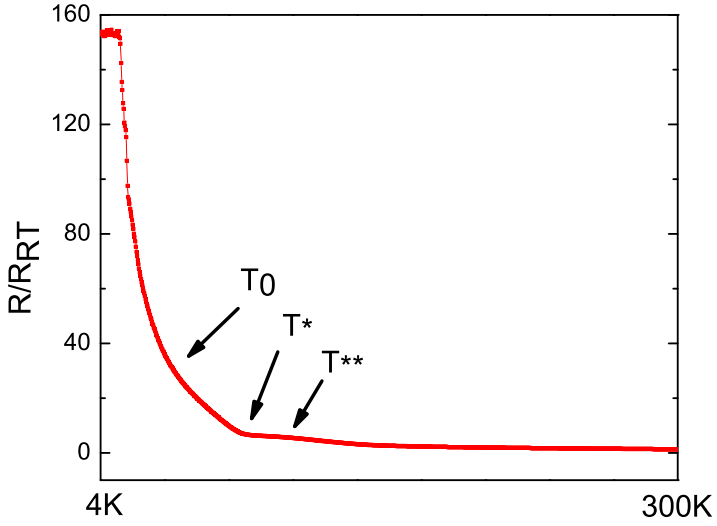

Fig. 3.4: Temperature dependence of the longitudinal resistance in a parabolic layer at ≈ 2% Mn concentration. The behavior is consistent with ultra-thin 5-nm thick samples from [Gare 10]. T^0 in their paper corresponds to the characteristic temperature of the MIT, T^* temperature of the minimum metallic resistivity and T^{**} maxima of resistance, explained by increased magnetic ordering.

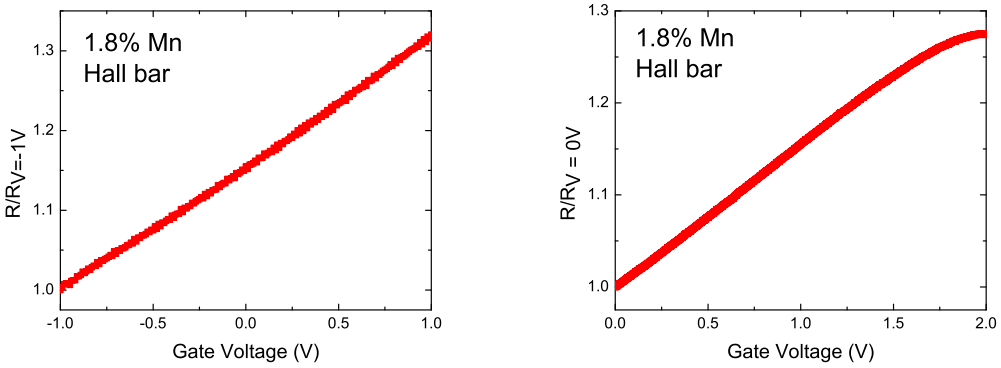

Fig. 3.5: Four-terminal resistance versus applied DC gate voltage for the Hall bar structure. The resistance shows at least 20% change in resistance at 1.5V. Beyond 1.5V, the trend of the change saturate, suggesting leakage current finally affecting the measurement in a measurable way.

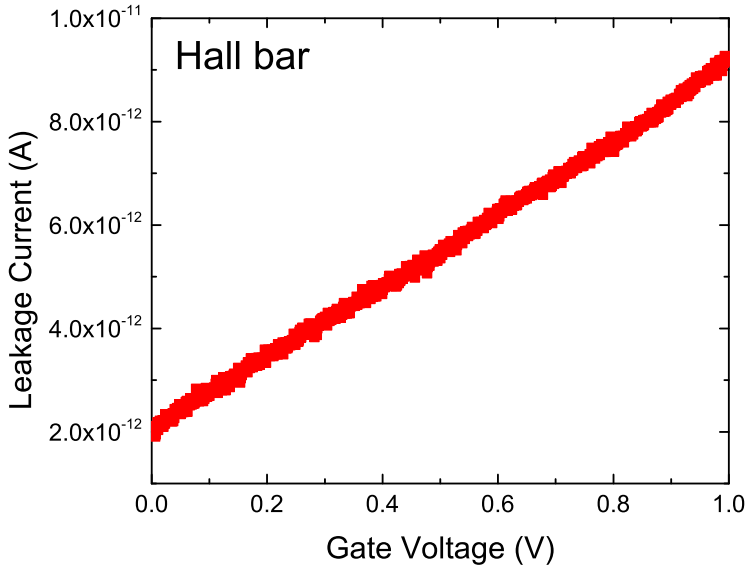

Fig. 3.6: Leakage current measurement through the Hall-bar structure with parabolic-doped (Ga,Mn)As and AlAs-AlGaAs all-semiconductor tunneling barrier. The leakage current is less than 1% at 1V applied gate.

olation places the leakage current reaching $\geq 2\%$ beyond 1.5V, which is consistent with the measured effect of the leakage current in Figure 3.5.

For the Corbino structure, cooling measurements showed a much larger percentage increase in the four-terminal resistance (Figure 3.7), suggesting proximity to the metal-insulator transition (MIT), which is supported by SQUID measurements.(Mn concentration at $\approx 2\%$) The difference between the channel resistances between applied gate voltages -1 V and 1.5V is around 200%. This is a large enhanced effect, considering the effect reported in Owen, et. al. is only a resistance increase of above 100% for an applied positive gate potential of 3V. [Owen 09] After this sweep however, the magnetic properties of the material change, owing the charging effects cause by the leakage current as it goes beyond 1.5V, consistent with previous observations for the Hall bar structure. Subsequent measurements are limited only to until 1.5V DC gate voltage. Reproducible conductance oscillations are also observed in the gating curve, which would be revisited later in this chapter.

3.2.2 In-Plane Magnetoresistance Measurements

Testing the effect of the electrical gating on the magnetic properties of the material, we first perform saturation magnetization scans with an in-plane magnetic field of 300 mT

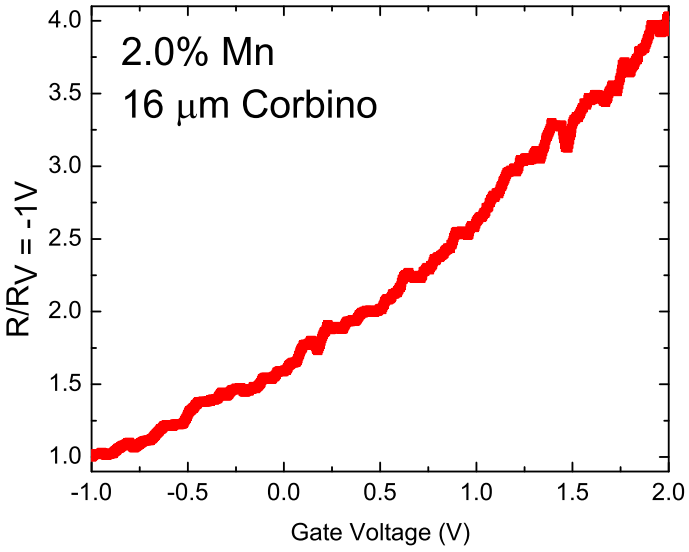

Fig. 3.7: Four-terminal resistance versus applied DC gate voltage for the 16 μm Corbino structure. The resistance shows at least 300% change in resistance at 2V. However, gating beyond 1.5V, the magnetic response of the device changes, suggesting charging effects and/or impurity re-configuration. For the subsequent measurements, the gating voltage is limited to 1.5V, as is suggested as well in the Hall bar structure.(Figure 3.5)

applied to the sample and rotated along different crystal directions. For the Hall bar structure, the magnetic response is shown in Figure 3.8. Electrical gating shows monotonic increase in both hard axis contributions along along [$\bar{1}$10] and along [110]. This is consistent with observations in [Owen 09]. The four-fold response is also consistent with the sample moving close to the MIT, with the crystalline contributions dominating the anisotropic magnetoresistance (AMR). The effects of the charge depletion seems concentrated on the uniaxial contributions to the magnetic anisotropy for these large structures.

To extract the pure crystalline contribution to the AMR, we use the Corbino structure since there is no preferred current direction in the device. However, compared to [Owen 09], we use smaller Corbino structure and remove the effect of the contacts by fabricating a four-terminal structure composed of four annular rings. The four-terminal structure removes spurious effects (e.g. effect of contact resistance) [Webb 86] and will be useful in observing pure response from the material. The results of the measurements are shown in Figure 3.9, showing a seemingly random effect of the applied gate voltage to the relative resistances in the hard axis directions. The normalized change in resistance with respect to the biaxial easy axis along [0$\bar{1}$0] for the different applied voltages are shown in Figure3.10, with the curves shifted for clarity.

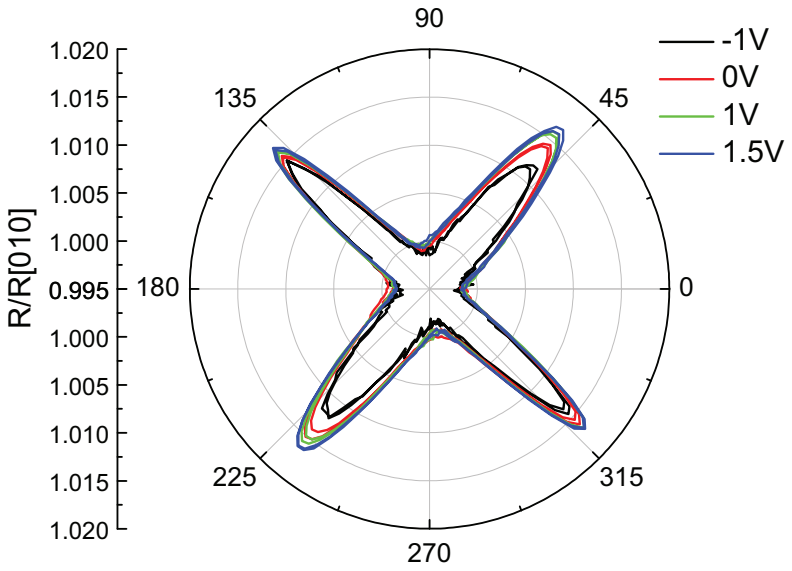

Fig. 3.8: Saturation magnetoresistance measurements at different voltages (-1V, 0V, 1V and 1.5V), with fields along different directions. Current is along $[\bar{1}10]$ and the values are normalized along [010], which is along the 0° direction of the applied field. For increasing voltage, the measurements show monotonic increase in the uniaxial contributions along the magnetization hard directions for both direction, with the largest increase in percent resistance along $[\bar{1}10]$ and $[1\bar{1}0]$.

We see from Figure 3.9 and the normalized resistances in Figure 3.10 that for the smaller structure, the behavior of the change in magnetoresistance contributions from the anisotropies in the sample is non-monotonic in resistance compared with that of the larger Hall bar structure (Figure 3.8). This can possibly arise from the small size of the structure, reducing the number of conduction paths within the system with the transport path approaching the coherence length.[Gira 07] The conductance fluctuations observed in gated structures are also attributed to the mesoscopic observation of a limited number of hopping paths dominating the transport.

In order to further check and observe the effects of the electric field to the anisotropy components in more detail, we extract the uniaxial and biaxial components from the saturation magnetization measurements. We follow the model from [Chib 08] for calculating the angle of the magnetization with minimum energy for different directions of the applied field:

$$E = \frac{K_B}{8} sin^2(2\varphi) + \frac{K_{U1}}{2} sin^2(\varphi - 45°) - MHcos(\vartheta - \varphi), \tag{3.1}$$

where K_B denotes the crystalline contribution arising from the biaxial anisotropy (along [010] and [100]) and K_{U1} for the anisotropy energy contribution from [110] and [$\bar{1}$10], following [Chib 08]. The calculated energy landscape with respect to the direction of the magnetization is shown in Figure 3.11.

We show the normalized resistances for each crystal direction in Figure 3.12, wherein no definite change in the relation between values for different crystal directions are observed. The extracted biaxial and uniaxial anisotropy components from the calculated percent change in the saturation magnetoresistance measurements for the Corbino structure are shown in Figure 3.13. We fitted all values to the normalized deviation from the en-

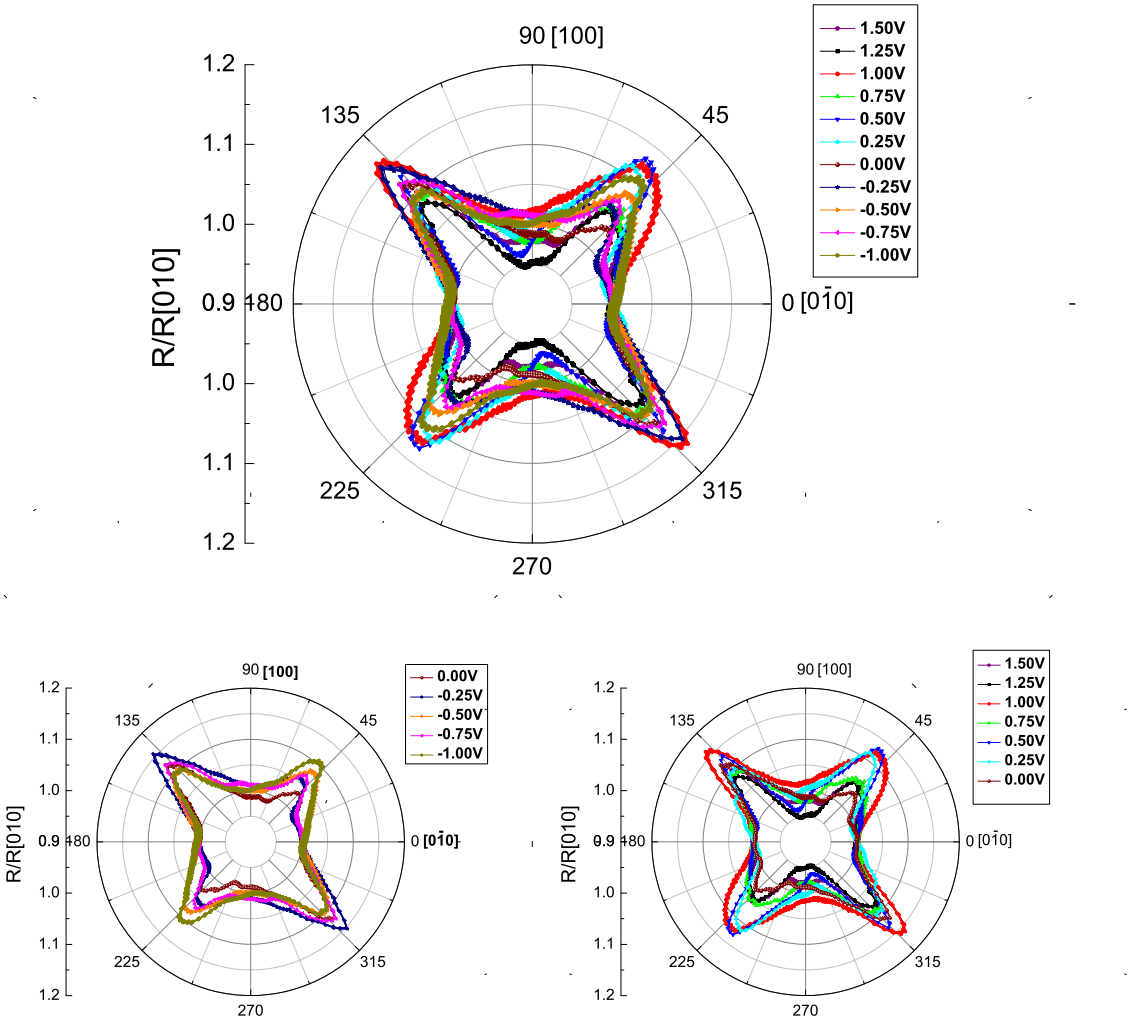

Fig. 3.9: Saturation magnetization measurements for different applied DC gate voltages from the Corbino structure. The changes in resistance appear non-monotonic compared to the linear change in the Hall bar structure.

ergy minima ∥ $[0\bar{1}0]$ ($\frac{E-E_{[0\bar{1}0]}}{E_{[0\bar{1}0]}}$). The extracted components for the Corbino structure also appear to not have a general trend/non-monotonic compared to the Hall bar structure

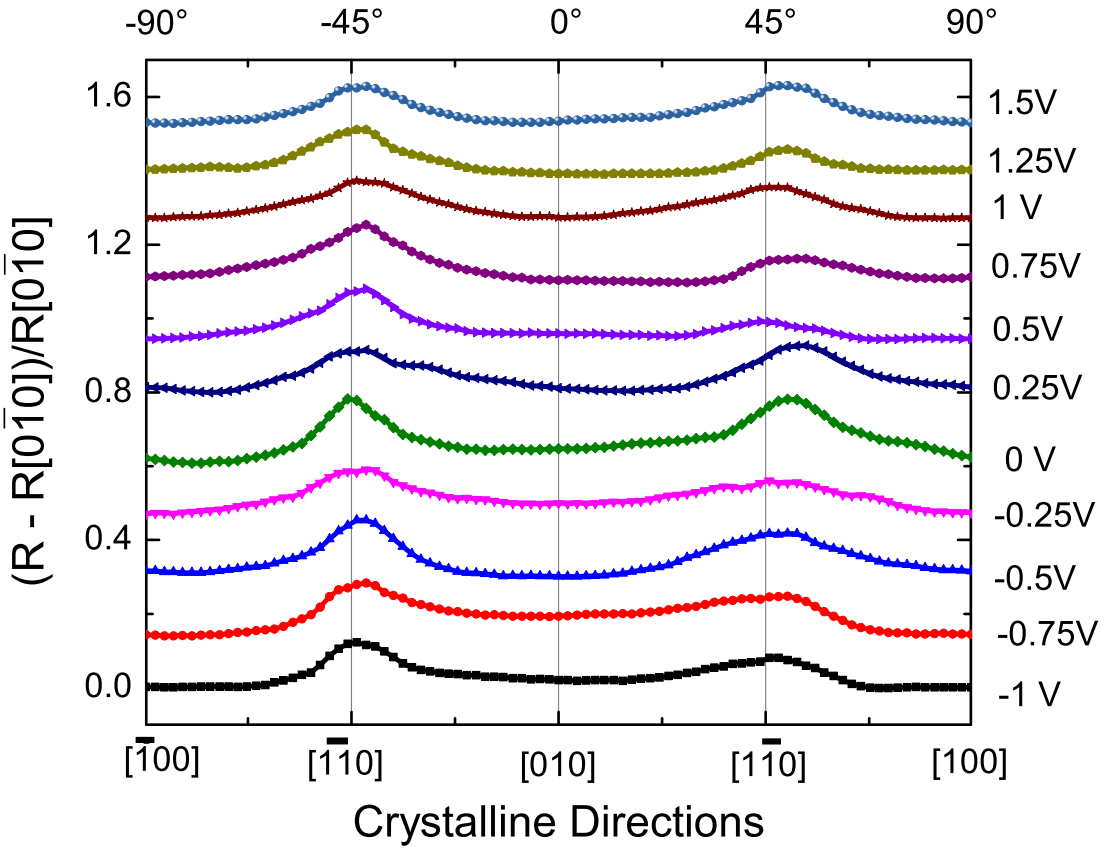

Fig. 3.10: Saturation magnetization measurements normalized with respect to the resistance along 0° (along $[0\bar{1}0]$) of the applied magnetic field. The curves are shifted for clarity.

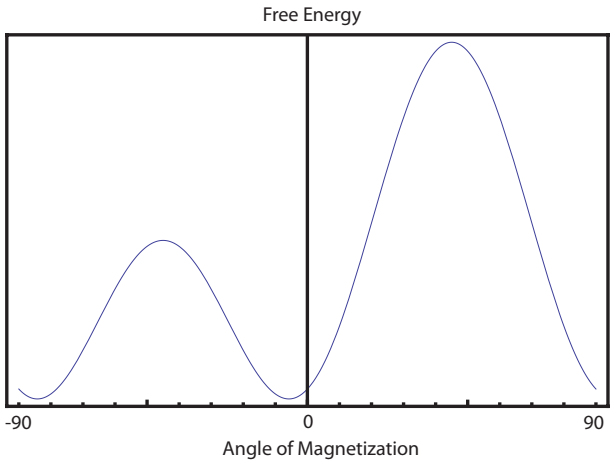

Fig. 3.11: Energy landscape based from 3.1 with K_U:K_B = -1:10.

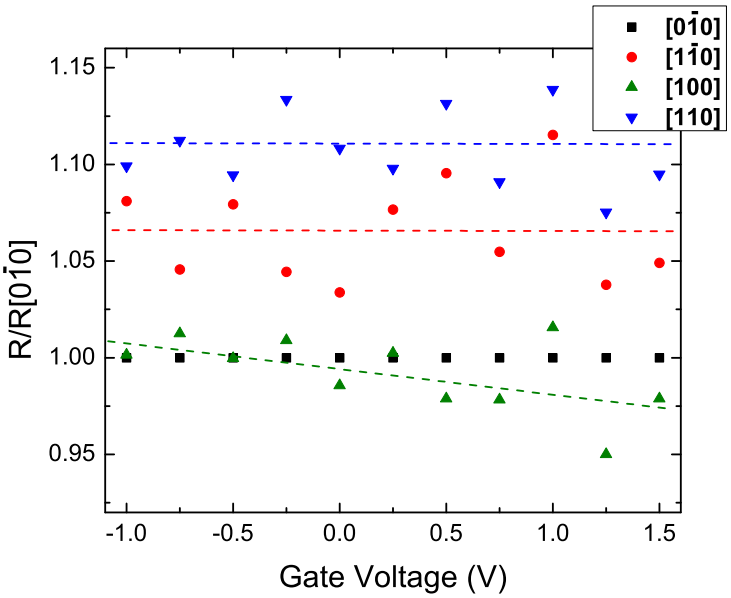

Fig. 3.12: Normalized resistances for the easy and hard axes changing with applied voltage. The resistance changes for all crystal directions appear to not have a general trend/non-monotonic. The resistance along [100] show slight decreasing trend with increased gate voltage but the range of applied voltages is too small to give a definite pattern.

with gate voltage as no strong trend with respect to applied voltage is observed for both constants. The biaxial anisotropy and the magnitude of the uniaxial contribution show slight increasing trend with increased gate voltage. The voltage range however might be too small to generalize the magnetic response with gate voltage. Still, we see the first signs of the increase in the uniaxial contribution as the holes are depleted from the thin (Ga,Mn)As film, consistent with observations from [Rush 06].

To further observe the effects of the in-plane applied field, we observe the magnetoresistance at particular crystal directions, focusing on the direction of the uniaxial contributions as we drive the sample closer to the metal-insulator transition. Shown in Figure 3.14 are the magnetoresistance curves for the Hall bar structure along the hard axis directions. The measurements show a change in the slope of the magnetic response at high fields, increasing with increasing applied gate voltage. Following [Diet 00], the depletion of holes may contribute to the Mn moments being less aligned at higher gate voltages, resulting in less alignment of moments at increasing field. This possibly results in the lower negative magnetoresistance slope for increasing gate voltage.

In Figure 3.15, we see that the relation between the [110] and [1$\bar{1}$0] changes as the gate voltage is increased to +1V. This is consistent with the material (parabolic (Ga,Mn)As layer) being metallic and slowly driven to the insulating state by a positive voltage, since

the curves for the -1V and 0V show no difference. We see that the change is also consistent with the saturation magnetization results in Figure 3.8, wherein the normalized resistances for [1$\bar{1}$0] and [110] reach the same value at increasing positive applied voltage.

From the in-plane measurements, we can (however tentatively because of the small gate

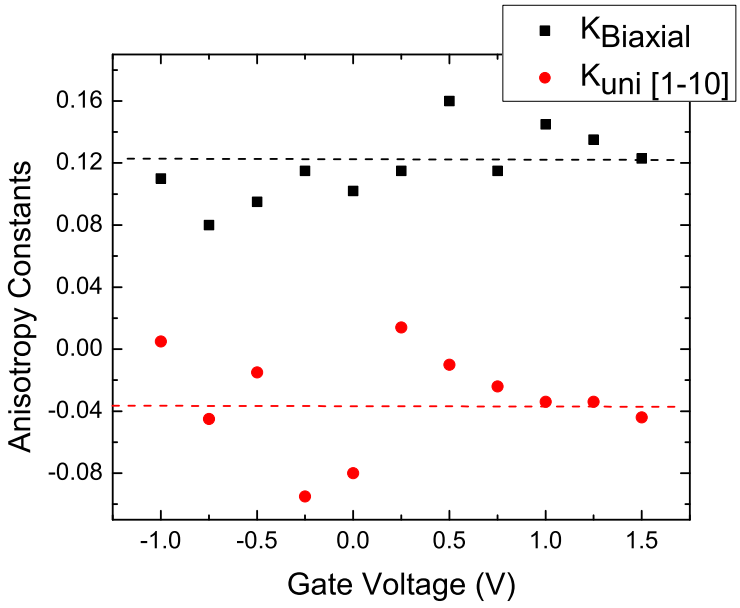

Fig. 3.13: Extracted uniaxial and biaxial anisotropy constants changing with applied voltage. The biaxial anisotropy constant is one order of magnitude higher than the uniaxial component. No strong trend with respect to applied voltage is observed for both constants. The biaxial anisotropy and the magnitude of the uniaxial contribution show slight increasing trend with increased gate voltage but the range of applied voltages is too small to generalize.

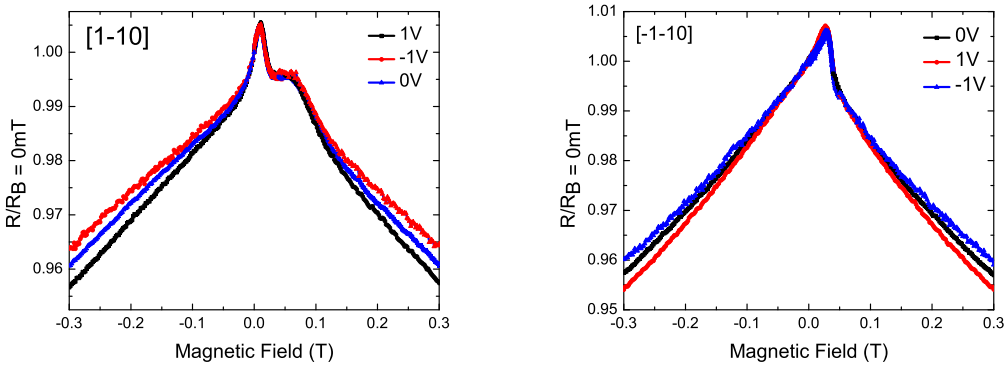

Fig. 3.14: Magnetoresistance curves of the Hall bar structure for the hard axis directions [1$\bar{1}$0] and [$\bar{1}$10] at different voltages. All curves are normalized with the magnetoresistance at B = 0mT.

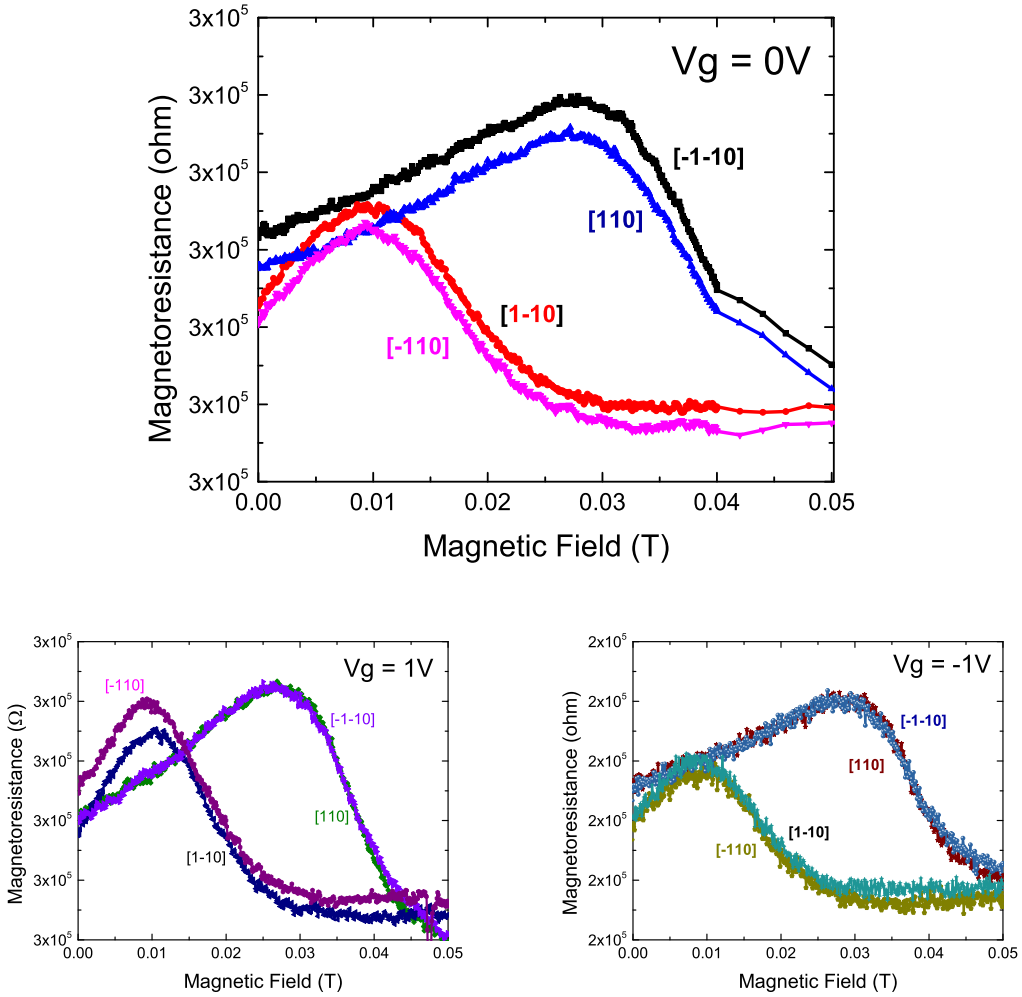

Fig. 3.15: Magnetoresistance curves along different crystal directions for the Hall bar structure at 0, +1 and -1V gate voltages. The curves for the -1V and 0V gate voltages shows no marked difference, which is consistent with the metallic behavior of the material. However, for the +1V gate voltage, the peaks for the $[1\bar{1}0]$ curves increase with respect to the [110] curves.

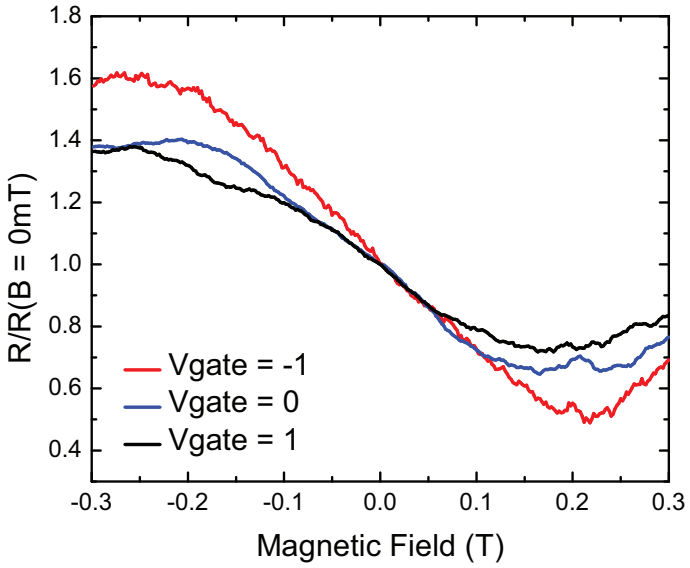

Fig. 3.16: Four-terminal Hall measurements on the parabolic layer Hall bar at different voltages. The plot shows increasing Hall voltage with decreasing gate voltage, driving the system into a more metallic, hence ferromagnetic, state. This behavior is consistent with results from [Ohno 00], albeit for a top-gate geometry and much higher applied voltage (+125V).

voltage range) see that the uniaxial contributions as the thin film device is driven closer to the MIT by charge depletion. The observed results are consistent with the observations from [Rush 06]. However, for smaller structures, we observe non-monotonic behavior which could arise from mesoscopic fluctuation effects. There is also the possibility of the material behaving non-linearly as it goes through the MIT, as [Sawi 10] pointed out the existence of paramagnetic and ferromagnetic domains at the MIT, which they also achieved by charge depletion.

3.2.3 Out-of-Plane Hall and Magnetoresistance Measurements

In order to complete our analysis of the gating effects to the material's magnetic anisotropy, we also test the behavior of the material with an out-of-plane field. For the Hall bar structure, we clearly see a decrease in the slope of the Hall signal. (Figure 3.16) This observation is consistent the previous gating measurements on gated structures, with the Hall signal reduced as it is driven closer to the insulating state with a high applied field.[Ohno 00, Chib 06a]

For the smaller structures, our analysis is limited by the geometry of the device. The current direction for the Corbino structure is along all directions, shorting the Hall effect. The out-of-plane measurements are shown in Figure 3.17 and the normalized resistances

in Figure 3.18. Unfortunately, both images suggest non-monotonic behavior with respect to gate voltage, with no strong trend. This might be due to the relatively small gating voltage we are limited in. [Ohno 00] used in their studies gating voltages as high as +125V to drive 5-nm (Ga,Mn)As to the non-magnetic insulating state. Further increase in the gating range can possibly give us a more in-depth study of the behavior of the material as it is driven to the insulating regime. It can also be seen that the fluctuations increase in strength and frequency with increasing positive voltage. This is consistent with a system where the number of conduction paths is being reduced with applied electric field, reducing the dimension of the hopping area from a two-dimensional conduction chain to a one-dimensional hopping chain where single hops may dominate the conduction behavior.[Raik 87, Hugh 96]) We revisit these fluctuations in the following section.

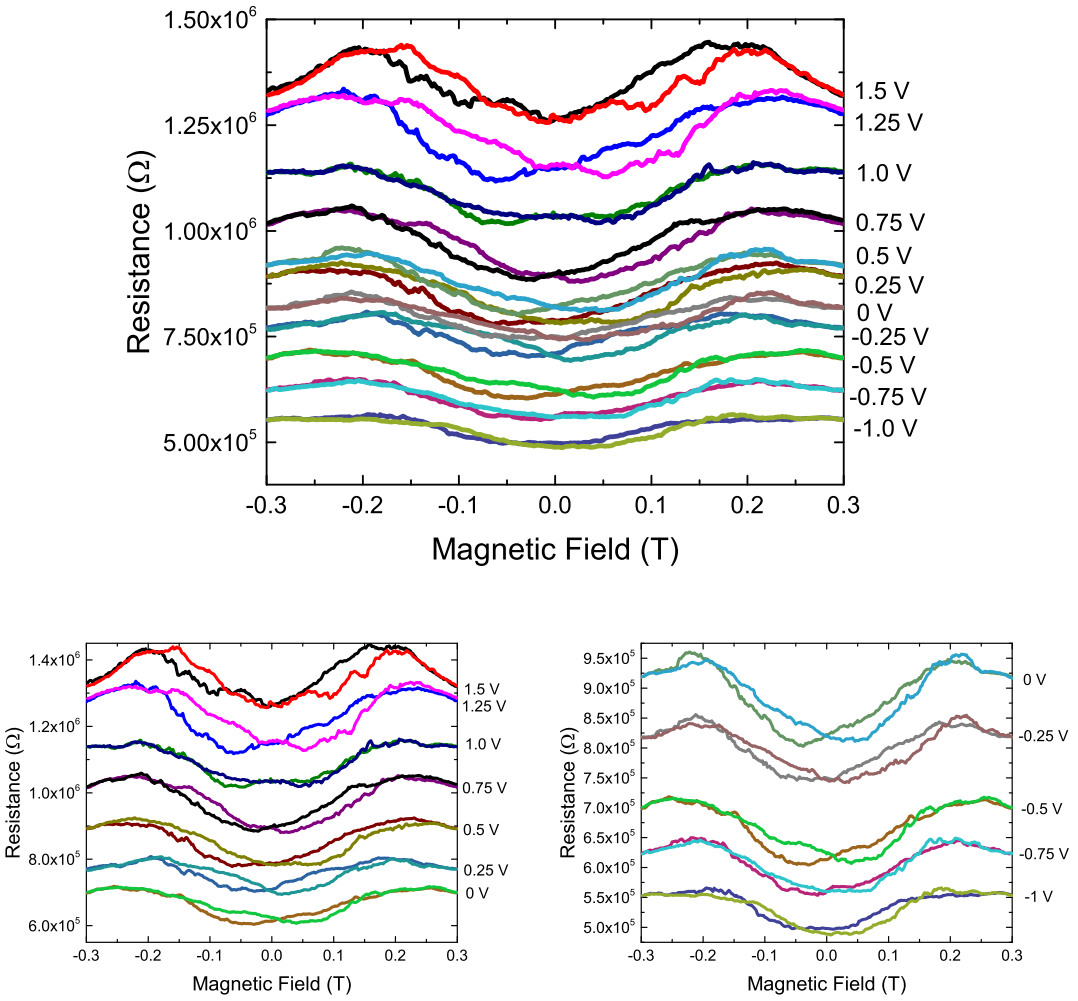

Fig. 3.17: Four-terminal Hall measurements on the parabolic layer Corbino structure at different voltages.

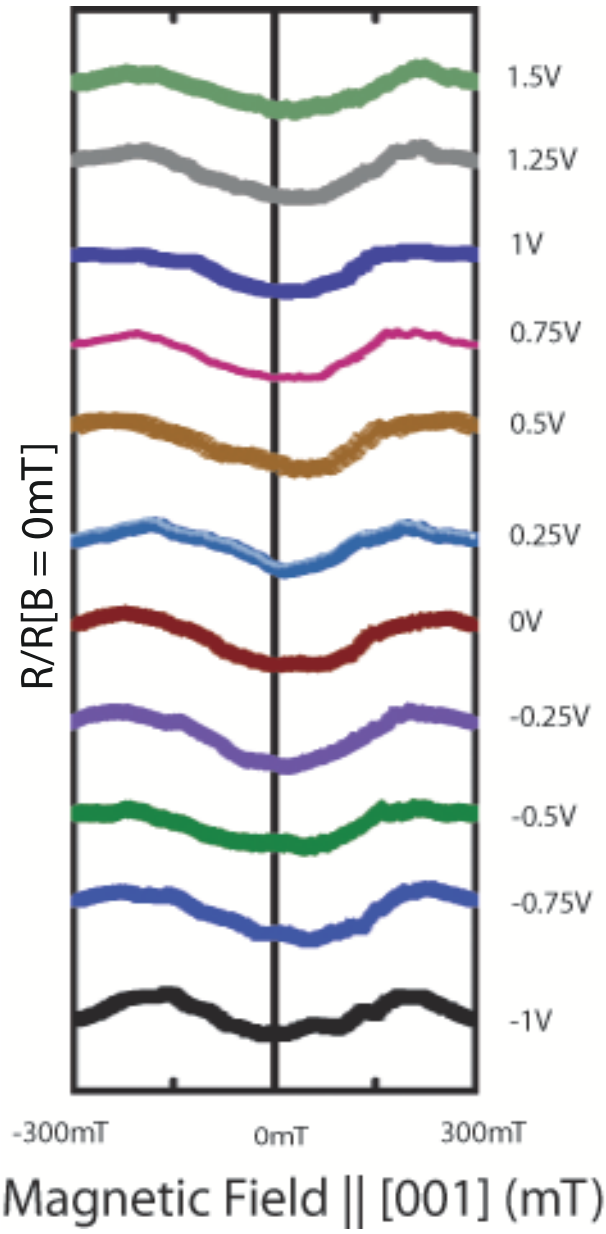

Fig. 3.18: Four-terminal Hall measurements on the parabolic layer Corbino structure at different voltages. The resistance are normalized with the zero-field resistance. Curves shifted for clarity.

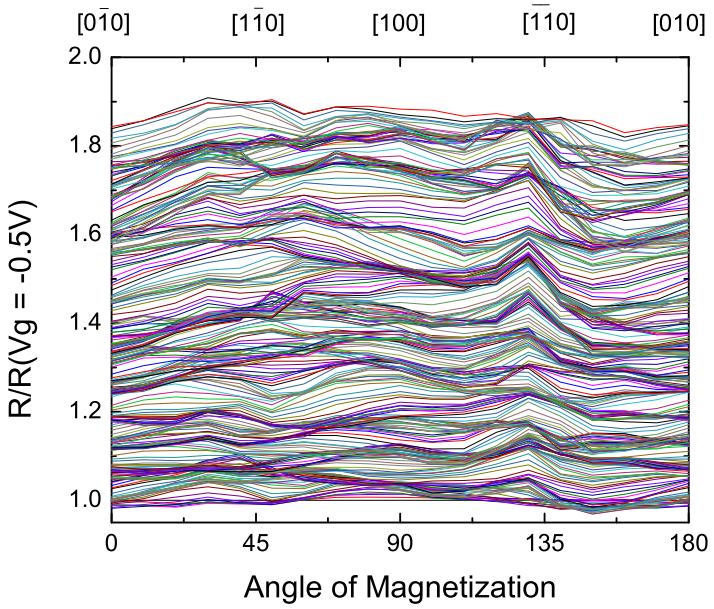

Fig. 3.19: Conductance fluctuations with respect to angle of magnetization. All applied field set at a saturation value of 300mT. The gate voltages are from -0.5V to +1V at 5mV steps. We see a concentration of the largest resistance fluctuations along [1$\bar{1}$0].

From the magnetic measurements, we see that the large structure shows monotonic behavior consistent with the results from [Ohno 00, Chib 08] and even [Owen 09]. For smaller structures however, the mesoscopic interactions again becomes more evident as the hopping interactions become stronger with increasing positive gate voltage. Increasing the range of the gate voltage will be of interest for future experiments, driving the material closer to the MIT and will be addressed in the next chapter.

3.3 Reproducible Conductance Fluctuations

For the smaller structures, reproducible resistance fluctuations begin to appear in our gating measurements. Shown in Figure 3.19 is the resistance versus voltage with values normalized by the resistance at the lowest gate voltage (V_g = -0.5V DC). The gate voltage range is from -0.5V to +1V (5mV steps) with the resistance increasing with increased positive voltage. The applied field is 300mT along different angles. The fluctuations show a concentration of high peaks along the [1$\bar{1}$0] directions.

Figure 3.20 shows that the resistance curves are reproducible with respect to field direction, also showing dependence of the fluctuations to the crystalline anisotropy. From Figure 3.9 and 3.10, we see no strong trend between the magnetoresistance peaks, but the uniaxial contribution is greater along this crystal direction for the Hall bar struc-

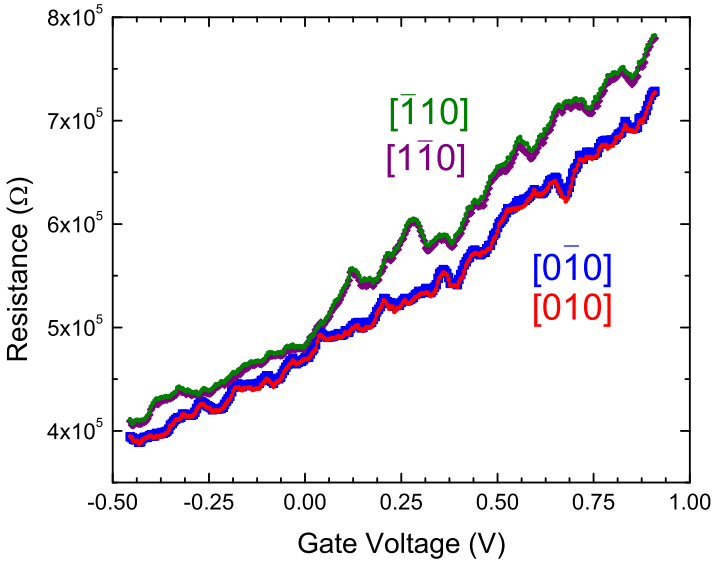

Fig. 3.20: Resistance with respect to gate voltage curves along different crystal directions. The conductance fluctuations appear to be reproducible and even with field direction.

ture (Figure 3.8). Thus these fluctuations are not completely random but related to the spin-orbit interaction which defines the crystalline anisotropy. The increased resistance fluctuations along the hard axis may be possibly explained as the system being driven into a state with a smaller number of dominant hopping states by the field as the magnetization switches to a uniaxial hard axis [110]. This is possible, as in [Papp 06] a junction was switched into the MIT using an applied field, driving the system to open an Efros-Shklovskii gap.[Efro 75] We also note that our sample is already in the vicinity of the hopping conductance regime (Figure 3.4).

Looking more closely to the behavior of these fluctuations at different crystal directions, we examine the normalized resistance fluctuations along the easy and hard axis magnetization directions. We normalize with the [100] curve to remove the linear electric field contribution in the background.[Raik 87] (Figure 3.21) It can be seen that the fluctuations follow the same trend for each crystal direction shown in Figure 3.12. The fluctuations along the uniaxial hard axes are observed to increase their deviation as the material becomes more metallic, with [110] becoming a harder axis than [1$\bar{1}$0]. This is consistent with previous observations in both the Hall bar (see Figure 3.8) and Corbino structures (Figure 3.12) that as the electric field (i.e. gating voltage) is increased, the ratio between resistances [110]/[1$\bar{1}$0] for the uniaxial hard axes decrease. We can see that the driving the magnetization to the hard axes also affects the interactions in the system, possibly allowing either a small number of hopping paths to dominate conduction or driving the system closer to the MIT by manipulating the anisotropic behavior of the impurity wave-

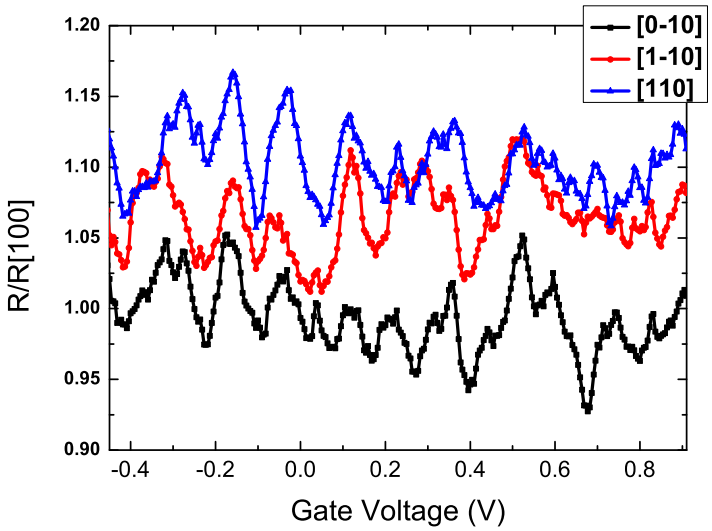

Fig. 3.21: Resistance fluctuations with respect to crystalline direction. The resistance response with gate voltage was normalized with the curve with field along [100]. All applied field set at a saturation value of 300mT. The fluctuations appear random, but certain fluctuation peaks correlate with magnetization direction.

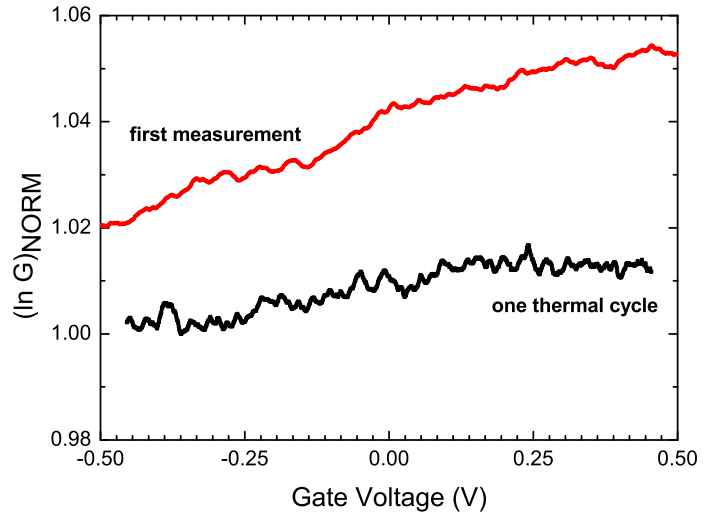

Fig. 3.22: Conductance versus gate voltage for first cooling and second cooling (one thermal cycle). The second cooling shows reduced gate efficiency and increase in frequency and height of reproducible conductance fluctuations. Curves shifted for clarity.

function with the applied magnetic field.[Papp 06, Schm 07]

After thermal cycling of the Corbino structure, the positions of the fluctuation peaks

changed significantly (Figure 3.22), indicating change in the impurity configuration during heating-cooling as with [Papp 06]. The frequency and height of the conductance fluctuations also increased after one thermal cycling, suggesting the possibility of sample aging. The same aging behavior of the fluctuations after thermal cycling is observed in [Vila 07]. Further analysis of smaller structures with these ultra-thin (Ga,Mn)As films with Mn concentrations near the transition might shed light to the real nature of these fluctuations and give a more detailed look into their thermal and electrical response.

3.4 Summary

In this chapter we have shown the electrical control of the magnetization of novel ultra-thin (Ga,Mn)As films, improved from Owen et. al by means of smaller gating structures.[Owen 09] As presented, our main limitation is the dielectric properties of the semiconductor barrier as we cannot go beyond a fairly low gating voltage. Reduction in leakage current through the barrier would be the next step in driving the material through the metal-insulator transition, preliminary attempts at which are discussed in the following chapter with the epitaxial lift-off technique (ELO).

Chapter 4

Epitaxial lift-off of (Ga,Mn)As thin films

In order to establish processing steps for further implementation of our gating experiments using other substrates, preliminary studies on the effect of the epitaxial lift-off process to the magnetic properties of (Ga,Mn)As thin films were performed. The possibility of using materials with higher dielectric constants for improved leakage current characteristics is highly attractive in continuing the exploration of results presented in the previous chapter, particularly through the metal-insulator transition. Effects on the magnetotransport behavior in lifted-off films are observed and discussed.

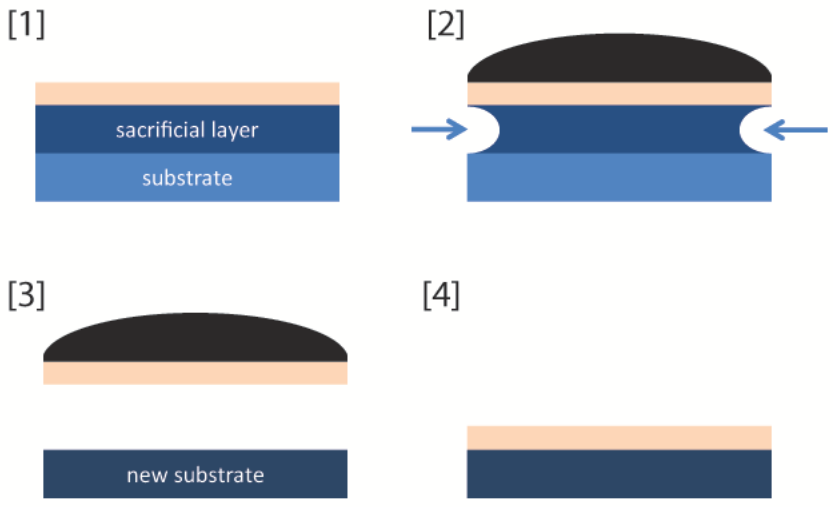

Fig. 4.1: Basic steps of the ELO process. Step [1] shows the desired film grown on top of a sacrificial layer, such as AlAs. In Step [2], black wax (e.g. Apiezon) is put on top of the film for protection and support. Step [3] shows the free-standing film after the etchant (e.g. HF) completely eats away the sacrificial layer. Step [4] shows the new film on top of a new substrate with the supporting wax cleaned away.

4.1 Epitaxial Liftoff (ELO)

To be able to use different barrier materials for our gating experiments, we employed the ELO process for its flexibility and extensive application in III-V semiconductors. Epitaxial liftoff is a process proposed and developed by [Yabl 87] for integrating III-V semiconductors onto different materials. The basic steps of this process is shown in Figure 4.1. (For a more detailed description of the lift-off fabrication steps used in this work, see Appendix B.)

The 'peeled-film' process was actually first observed and used by [Kona 78] for obtaining small free-standing GaAs films for fabrication of solar cells. While black wax was first used only as a protective coating for the film in their work, [Yabl 87] found that the wax provided a compressive strain on the desired film, resulting in an inward curl, providing access to the sacrificial layer to the etching agents. This led to improved sacrificial layer etching rates. For industrial applications, fast etch-rates and increased peeling area are desirable. An extended version of the technique includes weights suspended on the desired film to increase rate of peeling from the original substrate (weight-induced ELO (WI-ELO)).[Vonc 02] There have also been detailed studies on the etch rates for different materials. Table 4.1 shows the general etch rate values estimated for $Al_xGa_{1-x}As$ sacrificial layers with Al mole fractions x $\geq$ 0.4 at different temperatures.

ELO Etch Rates (μm/min)					
Mole Fraction x	230K	250K	273K	296K	328K
0.4		1.8E-6	1.2E-5	5.6E-5	3.8E-4
0.5	1.6E-3	1.2E-2	7.4E-2	3.8E-1	2.5
0.64	1.0	3.2	9.8	15	
0.8	6.5	11	18	28	

Tab. 4.1: Etch rates for various temperatures for AlGaAs tertiary alloys using 49 percent aquaeous HF solution. These are guide values as significant variation exist sample to sample. Based on [Yabl 90].

There have been other studies which have been proposed to integrate different materials. such as cleaving or complete removal of the substrate by etching. However, ELO has the advantage of lattice-matched growth, which provides high quality lift-off film and open choice of alternative substrates.[Yabl 90] In this study, we used 0° acid temperature to fully control the etch-rate of the magnetic material as the (Ga,Mn)As material's magnetic properties have been observed to change with exposure to HF through etching. Changes in thickness have been shown to contribute strongly to changes in the magnetic anisotropy.[Papp 07b, Goul 08]

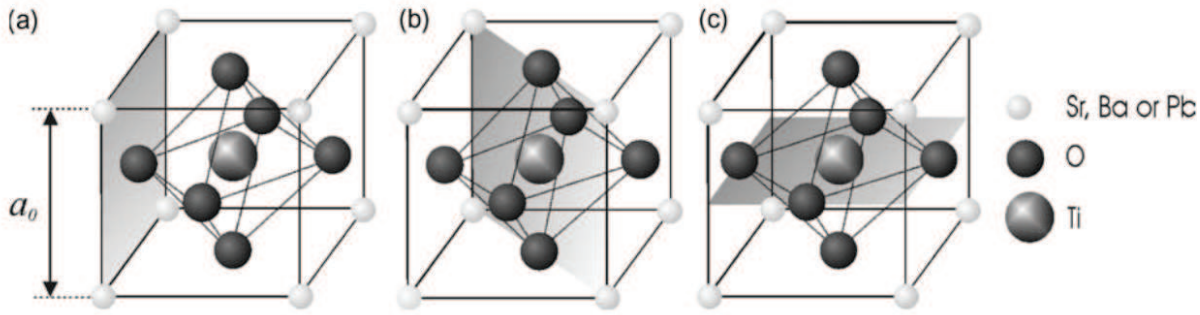

Fig. 4.2: Cubic structure of ABO_3 pervoskite crystals.(for our analysis, A = Sr and B = Ti) (a) shows the (100) AO-terminated plane (e.g. SrO). (b) and (c) show the (110) and (001) (TiO_2 termination) planes, respectively. Figure reprinted from [Pisk 04]

4.2 Test Barrier Material

For our purposes, we focused on a particular material Strontium Titanate $SrTiO_3$ to improve our gating devices's leakage current characteristics. Reported dielectric constants for this material is measured to be higher than that of $Al_xGa_{1-x}As$ (where x is Al mole fraction) and AlAs both at $\epsilon \approx 10$ - $15\epsilon_0$, which comprised the n all-semiconductor gating barrier used in the previous chapter.[Owen 09]

4.2.1 Strontium Titanate $SrTiO_3$ (STO)

Strontium Titanate or STO is a prototypical perovskite ferroelectric oxide has been subject of interest due to its desirable electronic properties (e.g. large electric field-sensitive permittivity). The perovskite crystal structure is shown in Figure 4.2. It is found to be a

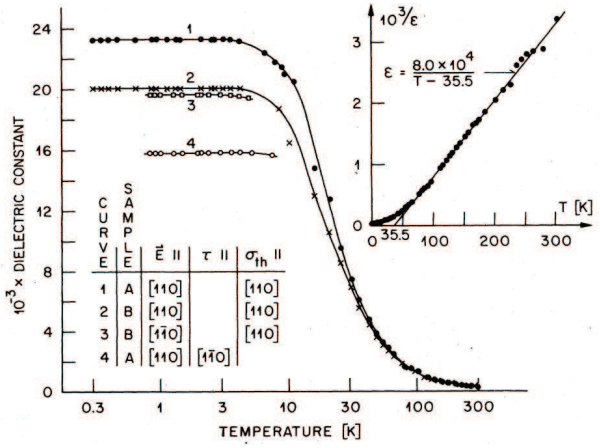

Fig. 4.3: Dielectric constant ϵ for bulk STO measured with temperature. Values at 4K show constants in the range of 10000 - 20000. The curves show samples with different current directions (E) and stresses (τ for strain and σ for thermal strain) Figure reprinted from [Mull 79].

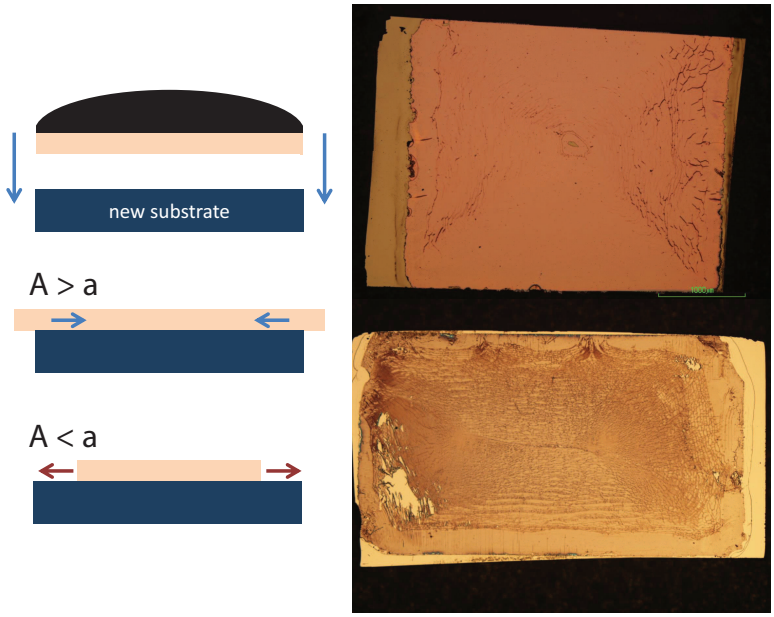

Fig. 4.4: Effects of the ELO process on the layer. Cracks appear on the surface, severely limiting the area usable for device fabrication. Defects on the surface may come from a variety of factors, such as defects on the new substrate, effects of the applied Apiezon wax and as well as strain induced by differences in the crystalline structure at the interface. The diagrams on the left show compressive (top) and tensile strain (bottom). A stands for the lattice constant of the top layer and a the lattice constant of the new substrate.

quantum paraelectric at low temperatures with high dielectric constant.[Mull 79] (Figure 4.3) The large dielectric constant at low temperatures makes this material an attractive prospect replacement for the all-semiconductor barrier used in the previous chapter.

As motivation for using this material as test barrier for gating thicker (Ga,Mn)As layers, we also refer to previous work using the material as gate dielectric. The use of STO on Si as isolating barrier [Eise 02] and gate dielectric [Eise 00] were already reported showing capacitances for 11 nm STO films equivalent to that of 1-nm SiO_2 barriers.

4.3 Lifted-off (Ga,Mn)As Thin Films

70-nm thick (Ga,Mn)As thin films grown on top of a thick AlAs sacrificial layer and semi-insulating GaAs substrate were used as test films for our test lift-off process. As for our STO substrates, layers were grown using a UHV pulsed-laser deposition (PLD) technique by F. Pfaff of EPIV. The lift-off technique yields large areas of usable film, but the quality is still highly process-dependent as shown in Figure 4.4. Cracks appear on the film which may render it unusable for device processing. These cracks can depend to a variety of factors, internal and external parameters such the induced strain within the layers due to

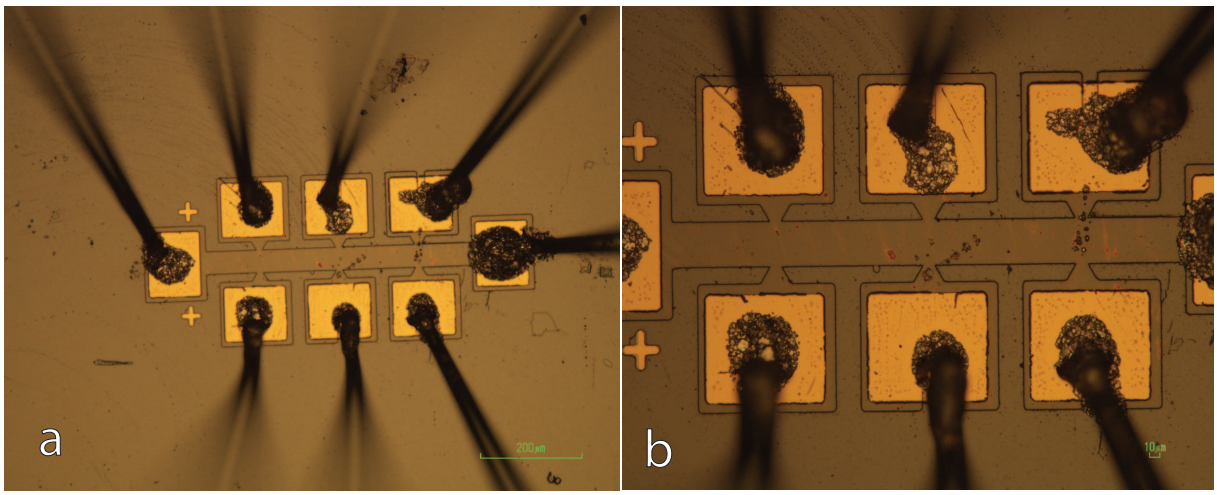

Fig. 4.5: Hall bar structure fabricated from the ELO (Ga,Mn)As layer. The samples were bonded with Ag-based glue for the gold wires to ensure that no pressure is applied on the lifted-off layer as even the slightest contact destroys the delicate van der Waals bonding of the (Ga,Mn)As layer on top of the new carrier substrate.

either substrate roughness, lattice mismatch or process-induced defects. The behavior of the protective wax can also play an important role in quality of the transferred layer, as it physically peels off the target film.

After lift-off, standard Hall-bar devices were fabricated on top of the layers (Figure 4.5) to measure the low-temperature magnetic and electrical properties of the material and for gating the (Ga,Mn)As thin film. Tunneling structures were also fabricated to measure the barrier height of the material to measure the leakage characteristics. For the fabrication steps, we use dry etching as wet chemical etching destroys the layer from gaps in the Van der Waals bonding. For connecting to the measurement chip carrier, we use glue/no contact bonding using silver-based adhesive to prevent the press of the bonding needle cracking the delicate film on top of the STO/Si substrate.

4.4 Magnetotransport in ELO-processed (Ga,Mn)As Films

In order to check the effects of the lift-off process on the magnetic anisotropies, particularly the biaxial anisotropy of 70 nm (Ga,Mn)As, we perform saturation magnetization measurements with an applied field of 300 mT along different directions. This magnetic field is usually enough to pull the magnetization of (Ga,Mn)As along the applied field. The resulting measurements are shown in 4.6. We see that the anisotropies are changed with respect to the crystal direction, with the hard axis shifting from the [100] direction

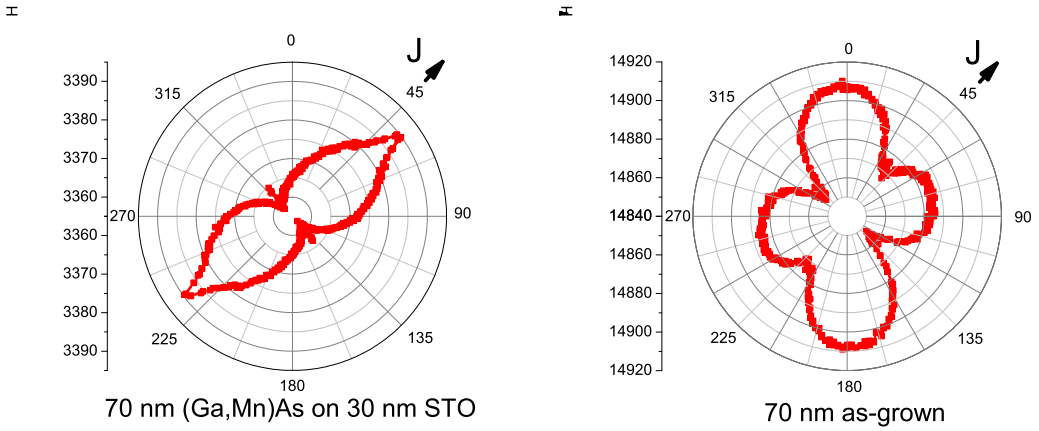

Fig. 4.6: Saturation magnetization measurements with rotating in-plane applied field. Both devices have current flowing along the [110] direction. The lifed-off layer shows a dominant uniaxial hard axis along the current direction at 45°, compared with the as-grown layer (on top of the AlAs sacrificial layer) with resistance maximum along 0° [100] and 90° [010].

in the as-grown layer (AlAs sacrificial layer) to rotating towards the [110] direction as the sample is placed on top of the 30-nm STO tunnel barrier. The lattice constant of crystalline STO is at ≈ 0.3905 nm, which is at least 30% smaller than the GaAs lattice constant $a_{GaAs} = 0.565$ nm. Aside from the possibility of the strain being released on the material as it is removed from the AlAs barrier, a sizeable compressive strain might also be the reason for the rotation of the anisotropies and reduction into a single hard axis for the lifted-off layer. Indeed several studies have already been done on the effect of strain on the magnetic anisotropies in (Ga,Mn)As.[Weni 07, Hump 07]

In order to further check the types of anisotropies present in the lifted-off material, we also perform variable field measurements at different angles. Shown in Figure 4.7 are the the resistance polar plots (RPP) for a lifted-off 70 nm layer on STO/Si and a reprinted reference RPP for a 70 nm (Ga,Mn)As layer from [Papp 07a]. The lifted-off layer shows the typical elongation along [110], suggesting uniaxial contribution to the anistropic magnetoresistance along [110], also clear from Figure 4.6. This behavior actually places the lifted-off layer closer to (Ga,Mn)As grown on GaAs substrate, suggesting release of stress from the sacrifical layer instead of a large lattice mismatch resulting in large compressive strain. Indeed, strain relaxation is observed in [Greu 11] as the (Ga,Mn)As is released from the sacrificial layer.

As a final test of the differences in the magnetic anisotropies in the as-grown and lifted-off layers, we perform low-field Hall measurements. From Figure 4.8, a substantial difference between the switching fields for the as-grown and ELO layers is observed in out-of-plane Hall measurements. The result is consistent with [Greu 11]. The release of the stress from the AlAs sacrificial layer was shown to reduce the saturation field for the magnetization.

From the MR and Hall measurements, we see that the ELO process preserves the general features of the (Ga,Mn)As 70-nm as-grown film, particularly the magnetic anisotropy,

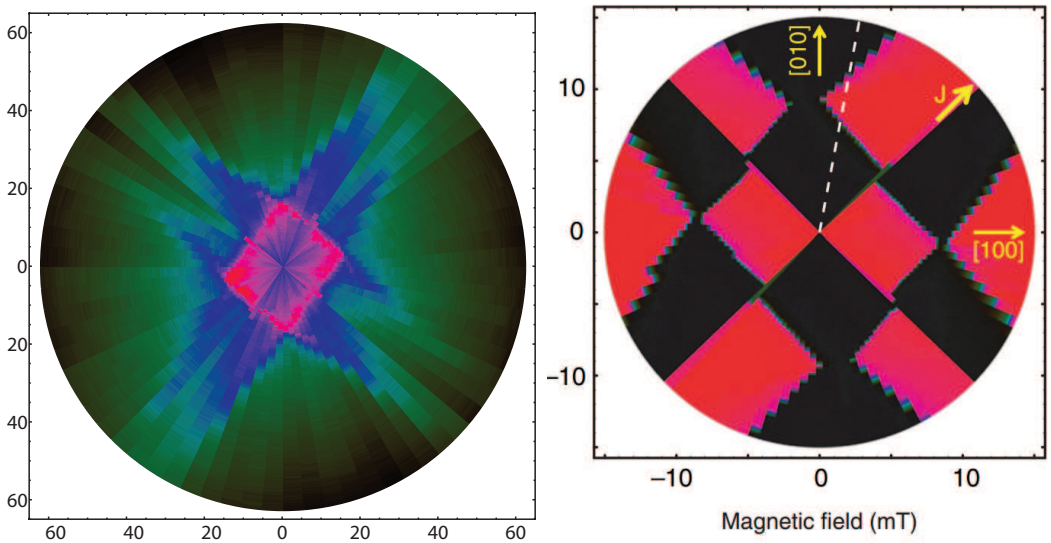

Fig. 4.7: Resistance polar plots for 70 nm (Ga,Mn)As thin films. On the left is the resistance polar plot for a 70 nm (Ga,Mn)As film deposited via ELO on top of 30-nm thick STO on n-type Si. The plot shows uniaxial contribution along the [110] and clear biaxial contribution. On the right is a reprinted reference RPP for a film of similar thickness grown on GaAs from [Papp 07a], showing uniaxial contribution along [$\bar{1}$10]. Reprinted image from [Papp 07a].

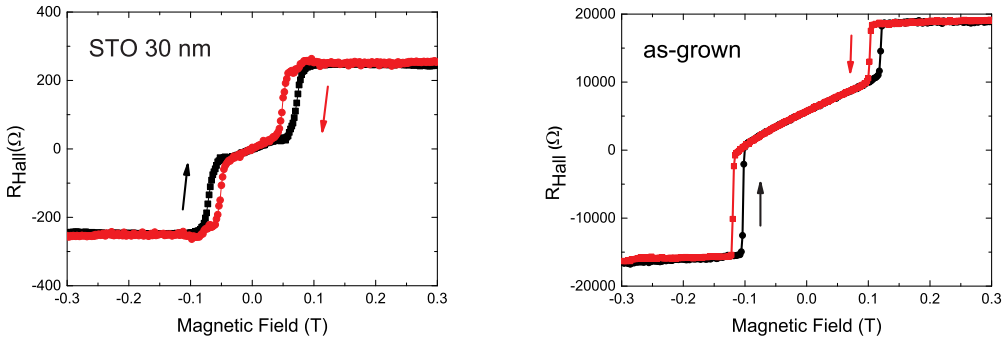

Fig. 4.8: Magnetization measurements with out-of-plane applied field and current along GaAs[110] for both samples. There is a marked difference in the switching fields between both measurements, showing reduction on the ELO-transferred layer on top of a 30-nm thick STO layer. ($H_{30nmSTO} \approx 50$mT versus $H_{as-grown} \approx 100$mT) The change is consistent with observations from [Greu 11]. The difference in the resistance values might arise from the difference in the signal extraction for both sets of data. The as-grown layer was measured directly from transverse contacts while for the ELO layer the signal had to be extracted from out-of-plane magnetoresistance measurements.

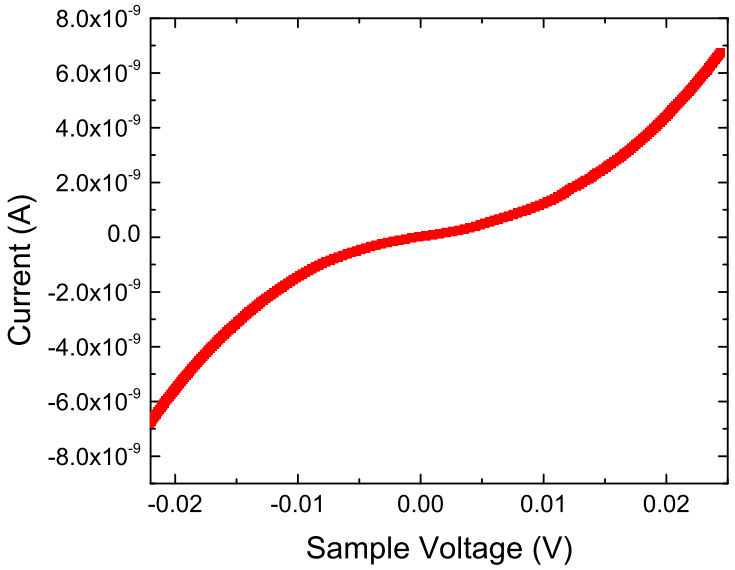

Fig. 4.9: Current-voltage measurement through the 30 nm thick STO tunnel barrier. The barrier shows typical tunnel barrier behavior, but suggests a very small tunnel barrier height, allowing current to leak through during gating measurements.

albeit with differences induced by strain-release or increased compressive strains. This verifies that the ELO process is a viable method in transferring (Ga,Mn)As thin films, preserving the basic anisotropies of the material and at the same time may be used to induced by strain interesting properties into the material with further testing.

4.5 Electrical gating of ELO-processed (Ga,Mn)As Thin Films

Unfortunately, our attempts at gating the lift-off device on the STO barrier are unsuccessful due to the large leakage currents measured through the 30 nm STO barrier. The tunnel barrier behavior, shown in Figure 4.9, suggests a very low tunnel barrier height. In order to get at least an approximate value for the height of the tunnel barrier, we use the following relation from the Brinkman model for trapezoidal barriers [Brin 70]:

$$\frac{G(V)}{G(0)} = 1 - (\frac{A_0 \Delta\varphi}{16\bar{\phi}^{\frac{3}{2}}})eV + (\frac{9}{128}\frac{A_0^2}{\phi})eV^2 \tag{4.1}$$

where the prefactor $A_0 = 4(2m)^{\frac{1}{2}}\frac{d}{3\hbar}$, the conductance at 0V estimated as $G(0) = \frac{3.16\cdot 10^{10}\varphi^{\frac{1}{2}}}{d}$

with d as the film thickness and the barrier height given by ϕ. We use a square barrier approximation to simplify our calculations, setting the second term of Equation 4.1 to zero. Using the relation from [Wolf 12] for the adjustable parameters α and γ: $\phi = \frac{\alpha}{\gamma}\frac{md^2}{4\hbar^2 e}$, we get an approximate barrier height of 17 meV by fitting to Figure 4.10. According to studies of band-offset of different high-k dielectric grown on Si from [Robe 02, Robe 06], this puts the current tunnel barrier way below the conduction bands offsets for industry standards SiO_2 (3.9eV) and Si_3N_4 (2.4eV).

Theoretical studies have shown that STO on Si has a near-zero conduction bandgap discontinuity.[Cham 01] The deposition of STO thin films on Si have also been observed to induce reduction in the dielectric properties (the material even becoming conducting) of the material due to thermal stresses [Cane 00], oxygen vacancies [Mull 04] and structural defects within the crystal.[Suzu 00] There is also of course the possibility of the lift-off and fabrication process affecting the quality of the film. Our calculation of the barrier height is consistent with this knowledge.

As previously noted, the use of STO on Si as gate dielectric was reported by [Eise 00] with capacitances for 11 nm STO films equivalent to that of 1-nm SiO_2 barriers. They show a 0.7-nm thick interface layer which has a lower dielectric response ($\epsilon = 4$) than the single-crystal film ($\epsilon = 175$) at room temperature. This was one of the main considerations in

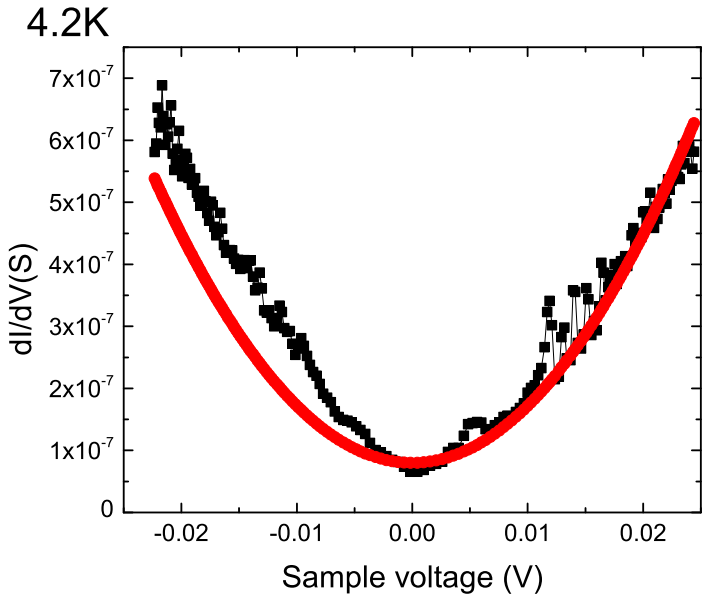

Fig. 4.10: Differential conductance through the tunnel barrier with respect to sample voltage. The calculated tunnel barrier is around 17meV (using simplified calculations from [Brin 70]), practically suggesting the conduction bands for $\approx$ 30 nm STO and n-type Si are aligned and cannot be used as a gating barrier.

using STO as our main alternative barrier material. In their study however, they high-quality epitaxially-grown single crystal, while our STO samples were so far preliminary attempts/calibration layers for first testing. Improved sample and device processing (e.g. less exposure to corrosive chemicals and water), crystallinity and decreasing thickness of the STO substrates used in future work may improve the leakage characteristics of the barrier with the lifted-off layer.

4.6 Summary

We established the effects that the techniques and processes for epitaxial lift-off on the magnetotransport properties. We perform preliminary trials at using PLD-grown STO thin films as our gate barrier. The zero conduction band alignment of the STO layer and the n-type Si substrate used prevents us from doing gate testing on this material system. Improved lift-off processing, growth on other substrates and improving crystallinity at a smaller thickness might be interesting directions at which future researchers can continue this work.

Chapter 5

Basic properties of Ferromagnet MnSi

Recent developments in the study of non-collinear spin structures, particularly MnSi, have prompted the renewed interest in the study of these types of materials. They have recently been the subject of several exploratory transport studies focusing on their unusual magnetic behavior, existence of exotic magnetic states or spin structures ([Papp 09], [Mueh 09]) and as testbed for existing theories such as those on the origin of the anomalous Hall effect (AHE).[Naga 10] These developments have inspired the initial development of in-house MnSi thin film growth in our group. In this chapter, we describe the basic properties of the weak itinerant ferromagnet MnSi and state-of-the-art research on its magnetic properties, particularly on its exotic magnetic structure.

5.1 Bulk properties of MnSi

Thought to be well-understood, interest in MnSi has grown in the recent years through the observation of new exciting electronic and magnetic properties, particularly non-Fermi liquid behavior under high pressure([Pfle 01]), presence of a Skyrmion lattice near the ordering temperature T_{ord} ([Pfle 10a]) and ultra-low current densities for spin-torque applications using these exotic phases.([Joni 10], [Schu 12]) These interesting material spintronic properties of MnSi are tied to the complex magnetocrystalline structure of the material.([Ishi 77], [Naka 80], [Grig 06a])

The weak itinerant ferromagnet MnSi is a cubic helimagnet with non-centrosymmetric B20 crystal structure belonging to space group $P2_13$ with distorted rock salt basis vectors $(u, u, u), (\frac{1}{2}+u, \frac{1}{2}-u, -u), (-u, \frac{1}{2}+u, \frac{1}{2}-u)$ and $(\frac{1}{2}-u, -u, \frac{1}{2}+u)$ for the right-handed form with u_{Mn} = 0.137 and u_{Si} = -0.155. For a left-handed structure, u is replaced by $1-u$. The lattice constant is around 4.558 $\mathring{A}$. The cubic crystalline structure is shown

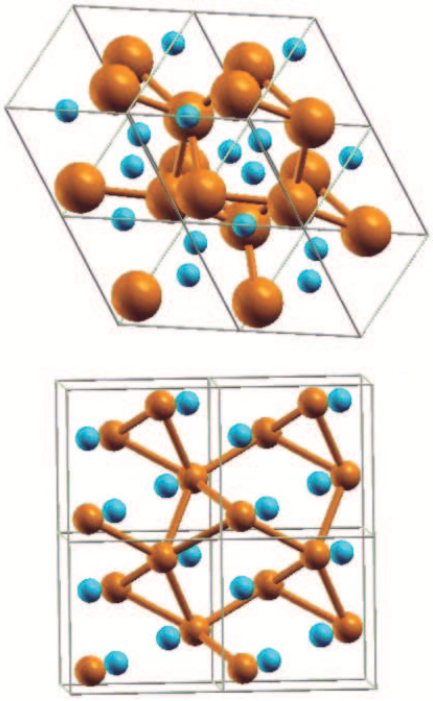

Fig. 5.1: Representations of the MnSi B20 cubic crystal with views from the [111] (top) and [110] planes. Larger spheres represent the Mn atoms. Figure reprinted from [Jeon 04].

in Figure 5.1.a.([Tana 85])

An additional Dzyaloshinskii-Moriya (DM) interaction [Dzya 58, Mori 60, Mori 76] $\mathbf{D} = \frac{D}{S}\mathbf{S}\cdot(\bigtriangledown\times\mathbf{S})$, where D is the DM constant, is included in the hierarchy of interactions due to the lack of inversion symmetry in the crystal. Theses interactions define the ground state of the non-centrosymmetric cubic magnet. Adding this spin-orbit term into the free energy equation, from the phenomenological MnSi model of Bak and Jensen, we get: ([Bak 80, Karh 12])

$$w(M) = \frac{c}{2}M_s^2(\bigtriangledown\frac{\mathbf{M}}{M_s})^2 + b_D M_s^2\cdot(\bigtriangledown\times\frac{\mathbf{M}}{M_s})^2 + \frac{S^2FQ^2(\mathbf{L}\cdot\mathbf{M})^2}{4a^3} - \mu_0\mathbf{H}\cdot\mathbf{M} \qquad (5.1)$$

where M_s corresponds to the saturation magnetization, $\mathbf{M}$ to the magnetization vector, $\mathbf{H}$ to the applied magnetic field, $S = 0.8\hbar$ to the spin per unit cell, $a = 0.4558$nm to the is MnSi lattice constant, $\mathbf{F}$ to the anisotropic exchange term and $\mathbf{L}$ to a cubic invariant term used to include the cubic anisotropy of MnSi B20 crystal. In most calculations,$\mathbf{F}$ and $\mathbf{L}$ are ignored because they are very weak compared to the DM spin orbit term. The constants c and b_D are related to the DM constant and the spin wave stiffness A by $c = \frac{AS}{M_s^2a^3}$ and $b_D = \frac{DS}{M_s^2a^3}$. The helicity of the spiral ground state depends on the sign of the DM interaction sgn($\mathbf{D}$) and to the pitch wavelength $L_D = |\frac{2\pi}{\mathbf{Q}}|$ by $\frac{S|\mathbf{D}|}{A}$.([Bak 80])

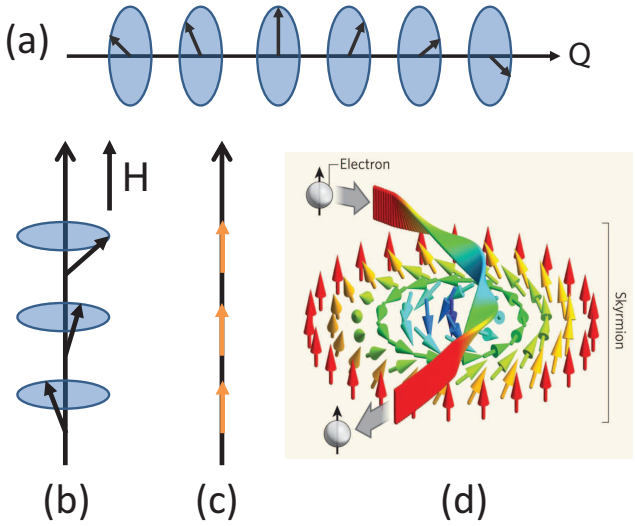

Fig. 5.2: Schematic diagrams of the helical ground state of MnSi at various states of magnetization. (a) shows the helical ground state at $H_{app} \leq H_{c1}$, where H_{c1} corresponds to the field required to transition from the helical state to the conical state (b), where the magnetic moments are pulled out of plane. Figure (c) shows the induced ferromagnetic state wherein the applied magnetic field ($H > H_{c2} > H_{c1}$) is strong enough to pull moments along the field direction. Skyrmion image reprinted from [Pfle 10b].

The three hierarchical energy scales (DM, ferromagnetic exchange and weak anisotropic exchange from the cubic anisotropy) defined in Equation 5.1 interact to determine the material's magnetic properties.[Bak 80] In Eq.5.1, the second term, which corresponds to the DM spin-orbit interaction, favors perpendicular alignment between spins. This competes with the in-plane preferred alignment in exchange interactions denoted in the first term. This competition between interactions result in the helical (or conical) bulk MnSi ground state as one-dimensional solution to Eq.5.1.(Figure 5.2) This resulting spin structure is not only characteristic to bulk MnSi. Helimagnetic behavior has been observed as well in low-dimensional MnSi structures such as one-dimensional CVD-grown nanowires ([Higg 10]) and two-dimensional thinned plate samples.[Tono 12]

In bulk growth with a single helical spin state, the propagation wavevector **Q** is pinned along the normal direction to the spin-plane. (Figure 5.2.a.) The intrinsic weak cubic anisotropy and the anisotropic exchange (**L**) pin the propagation vector along one of the cubic axes. The ground state spin helix in bulk MnSi is measured to have pitch wavelength $L_D = 18$ nm ([Ishi 77]) and a Curie temperature of $T_c \approx 29.5$ K. The conical phase arises from the application of a magnetic field along the propagation direction (perpendicular to the plane), distorting the spin helix (Figure 5.2.b). For bulk transport measurements

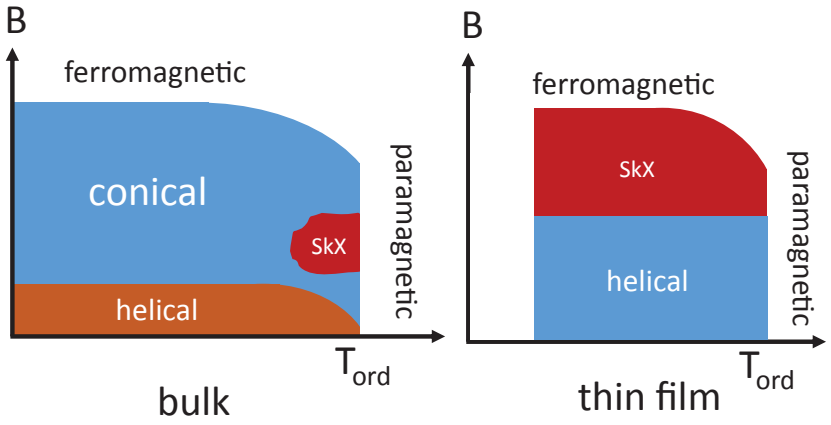

Fig. 5.3: Schematic representations of the T-H phase diagrams for bulk and thinned plate MnSi samples. For bulk MnSi, Skyrmion phase state (SkX) exists in a limited region called the A-phase. For the thinned plate measurements, the Skyrmion phase is measured to exist at a larger temperature and applied magnetic field range. Image referenced from [Tono 12] [thinned plate, t $\approx$ 50nm] and [Baue 12] [bulk].

the transition to the conical phase starts at 100mT until around 600mT where it enters an induced-ferromagnetic phase. (i.e. all spins are aligned along the applied field (Fig. 5.2.c)

The fourth magnetic phase observed in MnSi is the topological structure Skyrmion (Figure 5.2.d). Near T_c (ferromagnetic to paramagnetic transition phase), interesting transport behavior is observed for MnSi particularly the existence of the A-phase, a small region in the temperature-applied field (T-H) phase diagram wherein the Skyrmion lattice ([Pfle 09, Papp 09]) is observed to form and stabilize in bulk samples. (Figure 5.3) This region has also been observed in thinned plate samples ([Tono 12]) and much more recently in one-dimensional structures such as nanowires.([Yu 13]) The topological nature of this exotic phase couples with the carriers such that they pick up a Berry phase ([Berr 84]) from the varying magnetic field within the Skyrmion lattice. This results in a topological contribution to the Hall effect, insensitive to scattering processes. This is the topological Hall effect (THE).([Naga 10]) This magnetotransport signature has been the basis of identifying Skyrmion phases in MnSi and other materials with non-coplanar spin structures.([Shio 12, Shio 13, Yi 09]) Measurements have been performed to measure the signature of this magnetic state in MnSi, but there are still disagreements in the community regarding its true nature from measurements.(See: [Mueh 09, Papp 09, Karh 12, Bute 10])

The existence of these exotic magnetic states introduces a wealth of possibilities in future fundamental and applied research on the material, particularly spintronic applications such as spin transfer torque.[Schu 12] In addition, the calculated bandstructure of bulk

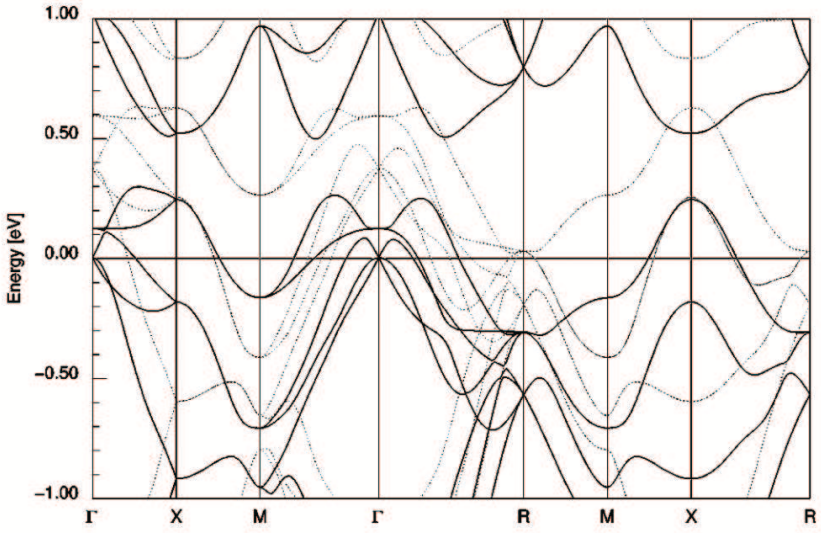

Fig. 5.4: Calculated bandstructure for MnSi at the ferromagnetic state. An average exchange splitting of 0.4eV was calculated between the minority and majority Γ spin bands. Figure reprinted from [Jeon 04].

MnSi at the ferromagnetic state (Figure 5.4) shows a considerable exchange splitting between the minority and majority bands, which implies the possibility of using the material as a detector for spin-polarized current as well as a spin-polarizer itself.([Jeon 04]) Hortamani et. al's DFT calculations for MnSi films deposited on Si[111] support this possibility for the MBE-grown thin films.([Hort 07]) This makes MnSi a promising material for integrated magnetic and electric functionalities in Si-based devices. Spin detection measurements have already been done on MnSi nanowires.([Lin 10], [Seo 10])

5.2 Expitaxially-grown MnSi Thin Films

In order to fully exploit the novel properties of MnSi towards device applications, it is important to understand and fully control its magnetic properties in relation to physical growth parameters such as thickness, type of substrate, etc. The epitaxial growth of MnSi thin films, with its enhanced T_c and rich collection of spin structures due to strain-induced in-plane anisotropies, promises the possibility of integration with established Si architectures. Magnano et. al. studied the ordered epitaxial growth of MnSi on Si[111] and established the ferromagnetic behavior of the films close to bulk and even a ferromagnetic transition closer to room temperature.[Magn 10] However, subsequent studies showed a much lower average transition temperature of 40 K.[Karh 10, Enge 12] A series of magnetotransport studies have explored and presented some observations on the effects of the strain-induced in-plane anisotropy on the magnetic properties of thin film MnSi.[Karh 10, Karh 11, Karh 12, Wils 12] In particular, they noted the possibility

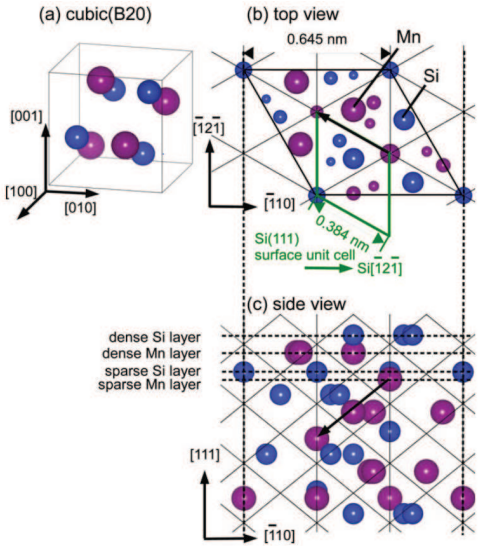

Fig. 5.5: Representations of the MnSi B20 cubic crystal. Purple atoms denote Mn and blue Si atoms. (a) Model of the right-handed MnSi cubic cell. (b) Top view of the epitaxially-grown MnSi(111) surface. The Si(111) surface unit cell is outlined in green, which shows a clear 30° rotation between both crystals. (c) Side view of the MnSi(111) crystal noting stacking order of sparse and dense layers. Figure from [Suto 09].

of other magnetization phases in thin films, i.e. depending on the value of the uniaxial anisotropy.

A diagram of the crystalline structure of epitaxially-grown MnSi[111] on Si[111] is shown in Figure 5.5. The lattice mismatch between MnSi[111] and Si[111] is calculated at -3.1%. (a[MnSi[111]]cos30° - a[Si[111]]) The difference in the lattice constants induce a tensile strain on the MnSi layer with Si[$\bar{1}$01]||MnSi$\bar{1}2\bar{1}$] and Si[111]||MnSi[111].[Zhan 02] The orientation of the cubic B20 MnSi unit cell with respect to the Si[111] substrate is shown in Figure 5.5.

Most of transport studies done on MnSi are usually done on bulk MnSi. Only recently studies on MBE-grown MnSi thin films were performed using SQUID and polarized neutron reflection (PNR) experiments, which reveal rich behavior at times different from the bulk, but still retaining qualitatively bulk MnSi-like qualities. ([Karh 10, Enge 12]) Most of the studies on thin MnSi films so far were done by Karhu, et. al. and they measured a helical wavelength of $|\mathbf{Q}| \approx 13.9$ nm, which they confirmed by thickness-dependent SQUID magnetization measurements.[Karh 11] (Figure 5.6) Their in-plane SQUID measurements show additional magnetic transitions which they cite as the formation of elliptical Skyrmions with increasing applied in-plane field.[Karh 12] (Also see Figure 5.7)

As for the magnetic properties, the experimental observations of [Karh 12] and [Wils 12] argue that stable formation of the Skyrmion lattice in MnSi thin films instead occurs

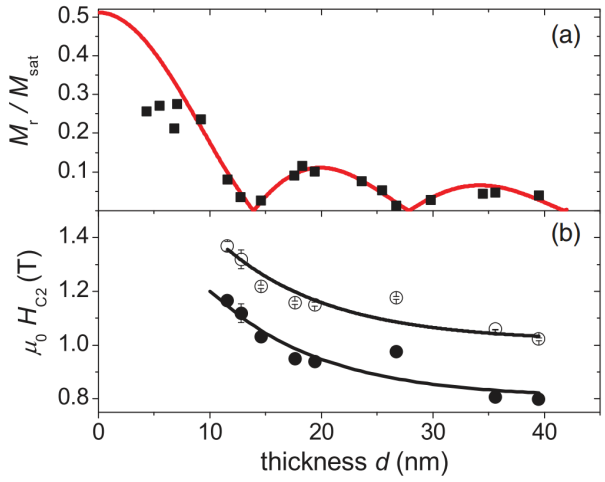

Fig. 5.6: (a) In-plane remanent magnetization M_r normalized by the saturation magnetization M_s for different thicknesses. The red line shows the fitting used to determine the pitch length $L_D \approx 13.9$ nm. (b) shows the trend of the second (in-plane) transition field H_{c2} (before saturation of the magnetization) with respect to sample thickness. Reprinted from [Karh 11].

from the two-dimensional perturbation on the free energy equation. These perturbations are due to the additional in-plane magnetic field and the uniaxial anisotropy induced by the -3% lattice mismatch between MnSi[111] and Si[111], forming helicoidal structures and elliptical skyrmions. This directly contradicts the results for bulk samples wherein the Skyrmion lattice is stabilized by an out-of-plane (H ∥ [111]) field. The magnetization and magnetic phses diagrams with respect to induced uniaxial anisotropy of the states present in MnSi thin films with applied in-plane field are shown in Figure 5.7. The field H_D corresponds to the field where the spins align aong the field to form 360° domains and K_0 the induced spin wave stiffness.[Karh 12, Wils 12] Recently however, formation of Skyrmionic structures (albeit lacking long range order of the Skyrmion lattice) have been observed by Lorentz TEM on a series of 10 nm films. [Li 13] This again puts forth the question of the true nature of the magnetic states in epitaxially grown films.

So we see that while progress has been made in optimizing growth parameters and understanding the magnetic properties of MnSi thin films on Si[111] in terms of magnetotransport measurements, there are still some issues that needs to be addressed such as reconciling thin film to bulk behavior and understanding the full set of complex mechanisms in describing the magnetic behavior of these strained thin films. The metallic behavior of thin films have been observed to qualitatively behave similar to bulk samples.([Enge 12]) However, different group measured shorter pitch lengths (≈ 8.5 nm from a series of 10-nm thin films using Lorentz TEM ([Li 13]) and ≈ 13.9 nm from thickness-dependent SQUID measurements ([Li 13])) Questions have also been raised on the sole attribution of MnSi magnetization behavior in [Karh 11] on growth-induced strain and instead proposed to possibly arise from reduced spin-spin interactions.[Enge 12]

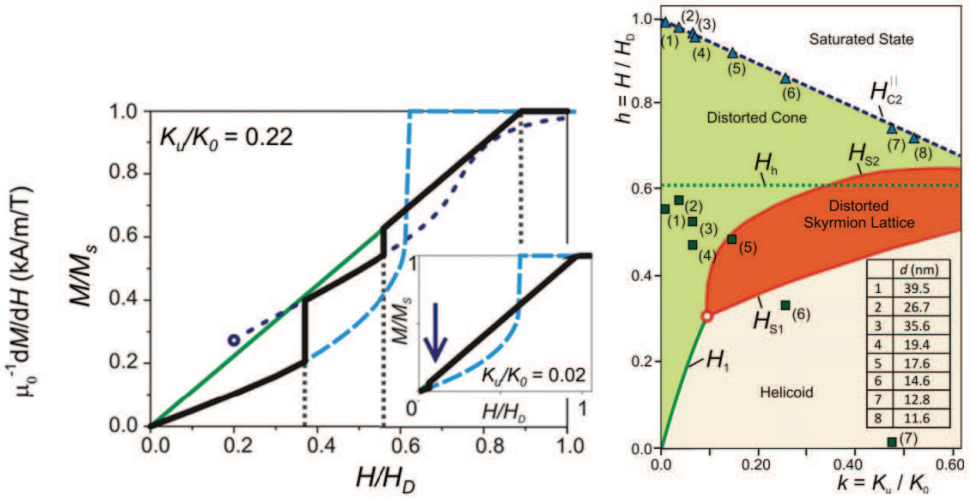

Fig. 5.7: Magnetic phase diagrams for magnetic sutrcutre formations in MnSi at in-plane applied fields. On the left shows a simulation of the magnetization with $K_u/K_0 = 0.22$. The black line indicates the energetically favorable state, with the green line repsenting the conical phase, the dark blue line the Skyrmion phase and the light blue line the helicoid phase.[Wils 12] On the right, the magnetic phase diagram for different magnetic phases is presented for samples of differet thicknesses. Reprinted from [Karh 12] and [Wils 12].

5.3 Skyrmions, Chirality and Magnetotransport in MnSi

As pointed out in the earlier sections, one of the main interests driving the curent study of bulk and thin film MnSi properties is the formation of the Skyrmion lattice.[Fert 13] Skyrmions in helimagnetic materials are topological defects formed as stable two-dimensional solutions to the free energy equation Eq. 5.1. This topological soliton was first proposed by Tony Skyrme from his deconstruction of the interactions between bosonic baryon states and fermionic mesons into coupled linear fields.[Skyr 62] While the initial intent was for the observation of pion interactions, the Skyrmion model trickled over to condensed matter systems with predictions and observation in materials such as chiral liquids, Bose-Einstein condensates, superconductors and magnetic thin films.[Fert 13] The latter set of materials includes prototypical cubic helimagnet MnSi, which is the material of topic in this work.

While the first signs of Skyrmion lattice formation have been deduced from structural and global magnetization measurements, transport measurements have been widely used in characterizing MnSi and other material systems with magnetic frustration and non-coplanar spin structures. The magnetotransport signatures are used to identify the magnetization structures present in the materials and Hall measurements have been crucial in picturing the magnetization behavior of such complex spin systems. For bulk MnSi, the signature of the Skyrmion lattice was independently observed by [Mueh 09]

and [Papp 09] in the limited T-H region (near T_c) of the A-phase. The small temperature region near T_c = 29K shows the existence of a Skyrmion lattice through the observed topological Hall effect (THE), which was pointed to arise from the Berry-phase acquired by electrons passing through the Skyrmion.(5.2.d.) [Neub 09a]) Thinned samples were also shown, using Lorentz TEM imaging, to exhibit the SkX phase for an extended T-H region.([Tono 12, Yu 10, Yu 11]) The THE was extracted by fitting measured values to the Hall resistivity equation ([Hurd 72, Naga 10])

$$\rho_{xy} = R_0 B + S_H M \tag{5.2}$$

where R_0 is the ordinary Hall coefficient, M the magnetization and S_H the AHE parameter. [Lee 07] performed Hall measurements on MnSi bulk samples, taking into account relatively high purity and high magnetoresistance signal of the material, to effectively separate the anomalous and ordinary Hall effects. Extracting the Hall parameters using measurements on bulk samples, [Lee 07] simplified the parameter extraction by phasing out the skew-scattering term αM in $S_H = \alpha\rho_{xx} + \beta\rho_{xx}^2$ reducing the AHE term of Eq. 5.2 to a ρ_{xx}^2 - dependence (intrinsic AHE). The linear skew-scattering term $\alpha\rho_{xx}$ was found to not contribute significantly to the fitting in the clean limit. Thus the ordinary Hall and AHE can be fitted from the raw Hall resistance using the simplified formula:

$$\rho_{xy} \approx R_0 B + \beta\rho_{xx}^2 M \tag{5.3}$$

In contrast to methods used in bulk samples ([Lee 07]), wherein they extracted Hall parameters in the high purity limit with low resistivity MnSi, [Li 13] extracted α by taking advantage of the resistivity reaching residual values at very low temperatures. Measuring 10-nm thick MnSi films, they extracted a value of $\alpha M_S \approx 3.5 \times 10^{-3}$. The topological signal was extracted by [Li 13] for epitaxiallly-grown MnSi thin films by expanding Eq.5.2 as Equation 5.4.

$$\rho_{xy} = R_0 B + (\alpha\rho_{xx} + \beta\rho_{xx}^2)M + \rho_{xy}^T \tag{5.4}$$

Other methods to drive MnSi into other exotic phases have also been of interest. High pressure measurements on bulk MnSi have also shown interesting magnetotransport signatures such as anomalously large topological Hall contribution ([Lee 09]), recently proposed to signal the formation of a non-Fermi liquid in MnSi.[Pfle 01, Ritz 13a, Ritz 13b]

[Ritz 13a] propose that at the formation of non-Fermi liquid (NFL) region (see Figure 5.8), a general phenomena may occur where there is full suppression of the magnetization which may in turn allow the formation of complex spin structures. One such complex spin structure predicted for the NFL phase is the BCC spin crystal.(BSC) The spin structure

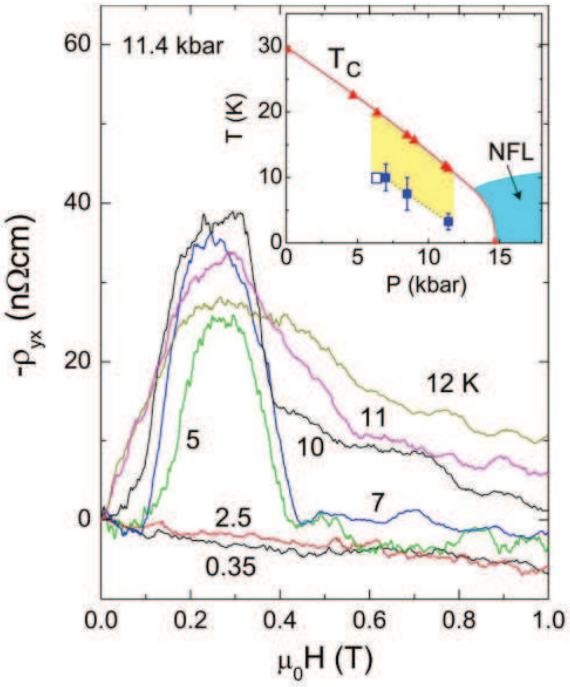

Fig. 5.8: High pressure measurements of the Hall resistivity show large topological contributions to the Hall signal at elevated pressure. Reprinted from [Lee 09]

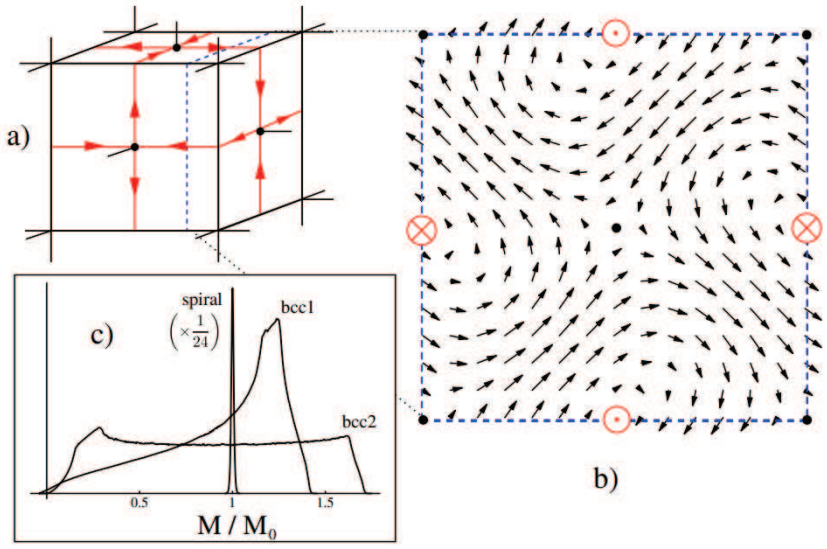

Fig. 5.9: Schematic representation of the bcc spin crystal (BSC) magnetic structure from [Binz 06b]. (a) shows the structure with the black nodes indicating M = 0 with (b) showing the cross section of (a) with arrows denoting in-plane magnetization. Image (c) shows the probability distribution of BSC states. Reprinted from [Binz 06b]

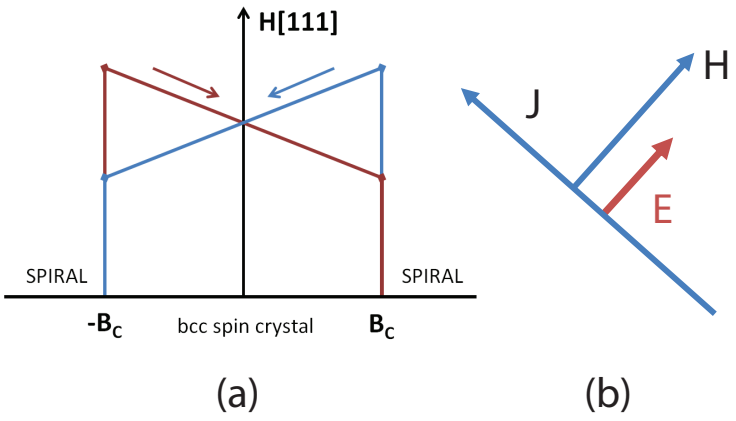

Fig. 5.10: Magnetotransport signatures from the BSC spin structure. (a) corresponds to the bow-tie hysteresis/quadratic contribution on the Hall signal arising from the symmetry breaking from the chiral parameter. (b) shows the additional electric field contribution to the planar Hall voltage (J ∥ $[1\bar{1}0]$) arising from the symmetry of the spin crtsyal. Image reference: [Binz 07]

is shown in Figure 5.9. [Binz 06b, Binz 06a]

This phenomenological model was derived from diffraction results near the phase (Fermi to non-Fermi) transition at high pressures, which shows reorientation of the propagation vector from [111] to [110].[Pfle 04] This partial order is modeled as linear superposition of helices, forming a bcc-structure spin crystal.[Binz 06b] The spin structure is shown in Figure 5.9. In this model spin structure, a chirality-induced anomalous term is predicted to manifest in the Hall measurements, among other magnetotransport signatures.[Binz 07, Binz 08] Several magnetotransport signatures have been predicted for the BSC state, shown in Figure 5.10.[Binz 07]

These structures arise mainly from the chiral character of the BSC state.[Binz 08] The Hall contribution is a quadratic Hall term given by Equation 5.5.

$$\rho_H \mathbf{B}_{eff} = (\rho_H + \frac{1}{\sqrt{3}}\gamma SB)\mathbf{B}, \tag{5.5}$$

where B_C is the effective field including contributions from the BSC global time-reversal symmetry breaking order parameter S. The signal manifests as a bow-hysteresis in the Hall signal arising from the changing sign of S. With a current j running along $[1\bar{1}0]$ with voltage drop measurement perpendicular to current direction, the BSC induces an

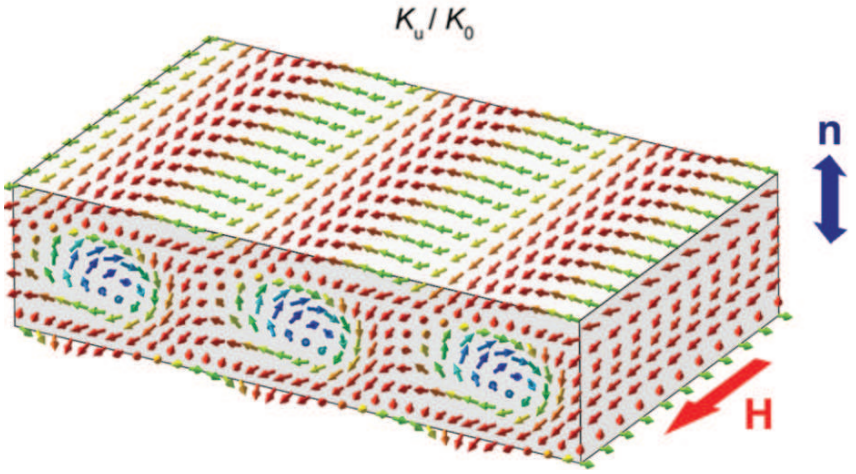

Fig. 5.11: Formation of the elliptical Skyrmion grating from an applied in-plane field. K_u/K_0 is the ratio between the uniaxial anisotropy strength parameter and the effective spin wave stiffness. Reprinted from [Wils 12]

additional electric field along the voltage contacts given by Equation 5.6.

$$E^H = B(\rho_H \hat{\mathbf{z}} - \gamma S \mathbf{B}) j \tag{5.6}$$

While the thin film samples are not under an applied pressure, the tensile strain due to the MnSi[111]/Si[111] growth induces pressure comparable to externally applied pressure measurements.[Karh 10] Also, one of the possible routes for the formation of a BSC state is the presence of disorder in the system.[Binz 06a]

Most measurements for bulk MnSi show the formation of the Skyrmion lattice with an out-of-plane applied magnetic field. For thin films, however, the theoretical works of Bogdanov and collaborators [Bogd 02] and subsequent experimental works on SPE and MBE-grown films by Karhu et. al on epitaxially-grown MnSi thin films argue that instead of a magnetic field along the hard axis along Si/MnSi[111], an in-plane applied magnetic field would result in the formation of a stable Skyrmion lattice by means of a two-dimensional perturbation from the strain induced in-plane anisotropy and the applied field.([Rler 10, Roes 11, Bute 10, Karh 12, Wils 12]) Polarized neutron scattering measurements also point out the presence of other types of spin textures and magnetization states in thin films. ([Karh 12]) They use these possible structures to alternatively explain magnetotransport signatures interpreted as the THE signal as in bulk samples. The formation of the elliptical Skyrmion from helicoidal structures is shown in Figure 5.11.[Wils 12]

In summary, the formation of the exotic magnetic structures in MnSi promises new concepts for clarifying long-standing theoretical issues and for future devices and applica-

tions. MnSi provides a great opportunity to combine existing Si architectures to magnetic processes in integrated circuits, particularly control of single skyrmions as information carriers [Fert 13] and ultra-low current memory applications.[Joni 10][Schu 12] Only recently, a new method of writing and deleting single Skyrmions using scanning tunneling micrscopy has developed, promising full control of these magnetic structures.[Romm 13]

5.4 Summary

A brief introduction into the current state of the art in the study of the magnetic and electrical properties of MnSi bulk and thin films shows the rich possibilities in the continued probing of the properties of such novel materials. The rich phenomena and unanswered questions in its magnetic characteristics justify the interest in pursuing the development of facilities for their growth and characterization of the itinerant ferromagnet MnSi.

Chapter 6

Epitaxial Growth of MnSi Thin Films

This chapter details the preliminary results of the development of in-house MnSi thin film growth in our group. In this chapter, we describe the material grown for this work and the preliminary characterization techniques done to verify its material properties. The following chapters would focus on the magnetoransport behavior of the grown thin films and implications to future work.

6.1 Epitaxial growth of MnSi Thin Films

The aim of this work is to establish the growth of MnSi thin films within our group and characterize their transport properties for future optimization and applications. Following the work of [Magn 10], thin film MnSi samples on Si[111] were grown by MBE by Christoph Pohl of EPIII using a co-deposition technique. In the co-deposition method, a layer of Mn is first deposited at room temperature on the cleaned substrates and then subsequently annealed at higher temperatures. ($\approx$ 400 deg Celsius at high Si and Mn atmosphere)

The films were grown on boron-doped single-side polished Si[111] substrates and the substrates are used and cleaned using standard preparation techniques with an additional step of growing a Si (approximately 32 nm-thick) buffer layer to smoothen the substrate surface before deposition of the Mn layer. Figure 6.1 shows the RHEED pattern from MnSi growth on Si, which indicates crystalline growth/formation. After film growth, a thin Si cap is grown on top of the layer. Depending on the substrate growth, an amorphous (a-Si) or crystalline (c-Si) is deposited as cap to prevent oxidation.

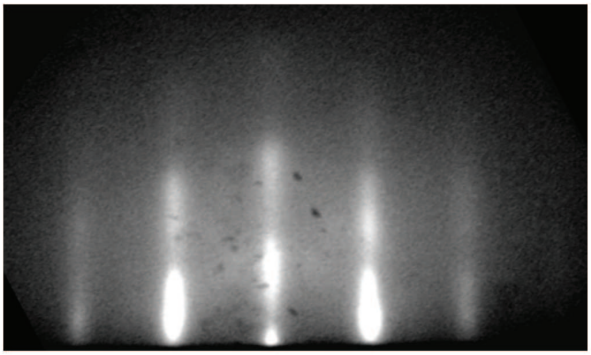

Fig. 6.1: RHEED pattern showing crystalline growth of home-grown MnSi thin films using a co-deposition MBE technique. Signs of 3D growth is also seen, but epitaxial growth is still indicated. Image reprinted with permission from C.Pohl of EPIII.

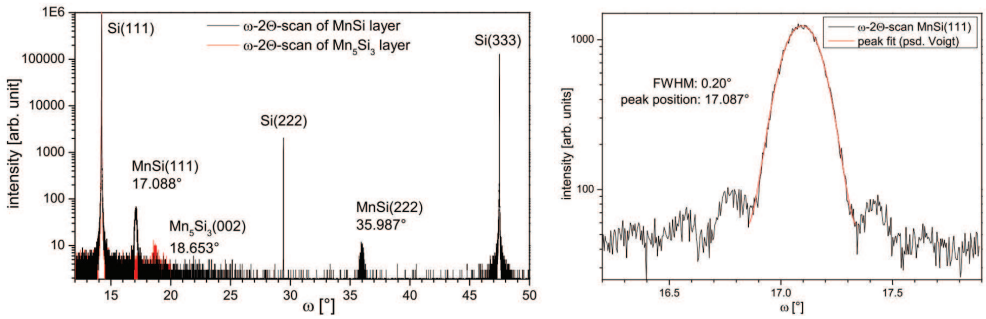

Fig. 6.2: Preliminary measurements were performed on the home-grown MnSi samples to measure the crystalline quality of the films. On the left shows superimposed XRD wide angle ω scans for MnSi in 1:1 and 5:3 stoichiometries, known metallic Mn:Si stoichiometries. On the right shows the $\omega - 2\Theta$-scan with a pseudo-Voigt peak fit to extract the FWHM. The peak fringes correspond to a thickness of $\approx$20 nm. Figures reprinted with permission from C.Pohl of EPIII.

6.2 Material Characterization

In order to extract more information regarding the characteristics of the grown films, both structural and magnetic measurements were performed. Both SQUID magnetization and X-ray Diffraction (XRD) measurements were done to confirm the possible presence of MnSi in the samples and compare them with the existing literature values on MnSi[111]on Si[111] growth. We focus our analysis mainly on two samples, one 12-nm and one 20-nm MnSi thin films both grown with a-Si cap layers.

6.2.1 Structural Characterization

XRD measurements were done to confirm the structural characteristics of the grown MnSi films. This is to at least, as our starting point, establish agreement of physical

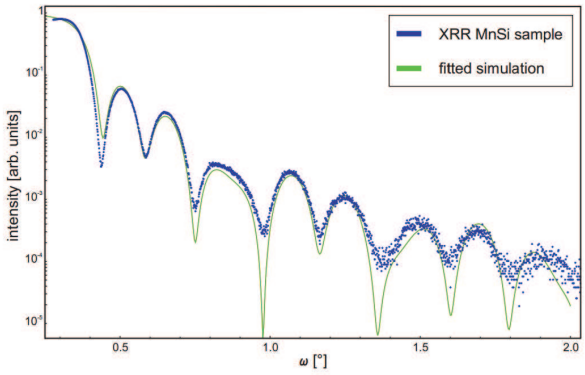

Fig. 6.3: XRR measurement of the 20-nm layer with superimposed two-layer simulated curve. The extracted layer thickness agrees with the XRD measurements of the same film. Other parameters such as cap thickness and interface and surface roughness were extracted for a fuller description of the physical characteristics of the layer. Measurements and figures reprinted with permission from C.Pohl of EPIII.

characteristics of the grown films to literature values for both bulk and thin film MnSi. Shown in Figure 6.2 are the results of the XRD and XRR measurements performed by C. Pohl of EPIII. Here we discuss key results which would strongly suggest the grown films as epitaxially-grown thin layers of MnSi. In Figure 6.2, the $\omega - 2\Theta$ XRD data on the left shows the MnSi peak in the ω scan with the peaks (in red) for Mn_3Si_5 for comparison. On the right is an $\omega - 2\Theta$ scan on the 20-nm layer showing pseudo-Voigt fit showing good fit. The scan shows fringes on both sides and the fringe period calculated from the fitting corresponds to a thickness of 20.6 nm. From the XRD measurements, several other characteristics of the film can also be extracted such as the average lattice constant and crystallographic relation of the grown film in relation to the Si[111] substrate. The measured crystallographic orientation of the grown films follow MnSi[111]||Si[111] and MnSi[$2\bar{1}\bar{1}$]||Si[$10\bar{1}$], consistent with [Zhan 02] and [Suto 09]. The average measured lattice constant is 4.545$\mathring{A}$, -0.34% off from the literature value. Of course, the presence of other (non-magnetic) Mn:Si stoichiometries are still possible and can only be resolved by further testing, especially high resolution TEM imaging for checking crystallinity, etc.

The XRR measurement on the 20-nm layer is shown Figure 6.3 with fitting to extract physical parameters of the film. Using a two layer model to simulate the layers, good fit with the experimental data is achieved. The oscillations of the cap layer is superimposed with those of the MnSi layer. From the XRR measurement, the following parameters were extracted: thickness d_{MnSi} = 20 nm (nominal: 20.6 nm), (amorphous) Si cap thickness d_{Sicap} = 7.9 nm (nominal: 7 nm), interface roughness MnSi/Si cap = 0.1 nm and surface roughness Δ_{MnSi} = 0.1 nm.

The XRD and XRR measurements show strong indication of MnSi presence within the grown layers, consistent with literature values which bodes well with the establishment of growth parameters of the material. Both measurements show a relatively homoge-

nous thickness and interface. However, the presence of other Mn-Si stoichiometries (e.g. $MnSi_{1.7}$, Mn_3Si_5) and defects cannot be completely removed from the measurements and can only be confirmed with further calibration of epitaxial growth and possibly by methods such as high resolution microscopy (i.e. TEM).

6.2.2 Magnetic Characterization

SQUID magnetization measurements were performed on the grown films to extract certain parameters pertaining to the magnetic characteristics such as the strain induced uniaxial anisotropy. The SQUID measurements were performed together with Ts. Naydenova of EPIII. The applied field for each in-plane measurement is along the MnSi[$1\bar{1}0$] direction and MnSi[111] for the out-of-plane geometry.
For the in-plane remanent magnetization measurement, multiple transitions are observed which is consistent with the observations for MnSi thin films with the existence of helical, helicoidal and ferromagnetic phases. For both the 20-nm and 12-nm thin films, the M-H curves show sharp transitions along the [111] crystal plane with very small hysteresis, which indicates a hard axis along [111]. The SQUID measurements are qualitatively consistent with the results from other groups, as shown in Figure 6.4.

SQUID measurements were also to measure parameters for calculating the anisotropy constants. We calculate the anisotropy constants, following [Karh 12], using the following equations:

$$\mu_0 H_{c2}^{\perp} = \frac{2K_0}{M_s} + \frac{2K_u}{M_s} + \mu_0 M_s \tag{6.1}$$

$$\mu_0 H_{c2}^{\parallel} = (2K_0 - K_u - K_m) M_s^{-1} \tag{6.2}$$

$$K_0 = \frac{M_s}{6}(\mu_0 H_{c2}^{\perp} + 2\mu_0 H_{c2}^{\parallel} - \mu_0 M_s + \frac{K_m}{M_s}) \tag{6.3}$$

$$K_m = \mu_0 M_s \frac{L_D}{4\pi d}[1 - exp(-2\pi \frac{d}{L_D})] \tag{6.4}$$

$$K_u = \frac{M_s}{3}(\mu_0 H_{c2}^{\perp} - 2\mu_0 H_{c2}^{\parallel} - \mu_0 M_s - \frac{K_m}{M_s}) \tag{6.5}$$

where K_0 is the effective stiffness of the spin wave, K_m the stray-field contribution, K_u the uniaxial anisotropy induced by the growth strain and M_s is the saturation magnetization.The magnetic field strength $H_{c2}^{\perp}$ and $\mu_0 H_{c2}^{\parallel}$ are the in-plane and out-of-plane values magnetization for the conical-induced ferromagnetic state transition.(see Figure 6.5) Of course, this is under the assumption of the single helix ground state and weak uniaxial anisotropy ($K_u \ll K_0$) from the growth strain.[Karh 12] From these constants, we can also calculate the critical fields $\mu_0 H_h = \frac{\pi^2 K_0}{16 M_s} = 0.617 H_D$. From these values we can also extract the spin wave stiffness A = $\frac{2g\mu_B K_0}{Q^2 M_s}$ and the DM constant D. These fields represent threshold fields between helicoidal and saturated states for the in-plane geometry, where

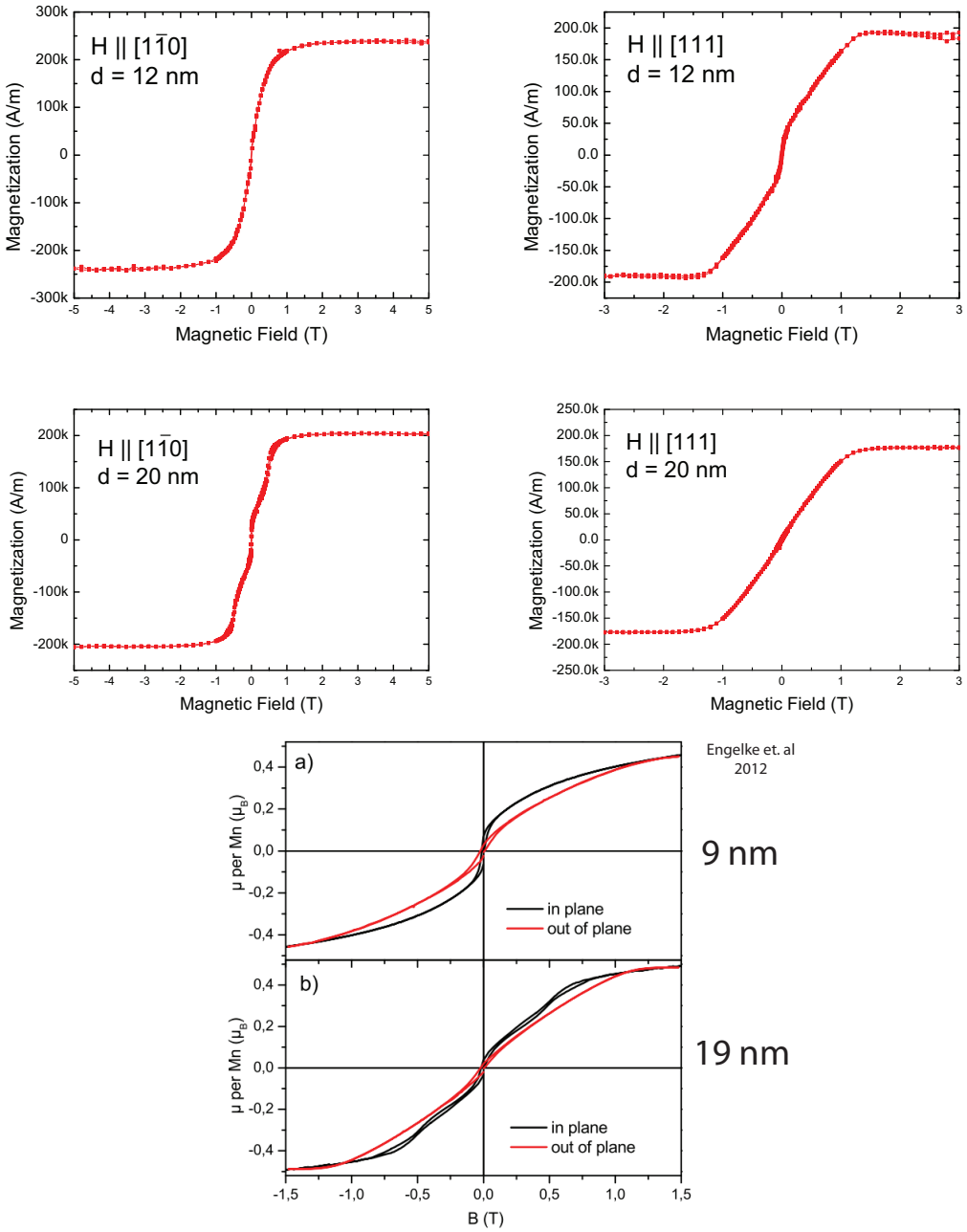

Fig. 6.4: SQUID results for the 12 and 20-nm thick grown Mnsi layers. In contrast with that of the 20 nm layer, the in-plane measurement for the 12-nm layer shows no intermediate magnetic phase transitions beyond the sharp transition near zero field and saturation at high fields. The in-plane and out-of-plane measurements show no hysteresis for both magnetic field sweeps. Both sets of measurements are qualitatively consistent to SQUID results from films of similar thickness by [Karh 11] and [Enge 12] The diamagnetic background for these measurements have been extracted by interpolation of the linear background. Reference SQUID data from [Enge 12] for 9 and 19 nm thick MnSi films grown by MBE co-desposition technique. The obtained magnetization for home-grown samples 12 and 20 nm thick (± 1-2 nm from XRR measurements) behave qualitatively similar to this data. Magnetization measurements performed with Tsvetelina Naydenova. Reprinted SQUID data from [Enge 12].

the helix turns into 360° domains (isolated Skyrmions). For the 20 and 12-nm thick layers we calculate the following parameters using Equations 6.5(±10 - 15% because of the uncertainty induced by the diamagnetic background for H‖[111] measurements (see Figure 6.5)):

Extracted anisotropy constants		
Parameter	20 nm	12 nm
K_m (TkA/m)	2.87	7.04
K_0 (TkA/m)	83.04	91.22
K_u (TkA/m)	6.42	19.70
$\frac{K_u}{K_0}$	0.077	0.220
$\mu_0 H_D$ (T)	823 mT	741 mT
$\mu_0 H_h$ (T)	508 mT	458 mT
A (meV nm^2)	0.42	0.47
D (meV nm)	0.189	0.212

Tab. 6.1: Anisotropy and critical field parameters extracted from SQUID measurements following [Karh 12].

The saturation magnetization M_s used for the calculations are from the in-plane measurements because this geometry avoids a paramagnetic contribution arising from the geometry of the measurement. The calculated parameters are shown in Table 6.1. The positive values for K_u suggest an easy plane anisotropy. The decrease of K_u with increasing thickness is consistent with the results presented in [Karh 12]. As for the values of μH_D, [Wils 13] presented an average value of 770mT for MnSi thin films, which is consistent with the values for both samples within the measurement error. From Figure 5.7, the values for $\frac{K_u}{K_0}$ agree well with the measured values from [Karh 12] for MnSi layers with thickness close to the measured films. (e.g. 19.4 nm and 14.6 nm films in [Karh 12]) The values for the spin wave stiffness A ($\approx$ 0.50meV nm^2 in [Ishi 77]) and the DM constant D ($\approx$ 0.18meV nm) for both films agree within error for bulk MnSi values and extracted from values in epitaxially-grown films in [Karh 12].

6.3 Device Fabrication

To measure the magnetotransport properties of the grown layers, they are fabricated into Hall bar structures using UV photolithography. The pattern used (with dimensions noted) is shown in Figure 6.6. Knowledge of device dimensions are important for subsequent calculations such as converting for resistivity values ($\rho = \frac{RA}{L}$).

The fabrication process is shown schematically in Figure 6.7. The contacts are defined by UV photolithography and metal deposition (steps a-b). After cleaning and metal lift-off,

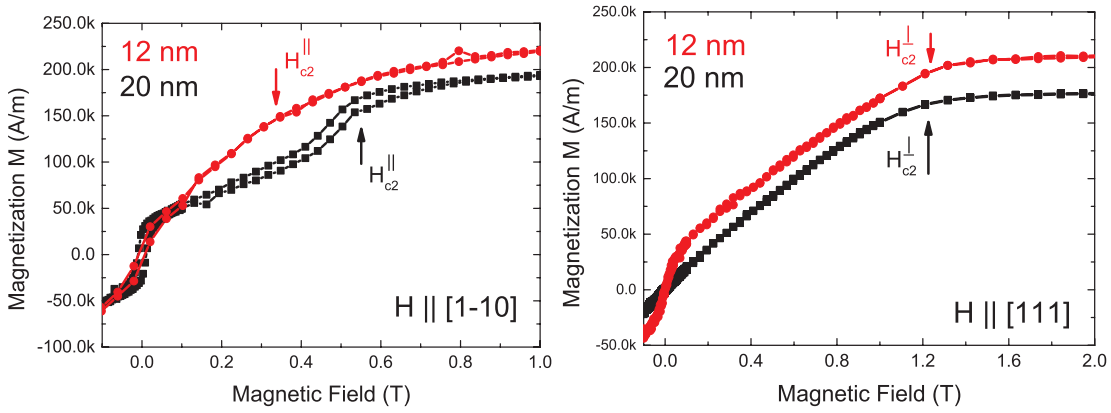

Fig. 6.5: Location of the H_{c2} fields used for the calculation of magnetic parameters from SQUID measurements. Because of the paramagnetic background from the out-of-plane geometry, an error is introduced in extracting the value for the out-of-plane saturation magnetization.

the mesa is defined by deposition of Ti metal mask. (steps c - d) The fabrication process makes use of a dry etching method for accurate definition of the Hall bar mesa. The Ti/Au contacts (10 nm Ti/120 nm Au) and Ti mask (thickness dependent on the MnSi thickness) for plasma etching are both deposited using resistive evaporation. The samples are then dry-etched using the CAIBE facility with a 5:3 Chlorine/Argon gas mix at 400V and 150W plasma voltage and power. The etch rate is found to be on the average 1 nm every 6.5 seconds for the MnSi layers. The Ti mask left by the etching process in then removed with low concentration 1:200 HF:DI H_2O_2 for controlled cleaning. (steps e - f)

Because of the thin silicon capping layer, the layers are protected from HF and the MnSi layer is protected from chemical exposure to the strong acid used to remove the remaining metal mask. After cleaning, the samples are wedge-bonded with gold wires onto a chip

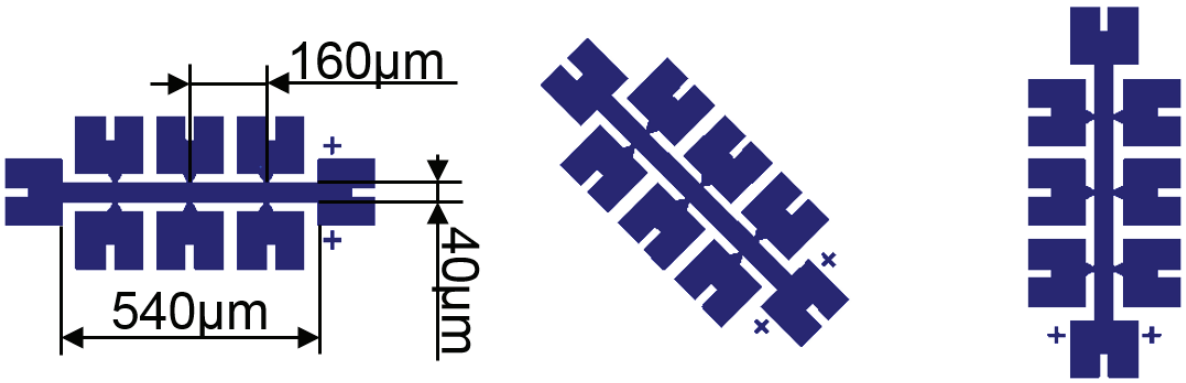

Fig. 6.6: Hall bar mask used for the defining the devices used for this work. The contacts and mesa were all defined using UV photolithography.

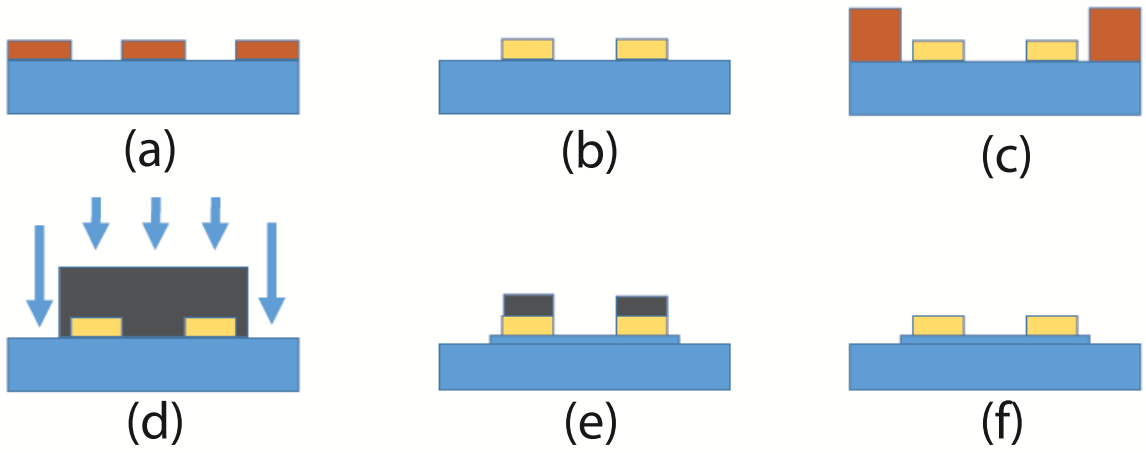

Fig. 6.7: Device fabrication steps used for making the Hall bar used for the transport measurements. Steps (a) to (b) show the metallization process for the Ti/Au metal contacts. Steps (c) and (d) show the fabrication of the Ti mask used in the dry etching process step for defining the mesa. Steps (e) and (f) show the final cleaning steps in HF removal of residual Ti mask before wire bonding.

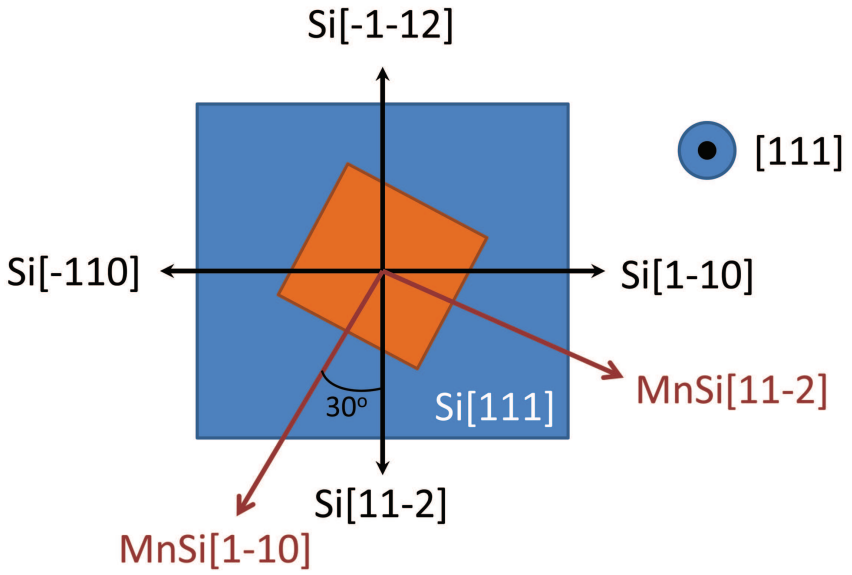

Fig. 6.8: Relative crystal directions between epitaxially-grown MnSi(111) thin films and the Si(111) substrate showing 30deg tilt for the top layer. The out-of-plane crystal directions are still parallel to each other MnSi[111]||Si[111].

carrier for electrical and magnetic measurements. In epitaxially-grown MnSi thin films, the B20-crystal is skewed by 30° from Si[111] substrate as was shown in Figure 5.5. We use Figure 6.8 as our guide in determining the relationships between magnetic and electric field parameters with respect to crystal directions.

The directions of the Hallbars used for this work is summarized in Table 6.2, noting both

crystal directions along the Si substrate and MnSi epitaxial film. This information would be important to remember for the comparison and analysis of subsequent magnetotransport measurements.

Hall bar crystal directions		
Hall bar	Si[111]	MnSi[111]
20 nm A	$15° off [10\bar{1}]$	$[\bar{2}\bar{1}3]$
20 nm B	$[01\bar{1}]$	$[1\bar{1}0]$
12 nm A	$[1\bar{1}0]$	$[01\bar{1}]$
12 nm B	$[\bar{1}\bar{1}2]$	$[\bar{2}11]$

Tab. 6.2: Si and MnSi crystal directions for all Hall bars measured for this work using the guide from Figure 6.8.

The Hall bars were measured in standard He_4 cryostats using an XYZ vector magnet for the low field measurements such as in-plane magnetoresistance and planar Hall effect measurements and high field magnets for Hall measurements. All electrical measurement results were obtained using standard lock-in techniques. Both systems are cooled down to Helium temperatures at 4.2 K. For accurate cooling curve measurements, the temperature-dependence of the sample resistivity was measured through a controlled warm-up process. All measurements were done after zero field cooling unless noted otherwise.
The transverse contacts were also measured at in-plane low field. Because of the very low resistivity of the MnSi layer and relatively higher contact resistances (e.g. ratios of 1:1000), the voltage drop across Hall contacts were within the limits of the AC measurement setup for most of the samples. As an example, The 20-nm thin film, with a four-terminal longitudinal resistance of 600 to 750 ohms and measured at 13 Hz using a EGG Model 124 lock-in set-up yielded a four-terminal Hall contact resistance of the order 200 to 500 mΩ.

6.4 Temperature-dependent measurements

As a first comparison to confirm some properties of MnSi in our sanmples, the resistivity of the samples (zero-field cooling (ZFC)) were first measured with respect to temperature. The resistivity versus temperature curve for the the 20-nm layer is shown in Figure 6.9. Both samples show similar behavior with $T_{ord} \approx 40$K. The geometry used for measuring longitudinal resistivity is shown in Figure 6.6.

There is good qualitative agreement between behavior of the experimental temperature-dependent resistivity curve (black) in Figure 6.9 compared to the temperature-dependence of bulk MnSi resistivity from literature.[Petr 06] A sharp change in the resistivity curve, which could not be fitted with both smooth functions, is as well evident in the vicinity of

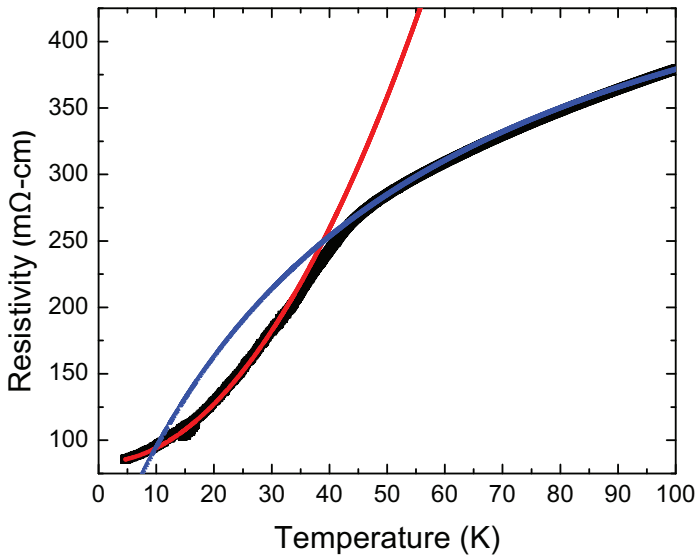

Fig. 6.9: Resistivity plot against temperature for the 20-nm thin layer. The resistivity curve (black) was fitted with a parallel resistor equation at T > Tc (red) and a power law at T < Tc.([Mena 03]) The exponent for the power law dependence of the resistivity at below Tc is calculated ≈ 2.0 for the 20-nm layer, which fits the expected Fermi liquid behavior.

T_c of the resistivity curve. This is usually identified as the transition region between the helical-paramagnetic phase in bulk samples.[Petr 06] An average of $T_c \approx 40$K is observed for both films, consistent with values reported in [Karh 10] and [Li 13]. A summary of the measured residual resistivity ratios, to see crystalline quality in the grown films, is shown in Table 6.3.

Residual Resistivity Ratios	
Thickness	ρ_{300K}/ρ_{4K}
12 nm	13
20 nm	6 - 7

Tab. 6.3: Measured RRR values for the films measured in this work. The value for the the 12 nm layer is similar to the reported values from [Li 13] for their 10 nm layers, which suggest at least good crystalline quality for the thinner layer.

The experimental curve was fitted with two different formulas for the different temperature ranges, as in Mena et. al.([Mena 03]) The red curve represents the temperature-dependent power-law fitting to the electrical resistivity starting at base temperature (4K) until T ≈ 30: $\rho(T) = \rho(0) + AT^{\mu}$, with calculated fitting parameters $\rho(0) = 166.2\,\mu\Omega$-cm, A = 0.22 $\mu\Omega$-cm-K^{-1} and $\mu = 2.0$. The factor approximates well the Fermi liquid T^2-dependence

expected for the helimagnetic phase.([Mori 79]) The T^2 contribution at low temperatures also follow the resistivity contribution mainly from the s-d interaction, with spin-ordering following the transition to ferromagnetic order at lower temperatures.[Kasu 59, Camp 82] This behavior is in contrast with the predicted $T^{5/3}$-behavior for weak itinerant ferromagnets at high temperatures.[Mori 85] For T > 40K, a parallel resistor formula was used to fit the data: $\rho_p(\mathrm{T}) = [1/\rho_\infty + 1/\rho' T]^{-1}$.([Wies 77]) For the 20 nm layer, it was roughly calculated that $\rho_\infty = 1.13$ m$\,\Omega$-cm and $\rho' = 23\ \mu\,\Omega$-K^{-1}. The values obtained are much larger than for values in bulk ([Mena 03]) and we attribute this to the presence of disorder in the sample inferred from the low residual resistance ratio $\mathrm{RRR} = \rho_{300K}/\rho_{4K}$ compared to bulk MnSi.

6.5 Summary

From the preliminary characterization techniques used, we show that the grown MnSi thin films have good correspondence with the results presented in literature for both bulk and MBE-grown samples. In the next chapters, we focus on the magnetotransport signatures for the 20- and 12-nm MnSi thin layers, which should help the at least illustrate some aspects of the actual magnetization structures present in these films.

Chapter 7

Magnetotransport with H ∥ [111]

In this chapter, results of magnetotransport measurements with the applied field directed parallel to the [111] hard axis plane are discussed. The current issue of the Skyrmion lattice stabilization with out-of-plane fields and its topological contribution to the Hall effect are topical to the current developments in the study of MnSi and are central to the discussion presented here.

7.1 Hall Measurements

Hall bars from 12 and 20-nm MnSi thin film layers were measured in an out-of-plane magnetic field ranging from 3T to 12 T using a liquid N_2-shield He cryostat connected to a PS Oxford magnetic power supply, sweeping the field at both directions. Multiple Hall bars oriented along different crystalline directions are fabricated. (See Table 6.2) Simultaneous AC measurements of both the magnetoresistance and the Hall voltage using standard six-terminal configuration are all performed using EG&G Princeton Applied Research Model 124 analog lock-in amplifiers at 13Hz.

Shown in Figure 7.1 are representative MR measurements on the 12 nm layer with currents along different crystal directions. The large negative magnetoresistance is consistent with observation of giant negative magnetoresistance in MnGe samples with the suppression of spin fluctuations and increased magnetic ordering along the field.[Li 07] The longitudinal magnetoresistance measurements show no preferred crystal direction for the current, which shows that the MnSi[111] is a magnetic hard axis separate from the in-plane anisotropies, consistent with out-of-plane SQUID results.(Figure 6.4) However, we measure a hysteresis between consecutive sweeps of the applied field, shown in Figure 7.2. This poses a problem in the subsequent symmetrization calculations since we actually symmetrize on H, not on $B = \mu\ (H + M)$.

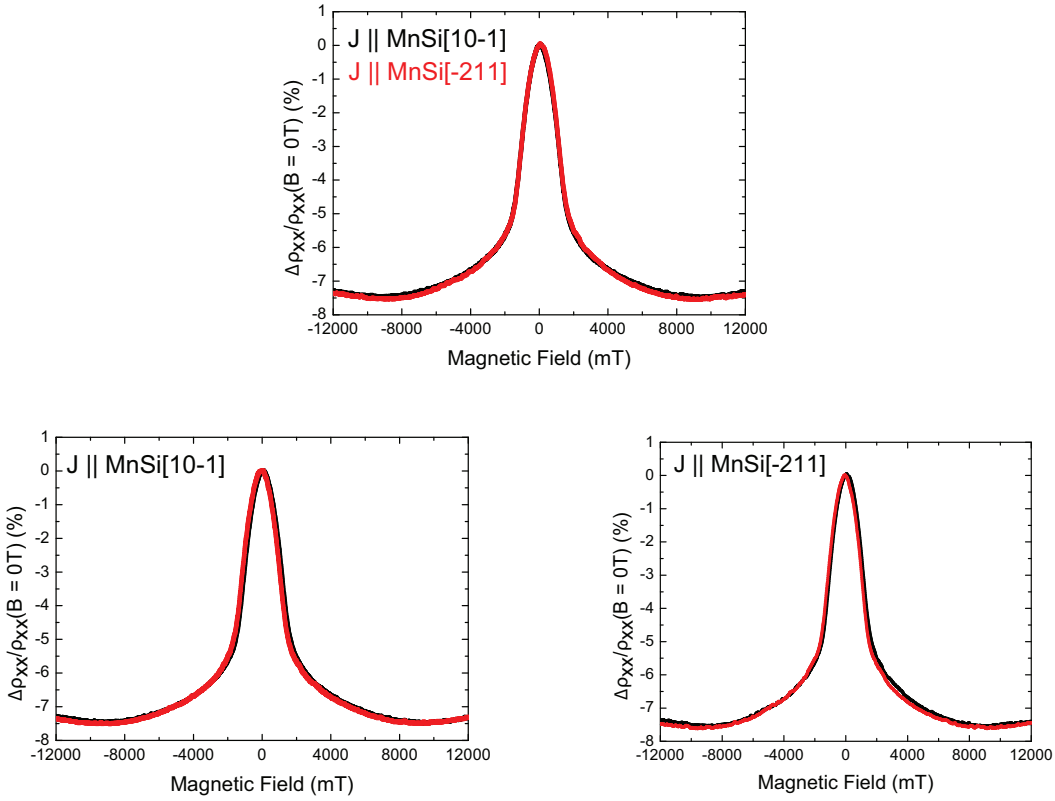

Fig. 7.1: Result from low temperature Hall measurements for 12 nm layer at a saturation field of ±3T with countinuous field sweep rate of 100mT/min and current direction along [1-10]: (a) Actual measured signal with contributions from the longitudinal component of the Hallbar, (b) The extracted Hall signal (asymmetric) and (c) resistance corrections from the longitudinal resistance (symmetric). The symmetric contributions arise from misalignments during the lithography process.

Why the need for symmetrization? Symmetrization of the data needs to be done with respect to field to extract only the asymmetric component for parameter fitting. The symmetric component is attributed to imperfections in lithography. The Hall effect is odd under field direction following Onsager relations.[Onsa 31a, Onsa 31b] We follow the method from [Ritz 13a], wherein they symmetrized their Hall measurements by combining forward and backward field sweeps, resulting in a single magnetic field dependence. A similar process was done for the magnetoresistance measurements before parameter extraction.[Ritz 13a] However, the hysteresis between the measurements would always introduce an uncertainty in the symmetrization because of the magnetization M. This is important to remember for all the calculations involved, particularly in the extracted Hall parameters (i.e. focus on order of magnitude instead for comparisons) in this chapter.

In order to extract the Hall coefficients, we use the following general formula for the Hall

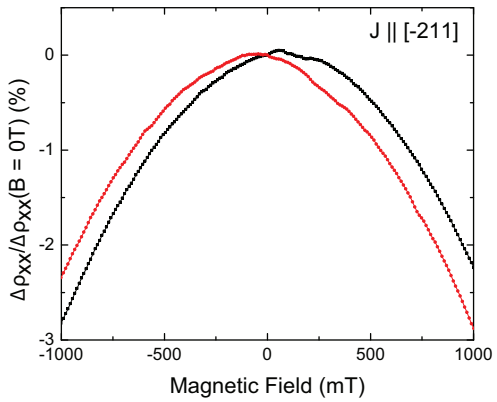

Fig. 7.2: Observed hysteresis on magnetic field sweeps for the longitudinal magnetoresistance. This hysteresis (from M) complicates and introduces errors into the symmetrization process of the measured Hall response.

resistivity, including the topological Hall term (chiral): [Li 13]

$$\rho_{xy} = R_0 B + (\alpha \rho_{xx} + \beta \rho_{xx}^2) M + \rho_{xy}^T, \tag{7.1}$$

where M and B stands for the magnetization and magnetic induction, R_0 the ordinary Hall coefficient and α and β for the anomalous hall (AHE) contributions for skew-scattering and intrinsic (side-jump) effects. ρ_{xy}^T stands for the topological Hall term arising from the net chirality of the system. For our calculations, we first tried following [Li 13] in including the α skew-scattering parameter in our calculations. The estimated relationship between the

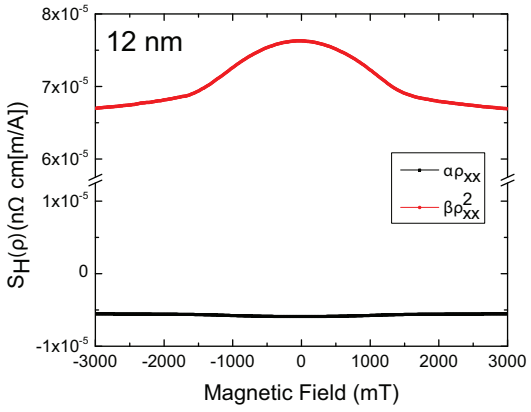

Fig. 7.3: Comparison of extrinsic and intrinsic scattering fitting parameters for the Hall measurement on the 12-nm layer at $\leq 10\%$ ratio. Ignoring the extrinsic scattering parameter α introduces only a slight error in the calculations of the scattering parameters and can be compensated by adjusting the intrinsic parameter β.

values of parameters (Figure 7.3) is at the maximum $\alpha\rho_{xx}/\beta\rho_{xx}^2 \approx 0.1$, which introduces a only slight error into the extracted parameters if using the simplification from [Lee 07] for thin samples. It can also be completely forced to be compensated by the other two parameters, as the longitudinal resistivity is at least four orders of magnitude larger than the (symmetrized) Hall resistance, consistent with the clean limit assumptions in [Lee 07]. For subsequent measurements we rely on the simplified formula: $\rho_{xy} \approx R_0 B + \beta\rho_{xx}^2 M + \rho_{xy}^T$.

Extracting the fitting parameters from high field measurements on the 20 nm layer (Figures 7.4 - 7.6), the calculated Hall coefficient R_H is measured as ≈ 17 nΩ-cm/T on average, which is higher than the results calculated in [Lee 07].($\approx$ 7 nΩ-cm/T) [Neub 09b] used a similar value for calculating the spin polarization P of the topological Hall effect at the A-phase, however with a smaller effective field of 2.5 T than [Ritz 13a] ($\approx$ 13T). A possible expanation would be a reduced carrier concentration in MnSi thin films arising

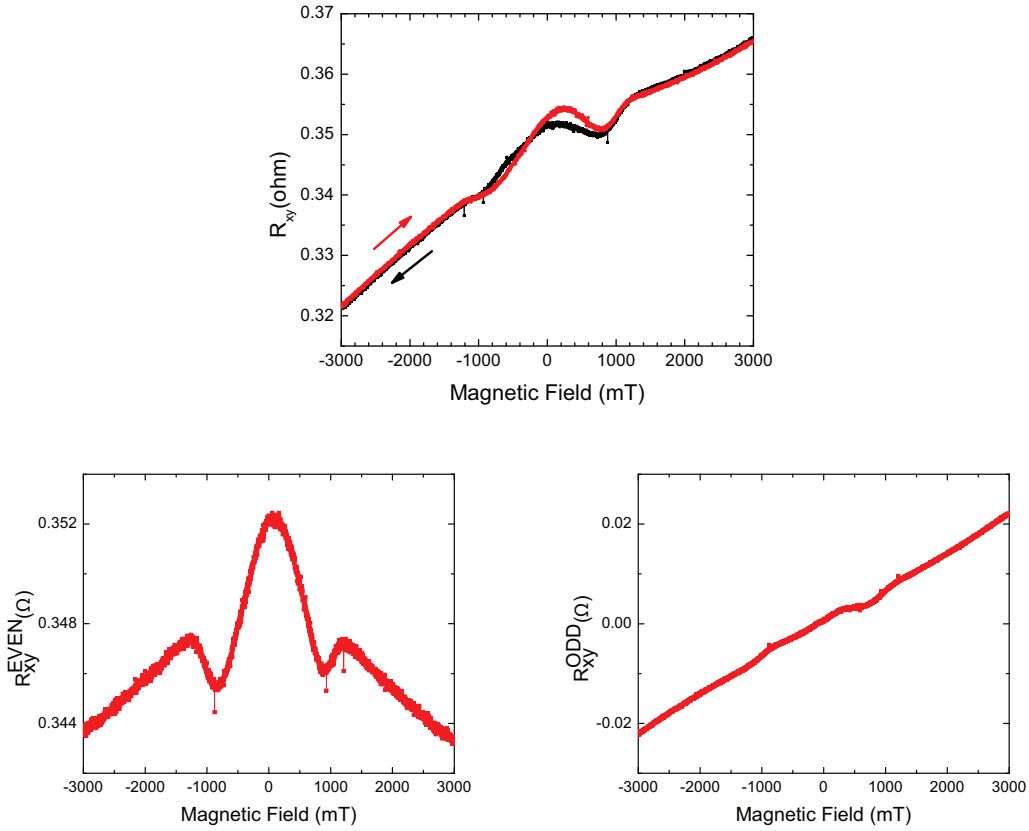

Fig. 7.4: Result from low temperature Hall measurements for 20 nm layer at a saturation field of ±3T with countinuous field sweep rate of 30mT/min: (a) Actual measured signal with contributions from the longitudinal component of the Hallbar, (b) The extracted Hall signal (asymmetric) and (c) resistance corrections from the longitudinal resistance (symmetric). The symmetric contributions arise from misalignments during the lithography process.

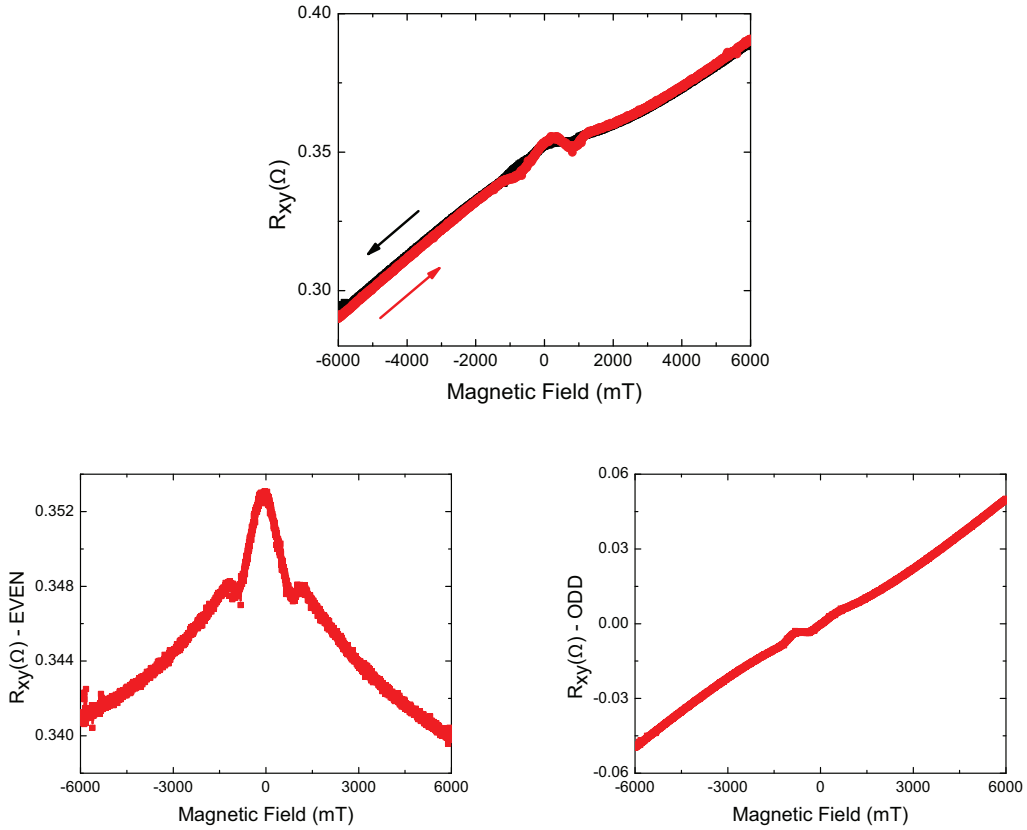

Fig. 7.5: Result from low temperature Hall measurements for 20 nm layer at a saturation field of ±6T with countinuous field sweep rate of 50mT/min: (a) Actual measured signal with contributions from the longitudinal component of the Hallbar, (b) The extracted Hall signal (asymmetric) and (c) resistance corrections from the longitudinal resistance (symmetric). The symmetric contributions arise from misalignments during the lithography process.

from the strain due to changes the bandstructure and thus the Fermi level.(see [Jeon 04]) For the 20-nm layer, the intrinsic scattering parameter β is at around $\beta \approx$ -10^4 V^{-1}, which is consistent with the order of magnitude of values from [Lee 07]. Shown in Figures 7.4 - 7.6 are the high field measurements for the 20-nm layer and their asymmetric and symmetric parts from the symmetrization process in [Ritz 13a]. Figures 7.4 and 7.5 are both measurements from the same lock-in setup and cryostat, while Figure 7.6 is from a sample measured at another cryostat. The extracted topological Hall signals for this film using the simplified formula are shown in Figures 7.7 - 7.9.

For the 12-nm thick layers (Figures 7.10 - 7.11), the ordinary Hall coefficient still measures in the same order of magnitude as the values from the 20 nm layer at $R_0 \approx 16$ Ω-cm/T, similar to the 20-nm layer. The calculated fitting parameter for the intrinsic anomalous Hall coefficient β for the 12 nm layer gives a value in the order of $\beta \approx$ -10^6 V^{-1}, which

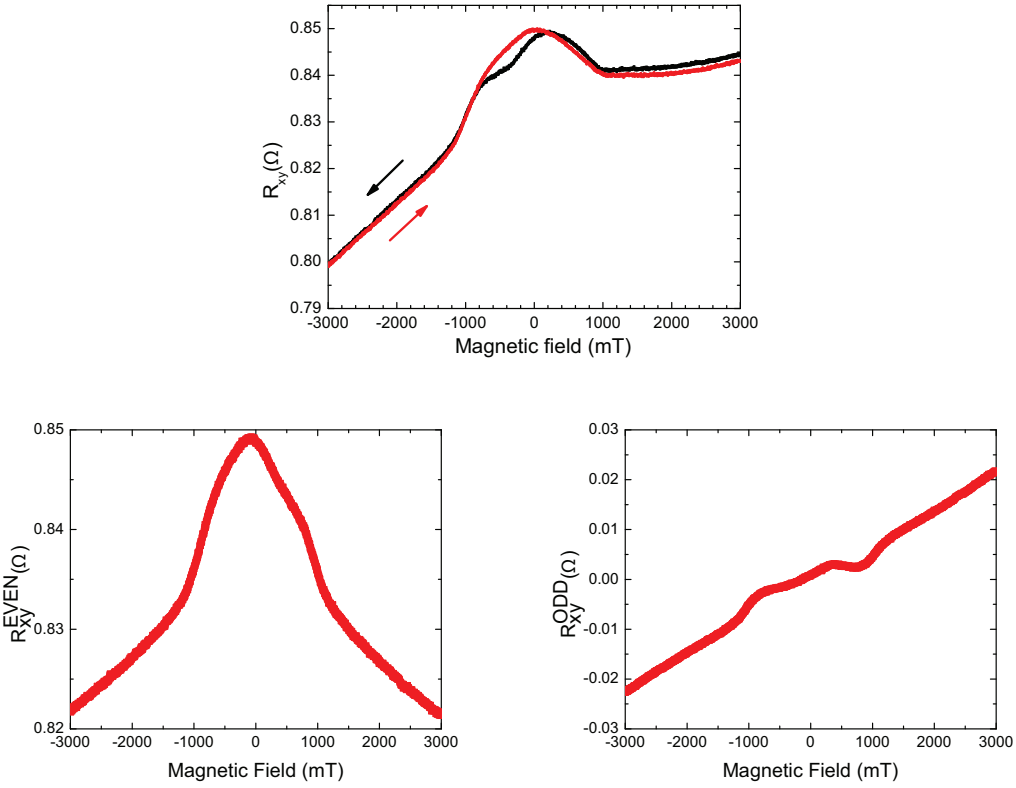

Fig. 7.6: Result from low temperature Hall measurements for 20 nm layer at a saturation field of ±3T with countinuous field sweep rate of 50mT/min: (a) Actual measured signal with contributions from the longitudinal component of the Hallbar, (b) The extracted Hall signal (asymmetric) and (c) resistance corrections from the longitudinal resistance (symmetric). The symmetric contributions arise from misalignments during the lithography process. This measurement was measured at a different cryostat than Figure 7.4 and Figure 7.5, which might have been the cause of the difference in measured Hall voltage.

is two orders of magnitude higher than that of Lee's results.[Lee 07] We can possibly attribute this to the effect of surface scattering due to the thinness of the layer [Gerb 02] wherein local contributions to the Hall effect becomes more important. [Enge 12] notes the decrease in the spin-spin interaction coupling range with decreasing MnSi thickness, which could also affect the extraordinary component. As for the order of magnitude of the anomalous contribution, an ehanced net chirality in the thinner film might also contribute to a higher anomalous signal.[Tata 02, Tagu 09] This can probably be supported by the higher RRR for the thinner film, which is higher than [Li 13] where they confirmed the crystallinity of their samples with high resolution TEM. The extracted topological Hall signals for this film using the simplified formula are shown in Figures 7.12 - 7.13.

As discussed in the preceding chapter, epitaxial growth of MnSi thin films result in the presence of an in-plane anisotropy due to the effects of growth strain, along with the hard axis and the helical propagation wavevector **Q** both oriented along [111]. In the single helix picture, with **Q** already pinned along the hard axis, the magnetic moments in the spin helix rotate continuously into a conical phase (H_{C1}) and, at a sufficiently strong field (H_{C2}), an induced- ferromagnetic phase where all spins are saturated along the field direction. Another magnetization state, the Skyrmion, is observed to occur at fields H||[111] near the A-phase, observed in an extended T - μH phase for lower dimensions. The topological cotribution to the Hall effect is used to indicate the presence of this Skyrmion lattice.

It seems that from the measurements, the magnitudes of the extracted THE signals for both the 12 and 20-nm thin films are consistent with value measured for bulk MnSi near T_c (-4 nΩ·cm) [Neub 09a], but slightly smaller than the values measured by [Li 13] at low tem-

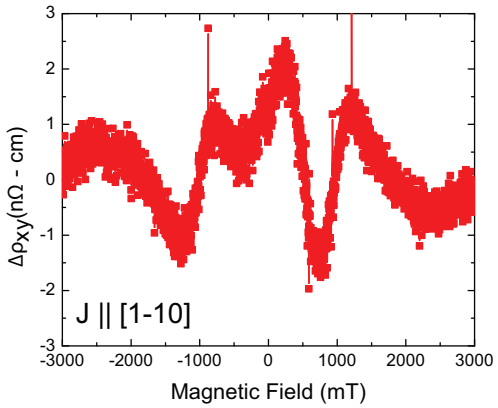

Fig. 7.7: Extracted signal $\Delta\rho_{xy}$ using the general Hall equation $\rho_{xy} = R_0B + (\alpha\rho_{xx} + \beta\rho_{xx}^2)M$ for the 3T saturation measurement at 30 mT/min sweept rate. This signal is usually denoted as the topological Hall signal.

peratures (-7.8 nΩ·cm). There is also an observed shift in the signal for higher saturation fields (6T for the 20 nm layer). This could be possibly be explained by differences in the saturation and relaxation processes in the magnetic states in the material.[Wind 12] For the 12 nm layers however, the sign of the topological Hall is reversed.(positive) This should violate the reversed sign relation between the normal hole-like ordinary Hall coefficient (positive) and the topological Hall signal.[Binz 08] This sign is actually consistent with the observed giant topological signal at high pressures for bulk MnSi near T_c by [Ritz 13a], albeit a much lower value. A positive topological signal is also observed by [Li 13] at low temperatures, but a sign reversal was observed for ρ_{xy}^T as the temperature changes ($T \leq$ 5K). They attribute this to changes in the bandstructure of the material and position of the Fermi level, affecting the spin polarization parameter P. [Jeon 04, Hort 08] We calculate this parameter from the topological Hall contribution (THE) $\Delta\rho_{xy} \approx PR_0B_{eff}$, where B_{eff} is the effective topological field arising from the Skyrmion lattice.[Neub 09a] It is plausible that surface effects in the thinner material and the higher induced uniaxial anisotropy ($K_u/K_0 \approx 0.22$) might contribute to the warping of the bandstructure and driving the polarization from a spin-up to spin-down majority state and vice versa.

The change in sign for magnetization direction is also consistent with the Skyrmionic chiral contribution of the bcc spin crystal[Binz 06a] to the Hall signal predicted in [Binz 08]. The calculated spin chirality induced effective field in this case is about 1.7 T, which might explain the low measured topological signal [Binz 08]. [Neub 09a] used a value of -2.5T for their calculation of P near T_c, wherein they used their measured THE signal of ≈ -4.5 nΩ·cm. In contrast, [Ritz 13a] calculates the effective field at -13T, consistent with their giant topological signal at ambient to fairly low pressures (≈50 nΩ·cm). It is clear that more detailed measurements are needed to resolve the nature of the mag-

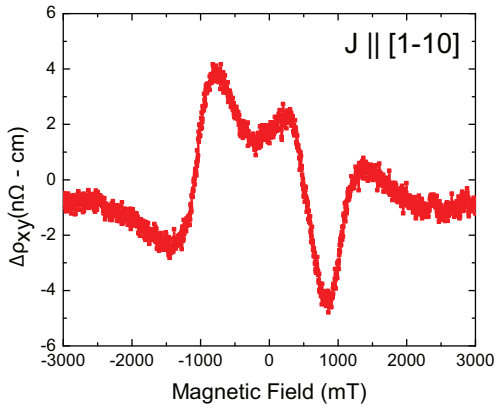

Fig. 7.8: Extracted signal $\Delta\rho_{xy}$ using the general Hall equation $\rho_{xy} = R_0B + (\alpha\rho_{xx} + \beta\rho_{xx}^2)M$ for the 3T saturation measurement at 50 mT/min sweept rate. This signal is usually denoted as the topological Hall signal.

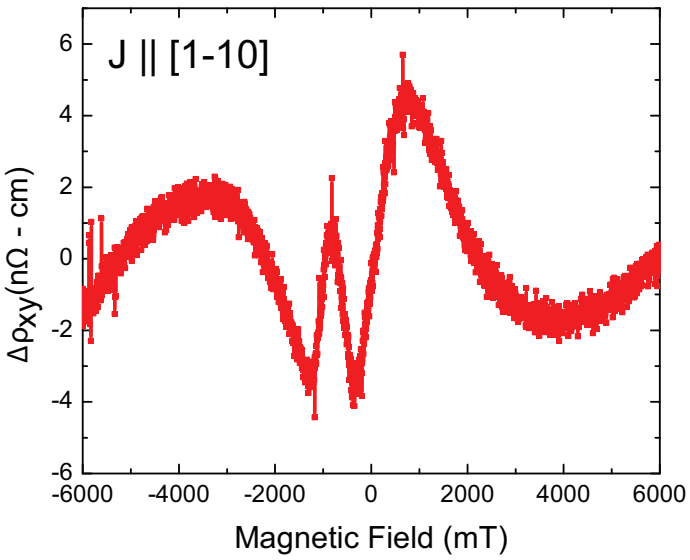

Fig. 7.9: Extracted signal $\Delta\rho_{xy}$ using the general Hall equation $\rho_{xy} = \mathrm{R_0B} + (\alpha\rho_{xx} + \beta\rho_{xx}^2)\mathrm{M}$ for the 3T saturation measurement at 50 mT/min sweept rate. This signal is usually denoted as the topological Hall signal.

netic states in these films. Aside from the need to perform further experiments such as Lorentz TEM to visualize possible Skyrmion formation or the real spin configuration in these films, there are still some experiments needed to clarify behavior such as differences in the extracted signals for different magnetic field sweep rates and saturation fields.

Recent works by Karhu et al. on epitaxially-grown thin MnSi films by Polarized Neutron Reflection (PNR) measurements reveal a plethora of other possible magnetization states. They also claim that this geometry (H||[111]) will result in an unstable Skyrmion state, which contradicts previous assertions from bulk MnSi. The Skyrmionic structures observed by [Li 13] using Lorentz TEM might discount this, but it must still be addressed that they do not show long range order typical of the Skyrmion lattice. Because of this, we still cannot discount the possibility that, in the region between the conical phase and ferromagnetic phase, another region is present that can result to an additional anomalous contribution independent of scattering. This can possibly be an intermediate phase transition between the conical phase and the ferromagnetic phase where both states co-exist or due to the distortions in the ideal helical spin structure (e.g. canting). Further measurements, particularly current dependent measurements at temperatures closer to the phase transition temperature may elaborate on what are the correct magnetic states to associate with the regions in the signal.[Schu 12]

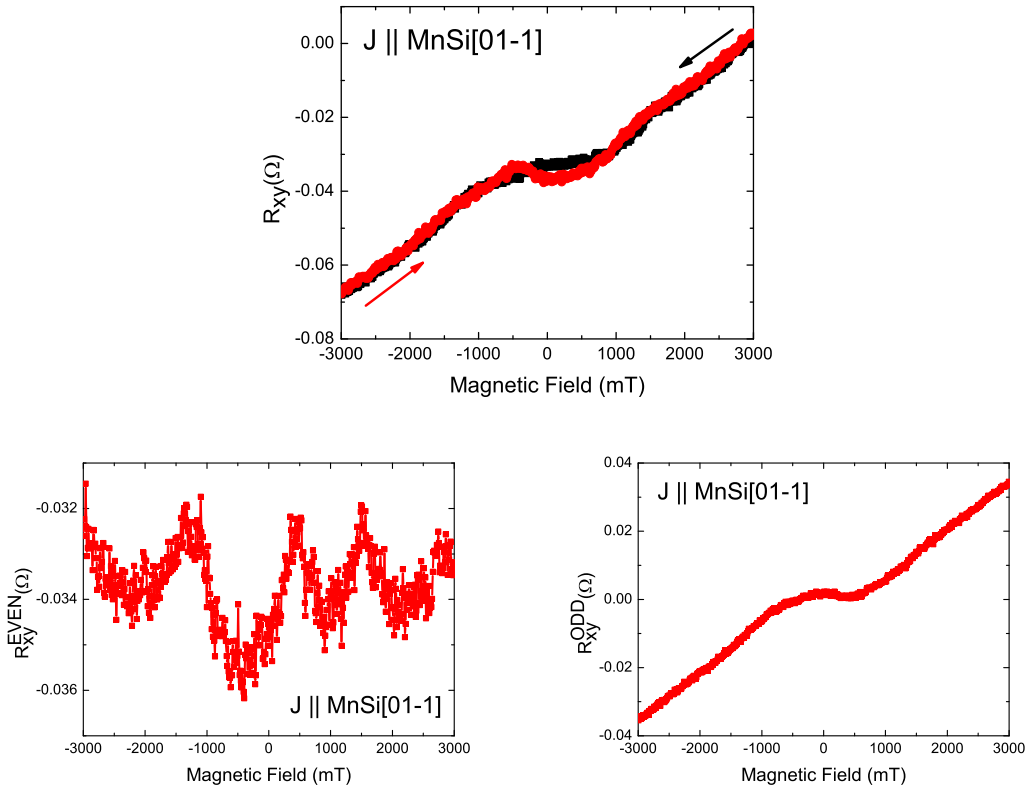

Fig. 7.10: Result from low temperature Hall measurements for 12 nm layer at a saturation field of ±3T with countinuous field sweep rate of 100mT/min and current direction along [01-1]: (a) Actual measured signal with contributions from the longitudinal component of the Hallbar, (b) The extracted Hall signal (asymmetric) and (c) resistance corrections from the longitudinal resistance (symmetric). The symmetric contributions arise from misalignments during the lithography process.

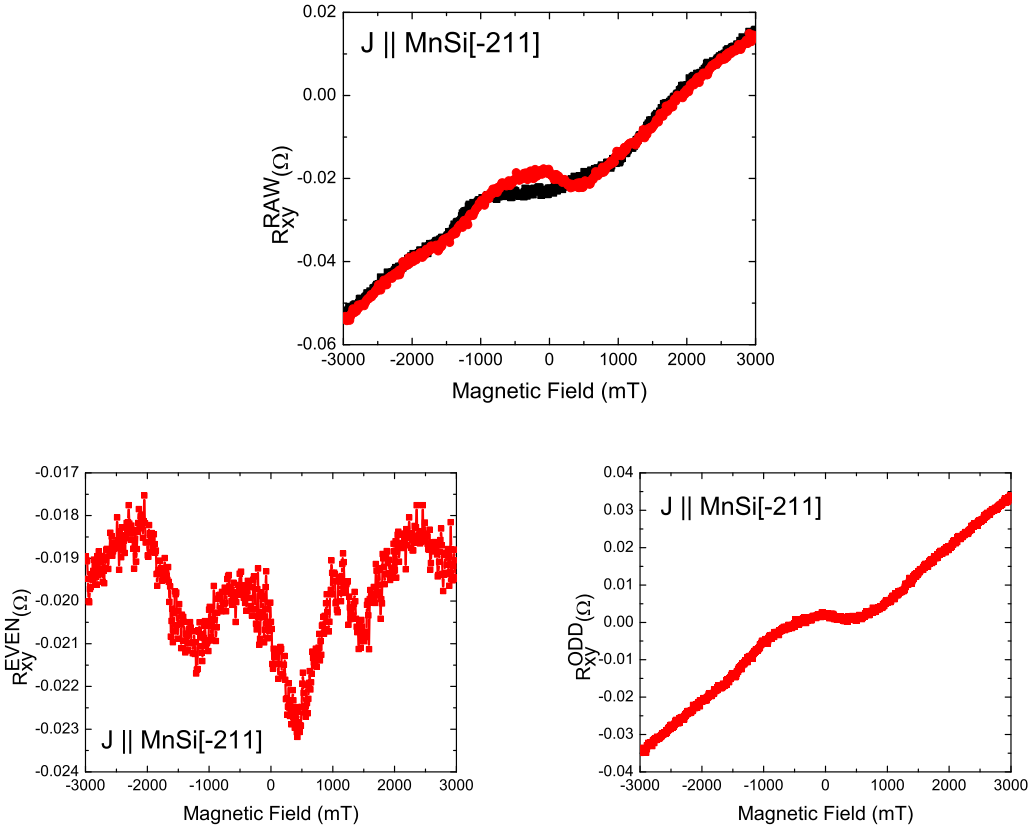

Fig. 7.11: Result from low temperature Hall measurements for 12 nm layer at a saturation field of ±3T with countinuous field sweep rate of 100mT/min and current direction along [-211]: (a) Actual measured signal with contributions from the longitudinal component of the Hallbar, (b) The extracted Hall signal (asymmetric) and (c) resistance corrections from the longitudinal resistance (symmetric). The symmetric contributions arise from misalignments during the lithography process.

7.1.1 Minor Loop Magnetization Dynamics

In order to study further the magnetization dynamics, we observe the behavior of minor magnetization loops. Measurements at different forward saturation magnetic fields are shown in Figure 7.14. For all the measurements, we concentrated on a single Hall bar with current and 0° magnetic field direction oriented along $[\bar{2}\bar{1}3]$. We did not symmetrize the data to observe the effect of the magnetization process on the hysteresis. Figure 7.14 shows magnetization loops at different forward sweep saturation magnetic fields, meaning the applied field before sweeping to positive fields. The hysteresis between forward and back sweeps of the magnetic field decreases as the sample is saturated closer to zero field.

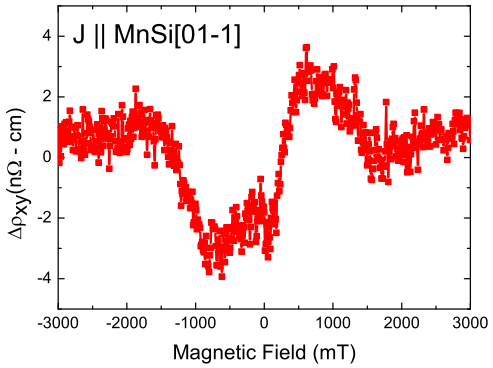

Fig. 7.12: Extracted signal $\Delta\rho_{xy}$ using the general Hall equation $\rho_{xy} = \mathrm{R_0B} + (\alpha\rho_{xx} + \beta\rho_{xx}^2)\mathrm{M}$ for the 3T saturation measurement with current along [01-1]. This signal is usually denoted as the topological Hall signal.

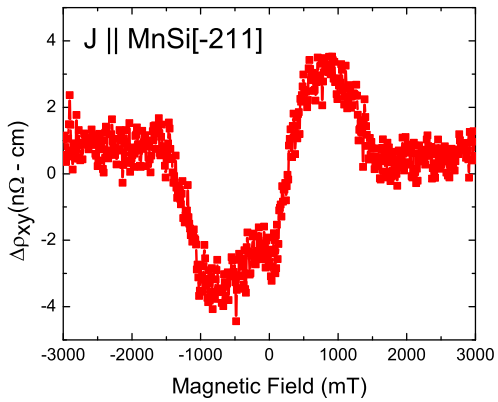

Fig. 7.13: Extracted signal $\Delta\rho_{xy}$ using the general Hall equation $\rho_{xy} = \mathrm{R_0B} + (\alpha\rho_{xx} + \beta\rho_{xx}^2)\mathrm{M}$ for the 3T saturation measurement with current along [-211]. This signal is usually denoted as the topological Hall signal.

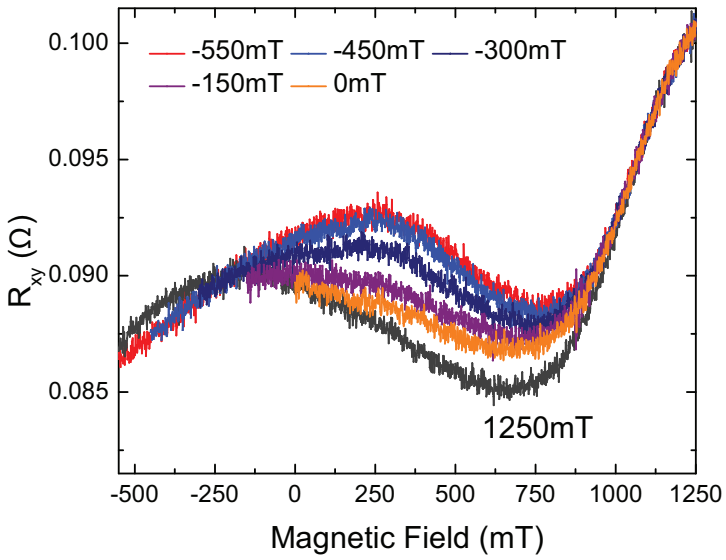

Fig. 7.14: Minor magnetization loops at different forward sweep saturation magnetic fields. The hysteresis between forward and back sweeps of the magnetic field decreases as the sample is saturated closer to zero field.

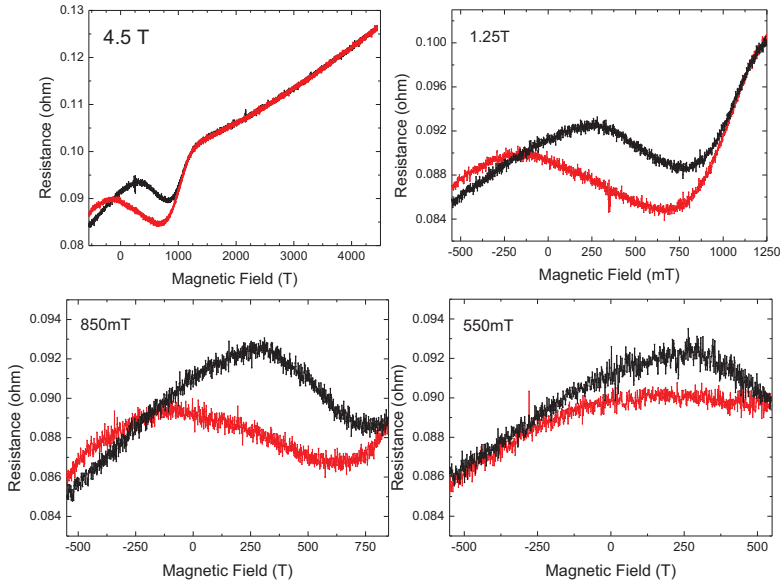

Fig. 7.15: Minor magnetization loops at different backward sweep saturation magnetic fields.The crossover (μH $\approx$ 100mT) disappears once the back sweep field is saturated before the Hall effect minima at μH $\geq$ 750mT.

Minor magnetization loops at different backward sweep saturation magnetic fields. The crossover between curves (μH $\approx$ 100mT) disappears once the back sweep field is saturated

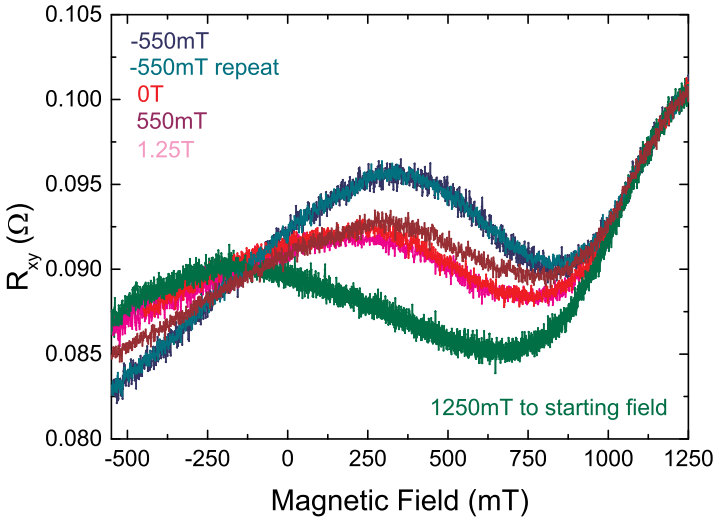

Fig. 7.16: Field-cooled Hall measurements at different applied fields. We saturate the sample at the end of the forward sweep at 1.25T. The observed hysteresis between the forward and backward sweep of the field is maximum at the highest applied negative cooling field. A slight increase in the hysteresis is also observed at cooling fields below the Hall effect minima at positive fields.

before the Hall effect minima at $\mu H \geq 750$mT.(Figure 7.15) The hysteresis is reproducible at final fields ≥ 1.25T. These measurements are consistent with the existence of multiple magnetic processes (e.g. upward and downward domain nucleation, annihilation) within the material with different time dependencies.[Wind 12] This might also be explained by the existence of both chiral domains in the material. The possible time dependence between processes might also explain the difference between the Hall measurements for different magnetic sweep rates. (Figures 7.4 and 7.6) We also establish the saturation fields where all processes stabilize and loops become reproducible for our next measurements. (1.25T)

7.1.2 Temperature-dependent measurements

In order to further investigate the behavior of the grown films, temperature measurements were done to observe the evolution of the magnetic behavior, particularly the observed hysteresis, at various temperature regimes. Steps were taken to ensure that the measurements have similar starting magnetic states. For the field dependent measurements at fixed temperatures, the samples are heated and cooled without field after each measurement for all samples to have the same (t-1) magnetic history. All field heating measurements are warmed well beyond the ferromagnetic-paramagnetic transition temperature ($T > 150$K) and cooled at zero field.

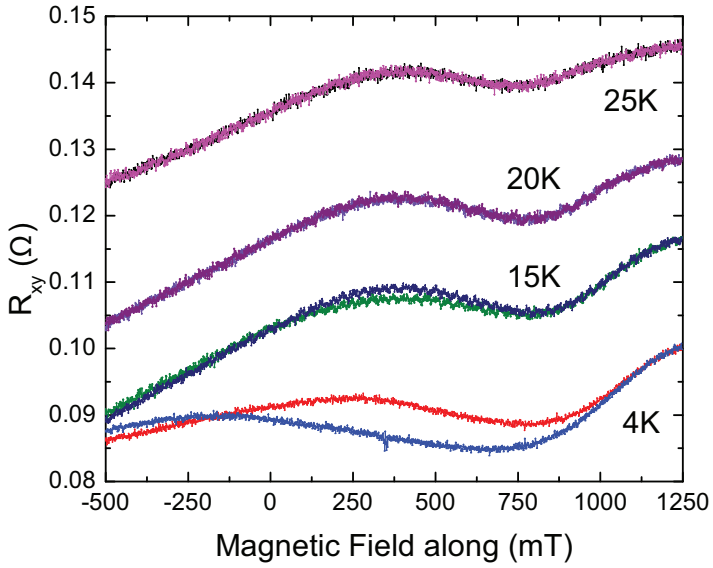

Fig. 7.17: Hall resistance curves from -550mT to 1.25T at T = 4, 15, 20 and 25 K. The observed hysteresis between the magnetization sweeps disappears at about 20 K.

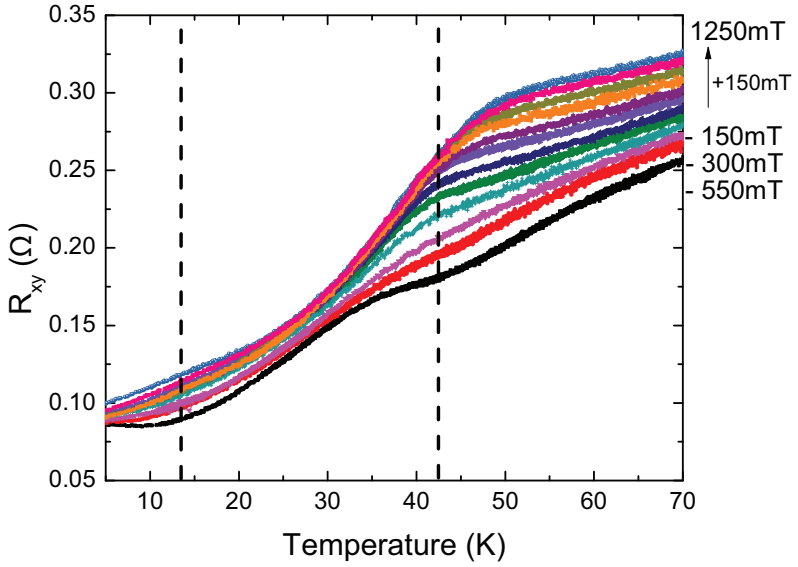

Fig. 7.18: Hall resistance with respect to temperature (field heating) for different applied fields.

Figure 7.16 shows four-terminal field-cooled Hall curves for the 20-nm layer with current and 0° magnetic field directions along [$2\bar{1}3$]. The sample was warmed up at zero field and cooled at an applied field before slowly ramping the magnetic field to zero at 4 K. After going to zero field, the magnetic field is then slowly ramped to -550mT and then

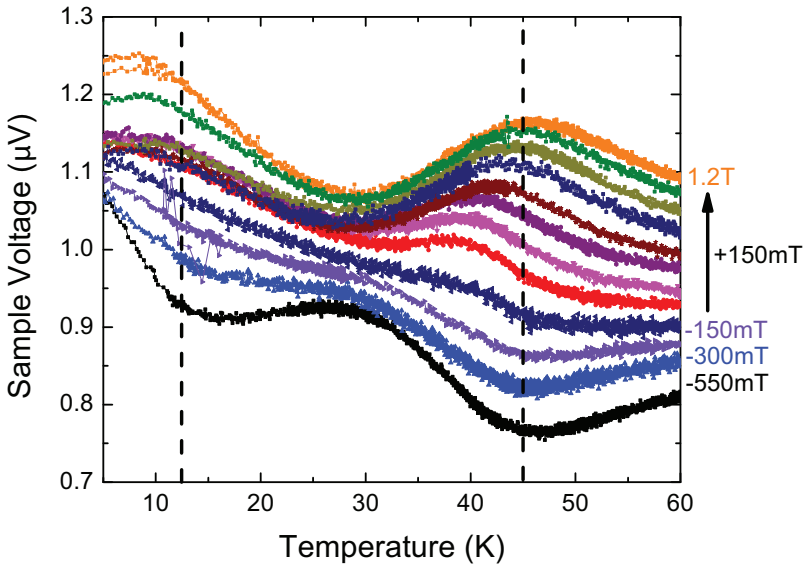

Fig. 7.19: Measured Hall voltage with respect to temperature (field heating) for different applied fields.

swept in a minor loop (-550mT to 1.25T) We use 1.25T since it was shown previously that the minor loop becomes macroscopically reproducible within this loop. (see Figure 7.16 and the repeated measurements for -550mT) We observe that the hysteresis decreases as the field is driven closer to the saturation field of 1.25T. However, the zero-field cooling follows closely instead the 1.25T curve. More measurements and thermal cyclings might be needed to ascertain the type of magnetization processes in the 20-nm layer.

We could again possibly attribute this to the asymmetry in the upward and downward magnetized enclaves in the sample.[Wind 12] In terms of our sample being a chiral material, we might attribute the macroscopic reproducibility of the loops to the saturation of the symmetry-breaking chiral parameter S of the material to a single chirality at an applied field. Field cooling with a high applied field is actually the suggested method in [Binz 07] for producing single chirality samples.

In Figure 7.17, it is seen that the hysteresis in the measured Hall resistance starts to disappear at around 10 - 20K, suggesting a magnetic phase transition occuring within this particular temperature range. A wide temperature range where the topological Hall effect and a broadened A-phase was observed on epitaxial films by [Li 13] at about the same range we have here. In order to gather more observations regarding on what occurs in this temperature regime, we need to measure the Hall voltage and Hall resistance at varying temperatures at different applied fields.

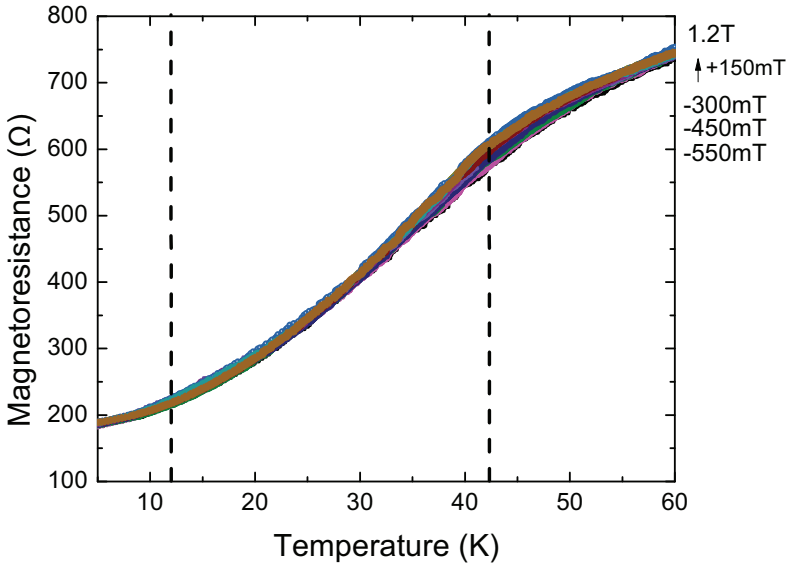

Fig. 7.20: Magnetoresistance with respect to temperature (field heating) for different applied fields. We can see an large monotonic effect near the transition temperature ≈ 42 K.

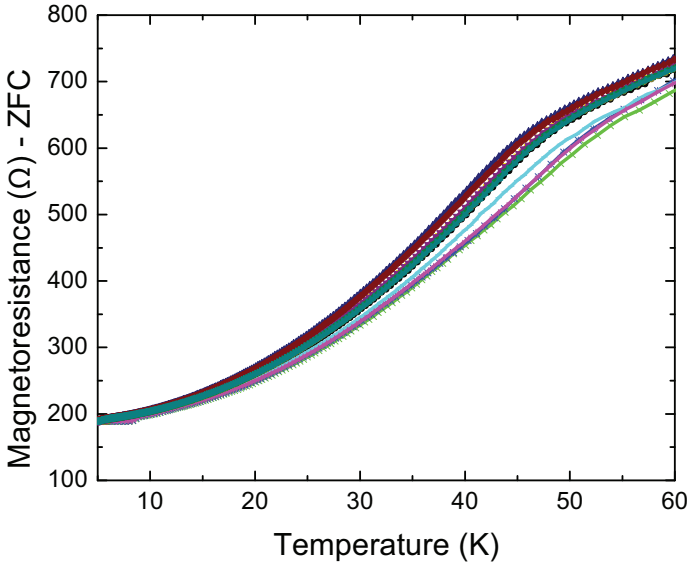

Fig. 7.21: Zero field four-terminal magnetoresistance cooling curves after field heating at different fields. We see a drift in the magnetoresistance drop near T_c. However, unlike with the field heating curves, the shift is not monotonic with field. We can attribute this to the non-uniformity of the cooling temperature sweep rate.

Figures 7.18 and 7.19 shows the measured Hall resistance and voltage with respect to

temperature. We see broadening features monotonic in field between 10 K and 45 K. We note no similarly broad change in the temperature regions for the magnetoresistance measurements (Figure 7.20 except for the point near T_c. We also note possible changes brought about by the thermal process. While there are observed changes in the zero-field cooling measurements after field heating, they are not monotonic in field, which we could attribute to differences in the temperature and measurement sweep.(Figure 7.21)

7.2 Summary

• Transport measurements with field along the Si[111]/MnSi[111] hard axis for the grown films show good correspondence with observations of the Hall effect for both bulk and MnSi thin films. Symmetrization of the measured signal with respect to the magnetic field is done similar to [Ritz 13a] resulting in a single magnetic field dependence. The hump-like features in the extracted anti-symmetric Hall signal is consistent with results for bulk MnSi in [Ritz 13a] at low applied pressure. However, we cannot fully claim this because of the hysteretic behavior of the magnetoresistance, which introduces some uncertainties into the extracted parameters and the nature of the features in the magnetotransport signal.

Using the formula from [Li 13], we extract the anomalous, topological and ordinary Hall parameters for both the 20 and 12 nm test films grown. For both samples, the values of the ordinary Hall coefficient R_0 for both films are consistent with the values used by [Neub 09a] for calculating the effective topological magnetic field and spin polarization P at the A-phase. However, lower values have been measured at lower temperatures by [Lee 09] and [Neub 09a]. This increase in the value of R_0 may possibly attributed to the strain in the films, even at small induced uniaxial anisotropy, reducing the carrier concetration through a warping of the bandstructure.

• While the extracted values for the thicker layer has a value for the coefficient for intrinsic scattering β that is consistent with the results of [Lee 09], we measure a much higher value for the thinner layer. One possible reason for this is the increasing importance of surface effects in thinner films.[Gerb 02] Another possible explanation would probably be due to the topological nature of the anomalous Hall term itself. An ehanced net chirality in the thinner film might result in a higher anomalous signal.[Tata 02, Tagu 09] This can probably be supported by the higher RRR for the thinner film, which is higher than [Li 13] where they confirmed the crystallinity of their samples with TEM.

• The magnitude of the calculated topological Hall Hall contributions for both films, all done at 4K, fall within the small value $2 - 4$ nΩ·cm, which is in the same order as the values measured by [Li 13] at low temperatures ($\approx$ -7.8 nΩ·cm) and for [Neub 09b] near

T_c. The sign of the topological signal (negative) is consistent with the values observed for $T \leq 5K$ for the 20 nm layer but reversed for the 12 nm film. We might be able to use as as possible explanation for this sign reversal in the dependence of the THE signal on the spin polarization P, which is sensitive to the position of the Fermi level of the material.[Jeon 04][Hort 07] The switching of the sign of the topological Hall signal with the direction of applied field is also consistent with the chiral Skyrmionic nature of the signal as proposed by [Binz 08], which might give credence to the topological nature of the measured THE signal. Unfortunately, no study of the magnetization structures using techniques such as Lorentz TEM has been done yet for these films and at the low temperatures used for the transport measurements, which should be an attractive project for future researchers in addition to further transport studies.

• Minor loop measurements show magnetization dynamics in the thin films. The results for the 20-nm layer are consistent with multiple magnetization processes happening within the material all with time-sensitive relaxation processes, like the possible existence of domains of different chirality in the sample. Further measurements should be done to identify the exact time-dependent magnetization processes happening within the grown films in this work.

• Hump-like features in the Hall voltage are seen in the region of 10 K and 40K (near the T_c) in temperature-dependent measurements. These bounding features are prominent in measurements. The values of the bounding temperatures are consistent with the range where Skyrmions are observed in thin plates and expitaxially-grown thin layers of MnSi. [Tono 12, Li 13] Further measurements of these samples within this temperature range would most likely yield a more complete picture of the magnetization processes in the material.

Chapter 8

Magnetotransport with In-Plane Applied Fields

In the previous chapter, magnetotransport with applied fields along the magnetic hard axis was discussed. It was shown that of the Hall measurements show the possible magnetotransport signature of the chiral (Berry-phase) contributions to the anomalous Hall effect. In this chapter, we discuss important results from our magnetotransport measurements on MBE-grown thin film MnSi at small in-plane fields at various angles. Most transport studies that have been done on thin MnSi so far have been on specific crystalline directions. In this chapter, we explore the evolution of the magnetic behavior with respect to multiple magnetization directions, particularly at low fields which would give the most information regarding relaxation processes in the magnetic structures and the ground state present in the material.

8.1 Magnetotransport Measurements in MnSi epitaxial thin films

Two main categories of measurements were done on the samples at an applied low field along the sample plane. First is measuring the anisotropy of the magnetic response to field direction at constant magnetic field. The second is applying a varying magnetic field along a particular angle. For these low-field measurements, we use an XYZ vector magnet with three-dimensional field rotation (for variable angle measurements) and performed electrical measurements of the magnetic response at low temperatures (4K He cryostat) using standard lock-in techniques.

8.1.1 Saturation Magnetization Measurements

For saturation magnetization measurements, a 300mT saturation field is applied along different direction along the crystal plane. The magnetic behavior is measured using

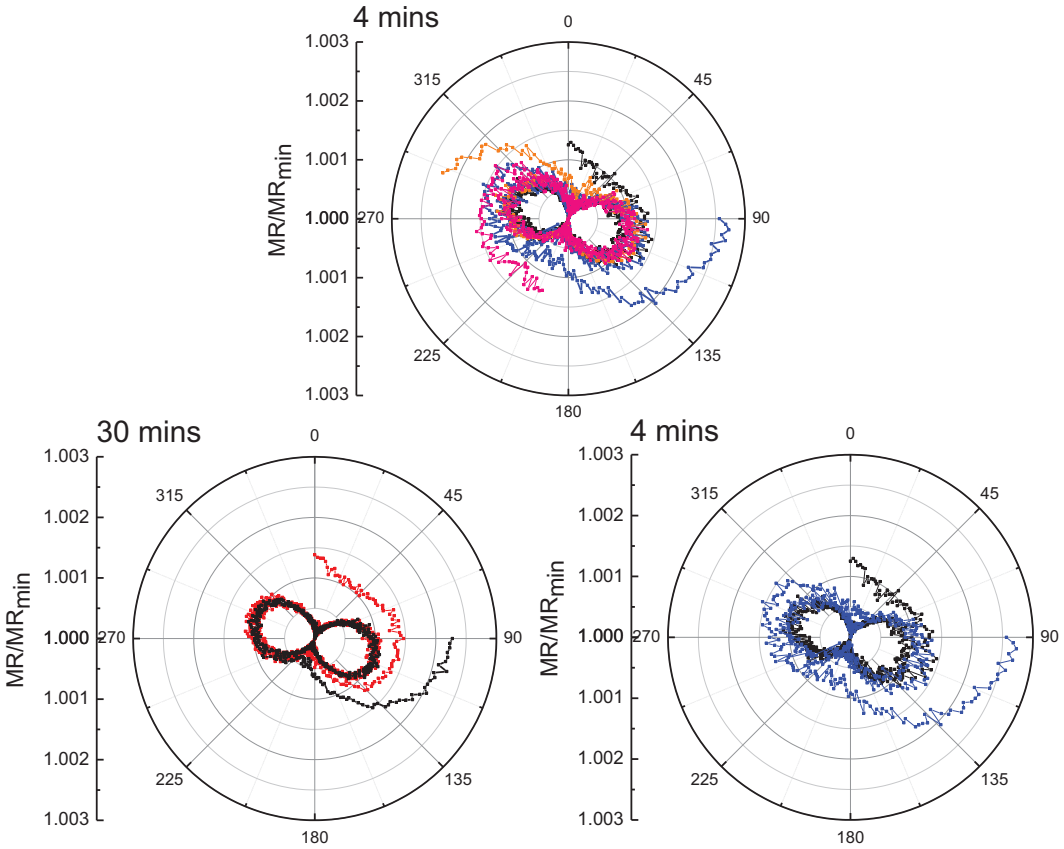

Fig. 8.1: Saturation magnetization measurements on the 20-nm grown MnSi thin film at different starting field angles. A memory ("glass-like") behavior is observed even with increased saturation waiting times at the order of the observed relaxation time. The current along the hallbar is along MnSi[1$\bar{1}$0], but similar behavior is observed in a Hall bar in the same sample oriented along [2$\bar{1}$3] (B(0°) ||MnSi[2$\bar{1}$3])

a four-terminal longitudinal magnetoresistance configuration. The magnetoresistance is again given by:

$$\rho_{AMR}^{xx} = \rho_{\perp} - (\rho_{\perp} - \rho_{\parallel}) \cdot cos^2\vartheta \tag{8.1}$$

where $\rho_{\perp}$ and $\rho_{\parallel}$ are the resistivities with the current parallel and perpendicular to the magnetization M, respectively. The angle ϑ corresponds to the angle between the current with respect to M. For magnetic 3d transition metals the usual relation between resistivities is $\rho_{\perp} \leq \rho_{\parallel}$.[Baxt 02] We see that this is not the case for the layers. This might be due to the applied field being not enough to saturate the sample into a single domain. We note that the 300mT saturation field is well below the calculated saturation field H_h (transition between helicoidal and isolated domains) for both samples (H_h [20 nm] = 508 mT and H_h [20 nm] = 458 mT) This means that to picture transport from

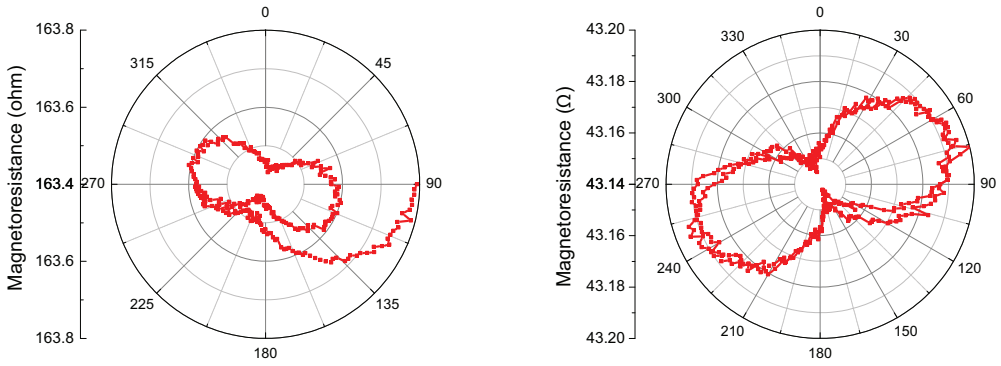

Fig. 8.2: Saturation magnetization measurements for 20 and 12-nm thick MnSi home-grown films. The measurement for the 20-nm film shows a glassy/memory effect while the 12-nm film shows no sign of the same effect. The current for the 20 nm layer is along MnSi[$1\bar{1}0$] (B(0°) ‖MnSi[$2\bar{1}3$]) and for the 12 nm layer along MnSi[$01\bar{1}$] (B(0°) ‖MnSi[$01\bar{1}$])

the possible magnetization configurations within the material, we can consider only the evolution of distorted helicoids. These distortions come from the effects of the strain in the material.[Plum 82] These notes are applicable as well to the subsequent measurements.

Measurements on the 20-nm layer show memory or glass-like behavior in the saturation magnetization measurements shown in Figure 8.1. The applied current for the measurement shown is along MnSi[$1\bar{1}0$]. Similar memory behavior is observed for the Hall bar oriented along [$2\bar{1}3$] and is also shown to appear for random angles of the magnetic field after initial saturation, which means that this effect is not a product of the strain-induced in-plane crystalline anisotropy. In contrast, this is not observed for the 12-nm layer. (Figure 8.2)

The memory effect observed for the 20-nm layer does not vanish even when increasing the waiting time of the saturation and also changing the angle between the applied current and the magnetic field. This delay in the magnetization saturation did not disappear even at a saturation waiting time of 30 minutes. Considering that one full rotation in the order of 30 minutes and that the magnetoresistance settles into the equilibrium well within full rotation of the magnetic field, this rules out the possibility that a longer saturation time at 300mT will work to remove this lag in the relaxation. However, we can see in Figure 8.1 that the increase in saturation waiting time seems to improve measurement noise. This can possibly be explained from increased saturation of different magnetic processes at different time scales within the material. However, further measurements are needed to check the sample with a wider range of applied fields and saturation times to confirm this. In-plane SQUID measurements, for example, shows full saturation at 1T, much higher than the field used here.

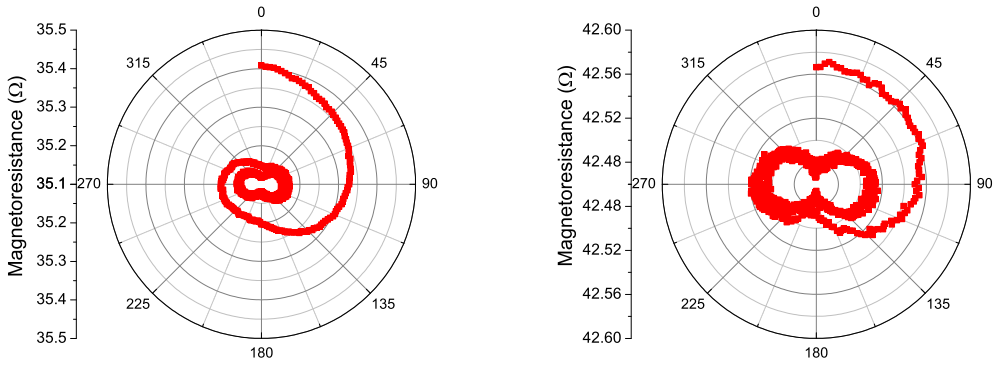

Fig. 8.3: Saturation magnetization measurements for 17.1 (left) and 17.9 (right) nm-nm thick MnSi home-grown films, presented here as points of comparison for the 20-nm measurement. Both samples are grown with c-Si caps, post-annealing after growth. Both measurements also show the glass-like memory effect. The current for both films are along MnSi[$\bar{2}$11] (B(0°) ||MnSi[01$\bar{1}$]).

For further comparison, we also performed the saturation magnetic measurements on two other samples grown with c-Si cap layers.(17.1 nm and 17.9 nm) For crystalline growth, the cap is grown at the same temperature as the MnSi film growth, in contrast with room temperature a-Si cap growth. The measurements for both samples are shown Figure 8.3. It can be seen that both samples show the glass-like behavior similar to the 20-nm layer. A possible explanation would be the formation of Mn complexes, such as local clusters with anti-ferromagnetic interactions, during cap layer annealing. Antiferromagnetic domains could cancel Mn moments leading to a magnetically frozen state.[Zeng 08] We note that the formation of elliptical islands with long axis oriented along MnSi[$\bar{1}$10] was also observed in one of these c-Si capped samples using AFM.[Pohl 13] This lends some credence to the possibility of existence of both chiral domain types existing in the 20-nm layer.

For their SPE samples, [Karh 10] explained glassy behavior in their grown films to be due to the presence of both chiral domain types in the thin film. The memory effect is not observed in the 12-nm layer, which could mean the existence of a single or at least dominant chiral type within the material. The magnetic chirality in MnSi is dependent on the handedness of the unit crystal.[Grig 09, Tana 85] With RRR comparable to crystalline 10 nm samples grown by [Li 13], there is a possibility of high crystalline quality in the 12-nm layer resulting in a single chiral type within the material. This could support the explanation that the observed memory relaxation effect in the saturation magnetization measurements arises from the existence of a net chirality. A net magnetic torque due to the unpinned domain walls may also arise.[Heur 03] The eventual relaxation of the magnetoresistance could be due to the domain walls in the system reaching equi-

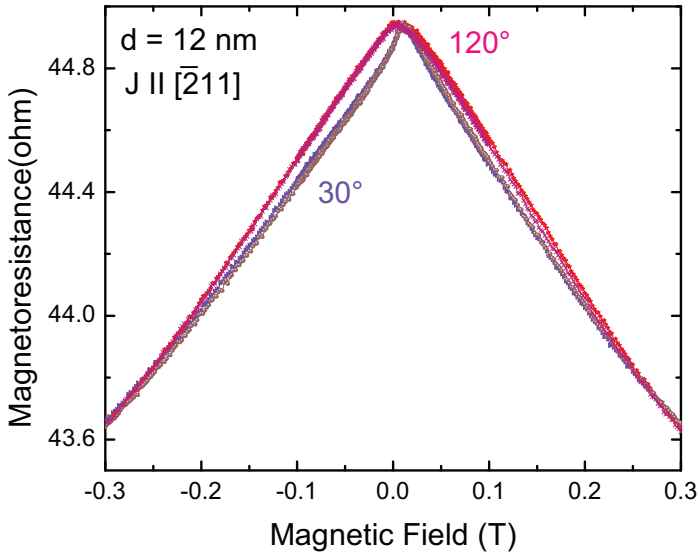

Fig. 8.4: Low field MR curves (saturation at B = -300mT) at 30° and 120°. Current through the hallbar and the 0° field direction is along MnSi[01$\bar{1}$]. We see a linear magnetic field dependence $\propto H^1$, consistent with [Mori 85]'s description of weak itinerant ferromagnets at small fields. This is as well consistent with MR measurements on single-crystal MnSi nanowires.

librium. Methods such as transmission electron microscopy (TEM) measuring the ratio between left-handed and right-handed crystal structures for both samples might confirm the proposed explanation of the existence of this glass-like effect.

8.1.2 Longitudinal Magnetoresistance Measurements

In order to gain more understanding on the field dependence of the magnetic properties of the grown thin films, the magnetoresistance of each layer was measured. For longitudinal magnetoresistance measurements, the variable magnetic field was applied in-plane at different angles. The magnetoresistance measurements at some angles are shown in Figures 8.4 (12 nm) and 8.5 (20 nm).

Both samples show strong negative magnetoresistance, consistent with the high magnetoresistance measured for the field parallel to MnSi[111]. For This large magnetic response can be attributed to the suppression of the spin fluctuations and increased magnetic ordering at an applied field in the material, similar to what is happening with magnetoresistance measurements with an out-of-plane (MnSi[111]) applied field.[Li 07, Lin 10] The measured in-plane magnetoresistance has a value of 0.9 % at an applied field of 300mT for the 20 nm layer and 2.75 % for 12 nm layer. Following the theory of itinerant ferromagnetism at low fields, the magnetic field dependence of both samples can be differentiated as weakly

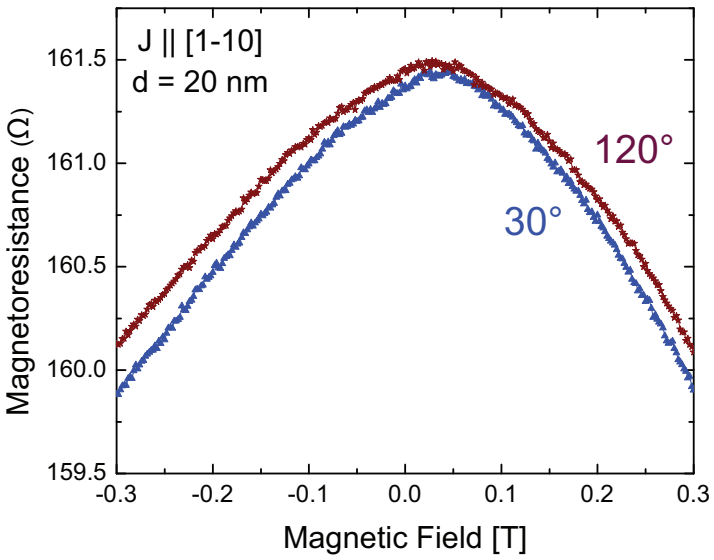

Fig. 8.5: Low field MR curves (saturation at B = -300mT) at 30° and 120°. Magnetic field direction 0deg along MnSi[$2\bar{1}3$]. Current through the hallbar and the 0° field direction is along MnSi[$1\bar{1}0$]. We see a square magnetic field dependence $\propto H^2$, consistent with [Mori 85]'s description of nearly ferromagnetic metals at small fields.

ferromagnetic (12 nm, $\propto H^1$) and nearly ferromagnetic (20 nm, $\propto H^2$).[Mori 85] Bulk MnSi is categorized as a weak itinerant ferromagnet, which could support the possibility of the existence of bulk-like single helical state in the 12-nm layer.

Again for further comparison, we show representative magnetoresistance curves for the c-Si cap samples (Figure 8.6) Both samples show, in contrast to the other two samples, very low positive magnetoresistance. This is actually consistent with the behavior of a non-magnetic disordered electronic system (e.g. amorphous Mn_xSi_{1-x}).[Lee 85] The low magnetoresistance might arise from the quenched Mn moment due to disorder. [Zeng 08] suggests an Anderson localization model wherein localized itinerant states with no moment exist within disorder-induced impurity bands. However, this is after discounting for their samples the existence of Mn-rich regions within the sample forming antiferromagnetic clusters. Because of higher doping, these regions are more likely to exist in our samples compared to their low-doped Si:Mn samples. (our MnSi samples x ≈0.5 compared to their samples x ≈ 0.07 –0.22) The spin glass-like behavior of the material is also consistent with antiferromagnetic interactions within our sample.

In order to observe the magnetic behavior of the spin structures in the grown films, we use the polar plot method described in [Papp 07a] to visualize their evolution with variable field. The polar plots for the 12 and 20 nm layers are shown in Figure 8.7.

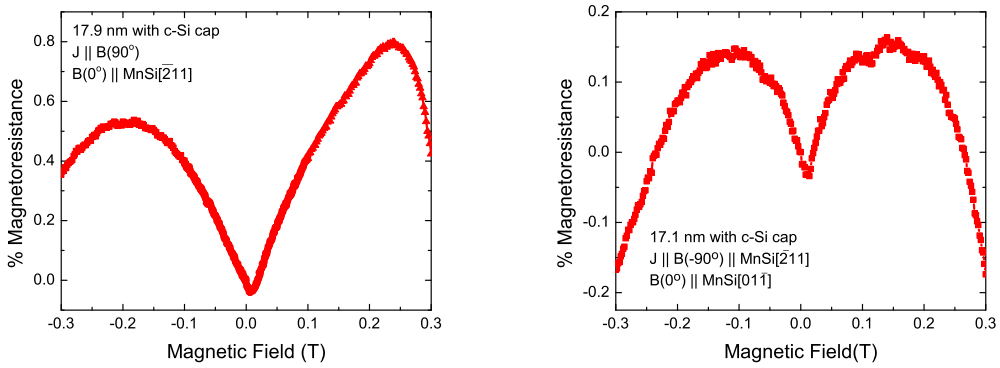

Fig. 8.6: Longitudinal magnetoresistance measurements for 17.1 and 17.9nm-nm thick MnSi home-grown films, presented here as points of comparison for the 20-nm measurement. The percent change in magnetoresistance is calculated from the zero-field resistance value and both samples show very low magnetoresistance which is positive at very low fields. The current for both films are along MnSi[$\bar{2}$11] (B(0°) ‖MnSi[01$\bar{1}$]).

From the magnetoresistance polar plots of both layers, it is pretty difficult to conclude the strength of the uniaxial anisotropy with the lack of sharp magnetization switches for materials such as (Ga,Mn)As. We might attribute this to the demagnetization corrections from the shape anisotropy of the Hall bar.[Ahar 98] Indeed, sample shape has been studied and observed to reduce and shift the transition fields. [Baue 12]

Also as a test for the possibility of in-plane transport contributions of an out-of-plane field, magnetic fields of 0 to 200 mT was applied along MnSi[111] while varying the in-plane magnetic field. The plots are shown in Figure 8.8. For helical magnets, an applied in-plane field distorts the helix into a helicoidal structure until the magnetization structure breaks into isolated domains at saturation.[Karh 12] For our measurements, we do not reach this critical value H_D in our applied fields. For an out-of-plane field, the helical structure is pulled into a conical state until the applied field is high enough to reach an induced ferromagnetic state. From measurements done on MnSi thin films, the helical-conical transition magnetic field is estimated to be around 180 mT for fields applied along MnSi[111].[Karh 11] Below a certain field, the helical structure re-orients to the easy axis.[Plum 81]

Comparing the polar plots for the 0 mT and 200mT applied fields, it seems that there is a change in the low-field fluctuations at an out-of-plane applied field near 200 mT. (Figure 8.8) However, as with Figure 8.7, this difference could possibly just arise from the demagnetization effects. This is supported by the plots with other out-of-plane magnetic field strengths where the observed evolution of the magnetic properties appear to be random

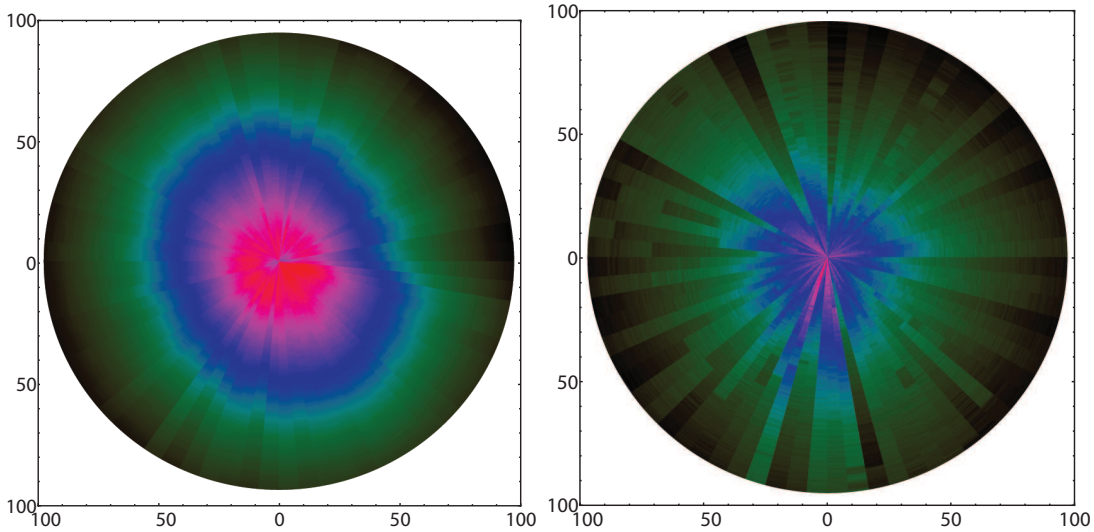

Fig. 8.7: Polar plots for the 12 and 20 nm thick films. The current along the 12 nm film is along [01$\bar{1}$] (B(0°) ||MnSi[01$\bar{1}$]) and along [1$\bar{1}$0] for the 20-nm film.(B(0°) ||MnSi[2$\bar{1}$3])

as well.

Linear in-plane magnetoresistance behavior for small fields is measured for the 12nm layer, pegging it as a weak itinerant ferromagnet. The latter is consistent with observations for high purity MnSi bulk [Mori 76, Mori 85]. This also echoes the qualitative bulk-like properties observed for films of almost similar thickness studied by [Enge 12]. The out-of-plane SQUID measurement for the 12-nm MnSi film even shows a transition field of $\approx$ 100mT for the magnetization. However, the out-of-plane field does not seem to show significant effect on the in-plane longitudinal magnetoresistance measurements for this sample, particularly a transition around 50 - 100mT field along MnSi[111] as the material is expected to transition from the helical to the conical phase from the SQUID measurement. (or $\approx$ 180mT for the Skyrmion lattice formation [Tono 12]) As pointed out earlier, we can possibly attribute this smearing of effects of the growth-induced uniaxial anisotropy to magnetotransport properties to the device shape/geometry.[Baue 12] Further measurements, possibly using the planar Hall effect instead (i.e. the signal arising from the magnetization direction), higher fields, different device geometries, and theoretical considerations may be needed to bypass this limitation and pinpoint the exact nature of the magnetization behavior.

8.1.3 Planar Hall Effect Measurements

The PHE measurements were performed using the the set-up as the longitudinal measurements, but measuring the transverse voltage drop. The planar Hall effect (PHE)

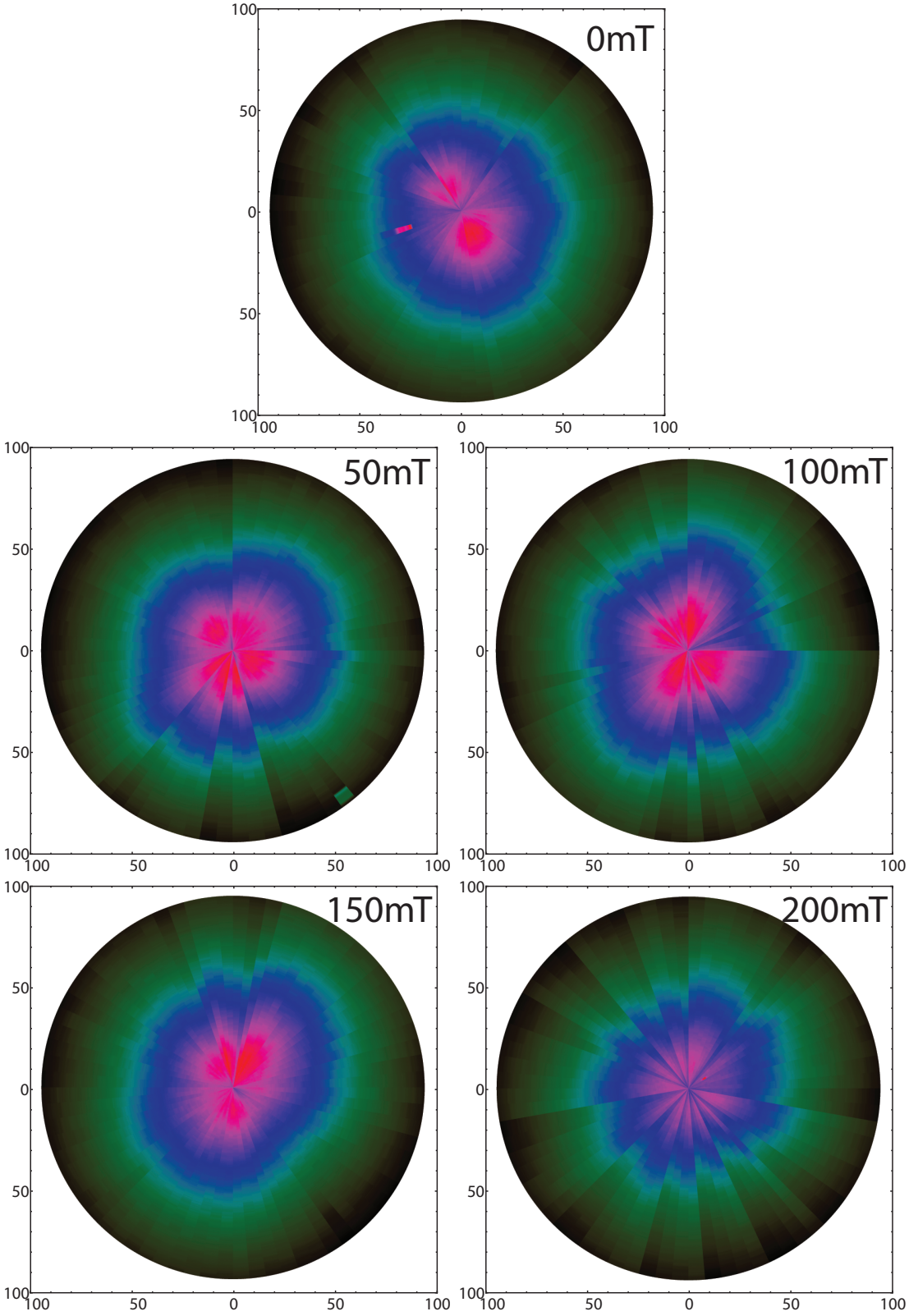

Fig. 8.8: Variable magnetic field measurements at different field strength applied along MnSi[111] (0 to 200 mT) with in-plane saturation magnetization 250mT (200mT for the 200mT measurement due to limitations in the XYZ vector magnet). Current is along MnSi[$\bar{2}11$] and the 0° direction for the magnetic field is along MnSi[$01\bar{1}$].

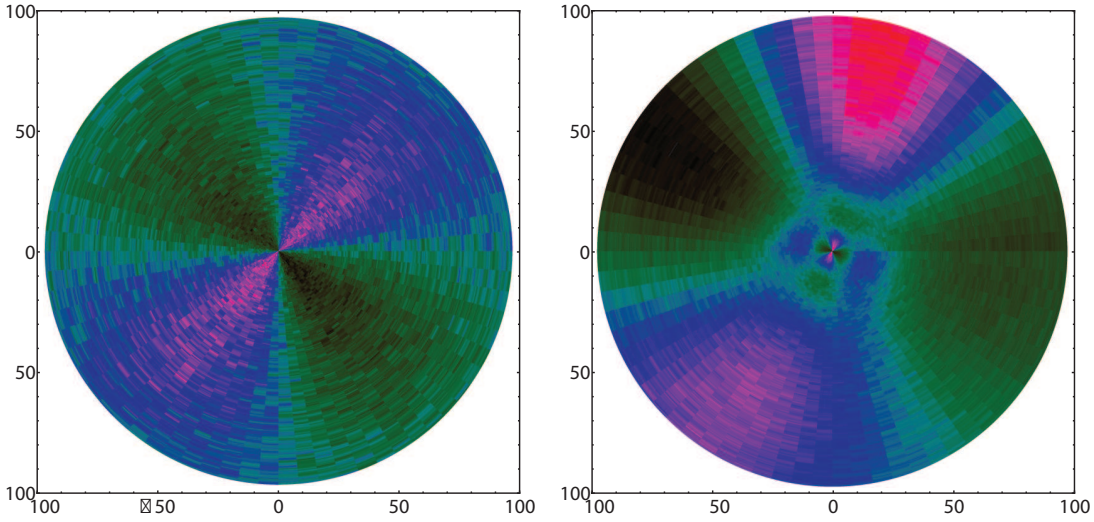

Fig. 8.9: Polar plots for the PHE curves from the 20 and 12 nm thick layers. Saturation field is at -300mT, way below H_h. The current for the 20-nm measurement and the magnetic field 0-degree direction are both along $[2\bar{1}3]$. For the 12 nm layer, the current and magnetic field 0-degree direction are both along $[01\bar{1}]$. Unlike the smooth rotation of the magnetization for the thicker layer, the 12-nm measurement shows sharp jumps to the easy axis.

measurement in metals follows the relation [Hurd 72]:

$$\rho_{PHE}^{xy} = -\frac{\rho_{\perp} - \rho_{\parallel}}{2} \cdot sin(2\vartheta) \tag{8.2}$$

where $\rho_{\perp}$ and $\rho_{\perp}$ are the resistivities with the current parallel and perpendicular to the magnetization M, respectively. The angle ϑ corresponds to the angle between the current with respect to M. Polar plots showing the evolution of the magnetization for both films are shown in Figure 8.9.

Both polar plots show uniaxial anisotropy present in both films. However, there is a contrast between the sharpness of the switching events for the two films as the magnetization relaxes to the easy axis. This can be easily seen in the individual curves for both samples shown in Figure 8.10.

The smooth rotation of the magnetization to the easy axis for the 20-nm layer is reminiscent of magnetization relaxation in a material with multiple domains. This could support both the possible existence of both chiral domain types in the thicker layer, while a single dominant chirality present in the 12-nm layer. Since the chirality is closely tied to the handedness of the crystal structure present in the material, this observation can also support the possibility of a single crystalline structure in the 12 nm layer.[Tana 85] Of course, this could also be due to the stronger uniaxial anisotropy present in the thinner layer.

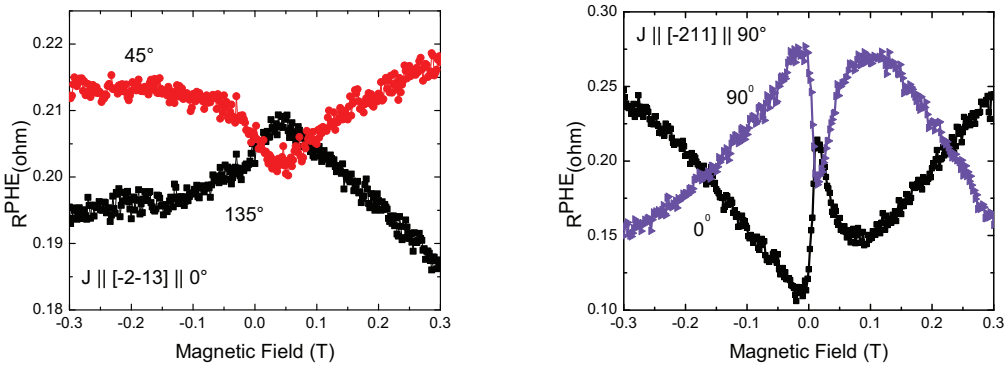

Fig. 8.10: Planar hall effect curves for the 20 and 12 nm thick films at various angles. The 20-nm shows smooth rotation of the magnetization to the easy axis, in contrast to the sharp jump in the 12-nm measurements. MnSi crystal directions are noted.

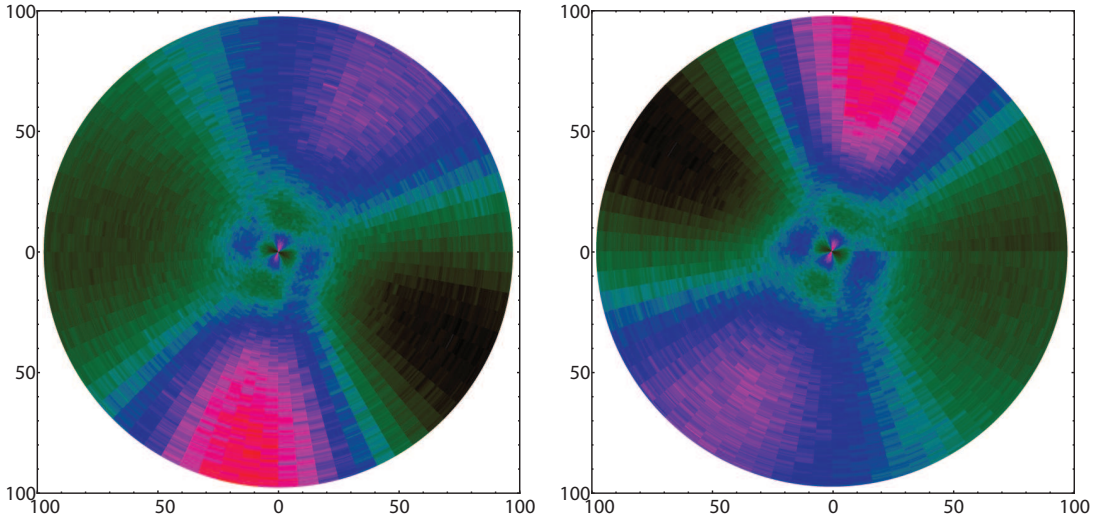

Fig. 8.11: Polar plots for the 12-nm layer with current applied at different directions. The current direction in the resistance polar plot on the left is along [$\bar{2}$11], while the plot on the right has the current along [01-1].

Now, changing the direction of the current by 90° completely flips the signal by 180°, which is consistent with the symmetry of Equation 8.2. Polar plots at different directions of the current for the 12-nm thick layer are shown in Figure 8.11. The switch to the easy axis at low fields can clearly be seen around the region of $\approx$ 20 mT.

As the PHE is tied to the magnetoresistance, normal PHE in metals is symmetric with with field according to the Onsager relations.[Onsa 31a, Onsa 31b] However, features asymmetric with applied field are observed in the signal.(Figures 8.12 and 8.13, curves shifted for clarity) The asymmetry is small in the 20 nm layer and more evident in the

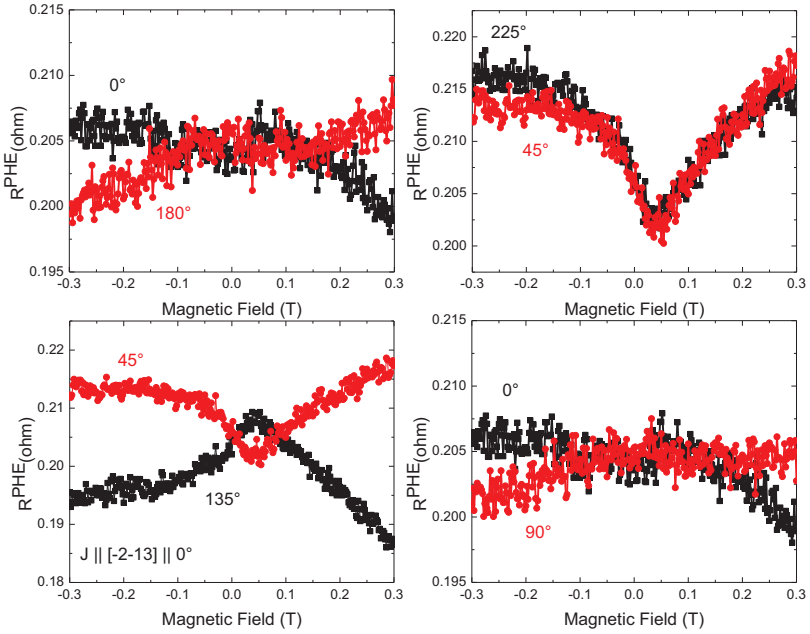

Fig. 8.12: Raw PHE curves for the 20-nm grown film with current and 0 degree magnetic field direction along MnSi[$2\bar{1}3$] at various angles (0 to 180 degrees).

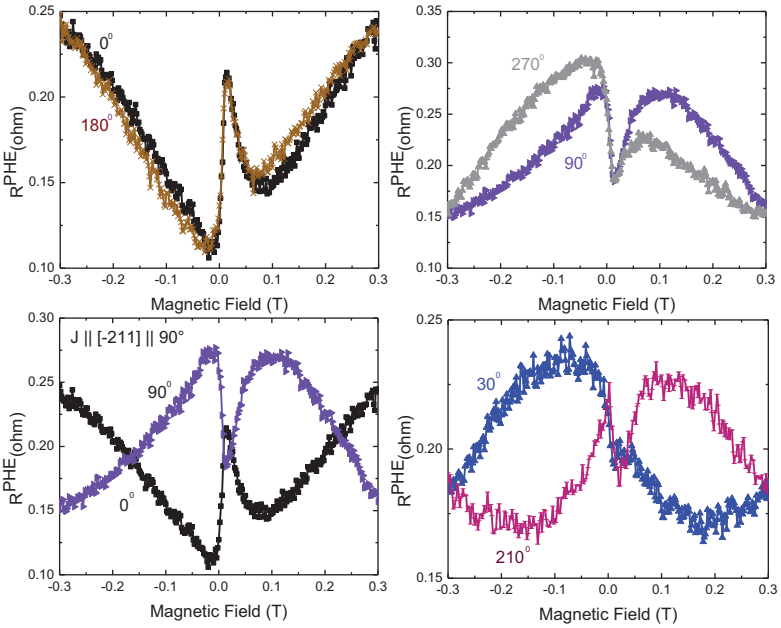

Fig. 8.13: Raw PHE curves for the 12-nm grown film with current along MnSi[$\bar{2}11$] and 0 degree magnetic field direction along MnSi[$01\bar{1}$] at various angles (0 to 180 degrees).

PHE curves of the 12 nm layer.

For further analysis, the antisymmetric part of the PHE signals are extracted. As always, the signals are symmetrized carefully to avoid creating hysteresis which can be miscon-

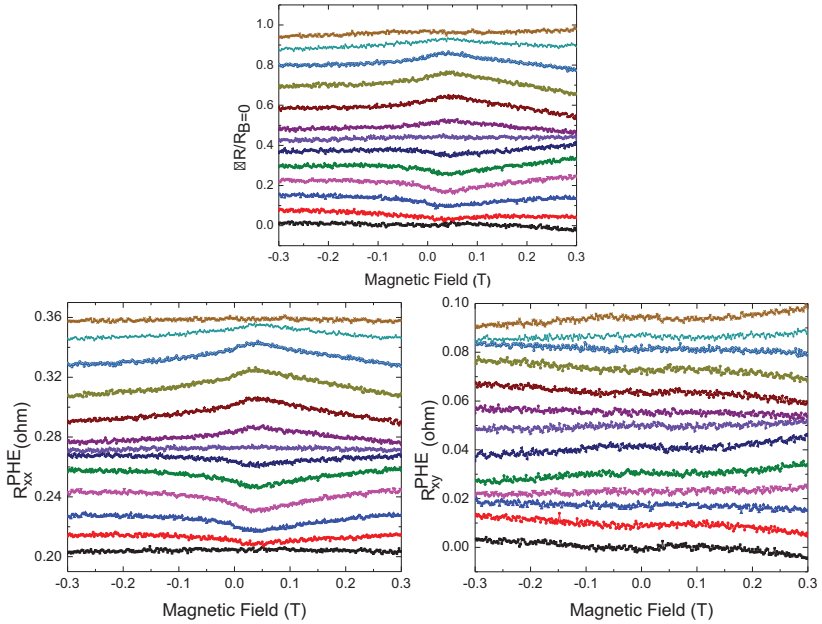

Fig. 8.14: PHE curves for the 20-nm grown film with current and 0 degree magnetic field direction along MnSi[2$\bar{1}$3] at various angles (0 to 180 degrees, 15 degree steps), including the antisymmetric and symmetric parts of the signals. The curves are shifted for clarity.

strued as real signature from the spin structure in the material. The results are shown in Figures 8.14 (antisymmetric component enlarged in Figure 8.15) and 8.16. For the symmetrized results, R_{xx} denotes the symmetric component and R_{xy} the antisymmetric component.

There is a marked difference between the extracted antisymmetric signals of the two grown films, with the component larger in the thinner layer. As for the source of this antisymmetric term, we have a few possibilities. Lithographic imperfections may introduce an asymmetry in the measured signals. Asymmetric contacts were used by groups to determine vortex chirality from the planar Hall effect, wherein the shift in the switching fields and asymmetry of the saturation signal were used to determine the handedness of a vortex.[Huan 06] Further fabrication of asymmetric devices might be useful in determining the contribution of lithographic errors in the antisymmetric component of the PHE signals.

A second explanation relies on the asymmetry of the crystalline structure of the material. The studies of [Mudu 05] on these systems propose the antisymmetric part arising from the antisymmetric part of the magnetoresistivity tensor. The antisymmetric part of the PHE signal in Fe and Fe_3Si films grown on GaAs(113)A substrates have also been explained by the contribution of the anomalous Hall effect through the chirality of the crystal structure.[Frie 06] If true for the grown films, the latter could explain the difference

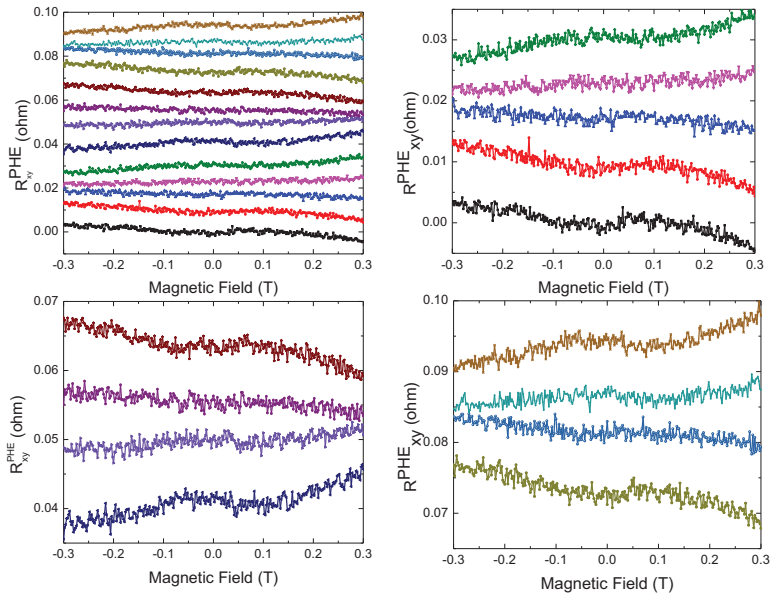

Fig. 8.15: Antisymmetric part of the PHE signal for the 20-nm layer. Current direction is along [$2\bar{1}3$]. Curves are from 0 to 180 degrees with 15 degree steps.

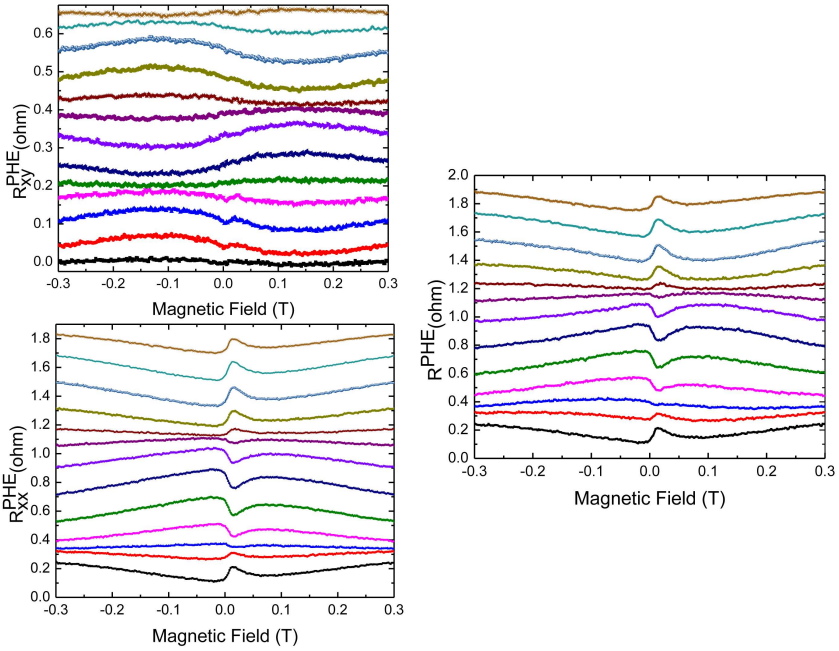

Fig. 8.16: PHE curves for the 12-nm grown film with current along MnSi[$\bar{2}11$] and 0 degree magnetic field direction along MnSi[01-1] at various angles (0 to 180 degrees, 15 degree steps), including the antisymmetric and symmetric parts of the signals. The curves are shifted for clarity.

between the size of the antisymmetric signal for both samples, if we combine with previous observations that the distribution of chiral domains in the grown films are different.

8.2 Summary

Low magnetic field characterization proves to be a good tool in probing the magnetization behavior and unraveling key difference between the grown films. For future measurements of the properties of MBE-grown MnSi thin films, variable angle low field measurements may be as important as high field in-plane and out-of-plane measurements in determining the effects of net chirality, the induced in-plane uniaxial strain [Karh 10] or spin-spin interactions [Enge 12] in the properties of these materials at the ground state. We point out the following key points in this work:

• The constant-field magnetoresistance for the 20-nm film shows are memory or relaxation effect which does not appear in the 12-nm film. From [Karh 10], they attribute glassy behavior of grown films through disorder and the presence of both chiral domain types in the sample. This is consistent with the higher RRR measured for the thinner film (comparable with [Li 13], indicating crystalline quality)

• The magnetoresistance further explores the difference in the ratio of the existence of both chiral domain in the grown samples. The 20-nm layer shows parabolic field ($\propto H^2$) dependence, consistent with a nearly ferromagnetic state, which is could possibly be explained with presence of both ferromagnetic and anti-ferromagnetic domains in the sample. The 12-nm film's low field linear ($\propto H$) magnetoresistance also shows weak ferromagnetic behavior, which could suggest single chiral type in the thin film.[Mori 85]

Longitudinal magnetoresistance curves were used to determine the effects of the measured in-plane anisotropy from SQUID magnetization measurements. However, polar-plots show no sharp switching between easy and hard axis directions for both the 20 and 12-nm layers. This probably arises from demagnetization effects caused by the shape anisotropy of the Hall bar.[Ahar 98, Baue 12]

• The planar Hall effect or PHE, on the other hand, proves itself as a useful tool in determining the magnetization easy axis of the crystal. The magnetization switching shows the relative difference between the uniaxial anisotropy strengths between the two samples. For the 20-nm layer, the magnetization rotates slowly to the easy axis at a maxima of 40 mT, while the 12-nm layer shows a sharp switch at $\approx$ 20 mT. More importantly, this can also be a measure of the existence of both chiral domain types within the material.

• Symmetrization shows both a symmetric and antisymmetric part of the PHE signal. PHE, by definition in metals, should be symmetric with field through its dependence on the magnetoresistance. A plausible reason that may possibly explain the effect is an Umkehr effect (second order Hall term) arising from induced crystalline anisotropy due to strain during the growth of MnSi[111] on Si[111].[Mudu 05] Non-coplanar spins configura-

tions and the induced crystalline anisotropy from the growth couples the anomalous Hall effect and the planar Hall effect.[Frie 06] Aside from investigations in the spin structures present in the material, further investigations on the uniformity of the grown layers are needed to confirm this as a possible explanation of the asymmetric signal.

Chapter 9

Conclusions & Outlook

In this thesis, we reported the magnetotransport properties of epitaxially-grown MnSi thin films and ultra-thin (Ga,Mn)As layers. The ultra-thin (Ga,Mn)As films show increased uniaxial contributions in magnetoresistance measurements, which is consistent with transport properties of samples near the hopping regime and in the vicinity of the metal-insulator transition. Here we show that the electric field manipulates the magnetic anisotropies of the material, such as a monotonic change in the uniaxial contributions for the large structures, also showing decreasing asymmetry between the uniaxial hard axes. The fluctuations however are also shown to become prominent and finally affect the magnetic behavior of the material for smaller structures. The magnetoresistance (in-plane and out-of-plane) measurements show non-monotonic changes in the uniaxial contributions to the anisotropy for the small structures, compared to the linear resistance increase with applied voltage in the large structures. Further studies should be done to study the nature of these fluctuations.

As a side study, epitaxial lift-off was used to test the compatibility of different gate barriers, in our study the paraelectric Strontium Titanate (STO), with(Ga,Mn)As. We observe changes in the magnetic anisotropies and magnetotransport for lifted-off layers, but the process used to transfer the free-standing film preserved the magnetic anisotropies of the 70 nm films used in the fabrication process. Unfortunately, the STO/Si interface appears to have near-zero conduction band discontinuity. Future work should focus on using different combinations of substrates with the STO to finally make use of the large dielectric constant of the material. Further testing and optimization should also be done on other parts of the process such as the lift-off, film growth and device fabrication.

For future work in (Ga,Mn)As layers, particularly parabolic-doped ultra-thin films, improvements in the leakage current through the gating barrier would be of importance to further drive the material through the insulating state and observe the changes in the magnetic behavior. The epitaxial lift-off technique could be a very important tool for future work, as it opens the possibility of working with other substrates with higher di-

electric constants and improved low-temperature behavior.

We also observe interesting magnetotransport effects for our MBE-grown MnSi thin films. The magnetic measurements for the grown films show good qualitative correspondence with observations for both bulk and MnSi thin films grown for this study. The high field extracted Hall parameters and topological Hall signals were shown to be consistent to results from bulk. However, differences are also appear such as the thinner layer showing reversed topological Hall sign and larger anomalous Hall contribution, possibly explained by the increasing importance of surface effects in thinner films, changes in the bandstructure and the topological nature of the anomalous Hall term arising from an enhanced net chirality. Minor loop measurements show possibility of with multiple magnetization processes happening within the material and temperature measurements also show hump-like features in the Hall voltage that can possibly be from the magnetic structures present in the material.

Low in-plane magnetic field characterization techniques were also shown to be good tools in probing the magnetization behavior of MnSi thin films. The constant-field magnetoresistance for MnSi film shows memory or relaxation effect, which could be possibly attributed to disorder and the presence of both chiral domain types in the sample. The longitudinal magnetoresistance of the grown films are also shown to follow characteristic applied field behavior at low fields. An obsrved asymmetric component of the planar Hall effect or PHE for both films possibly arises from second order Hall term due to non-coplanar spins configurations and the induced crystalline anisotropy from the growth couples the anomalous Hall effect and the planar Hall effect.

These results for the MnSi thin films show the potential of the material for fundamental studies in complex magnetic structures and possible applications. However, as with the (Ga,Mn)As films, further measurements should be done to identify the exact magnetization processes happening within the grown films in this work. Unfortunately, for MnSi thin films, no study of the magnetization structures using techniques such as Lorentz TEM has been done yet for these films at the low temperatures used for the transport measurements. This should be an attractive project for future researchers in addition to further transport studies.

Appendix A

Fabrication of Four-Terminal Corbino Gated Structure

In this appendix, steps of the device fabrication process used in making the four-terminal Corbino structures used for this work are detailed. As mentioned on Chapter 3, the Corbino geometry is employed to observe the electric field effects on the crystalline anisotropy of ultra-thin parabolic (Ga,Mn)As layers near the metal-insulator transition.

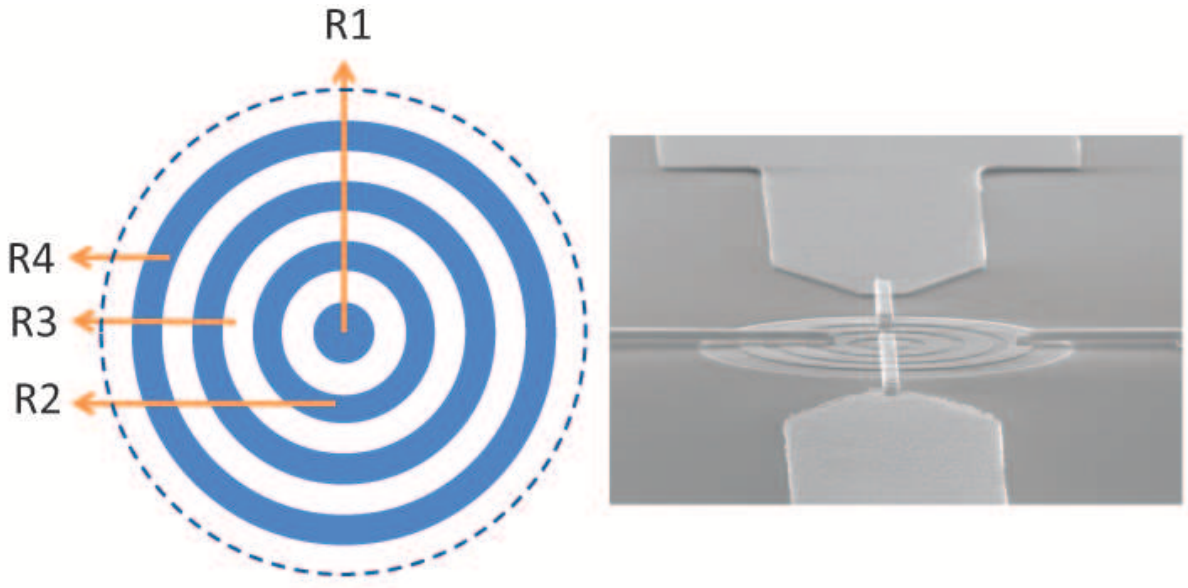

Fig. A.1: Corbino structure with the rings labeled R1 - R4. The four-contact configuration eliminates the effects of the contact resistance and allows for lower measured resistances. A finished e-beam structure is shown on the right.

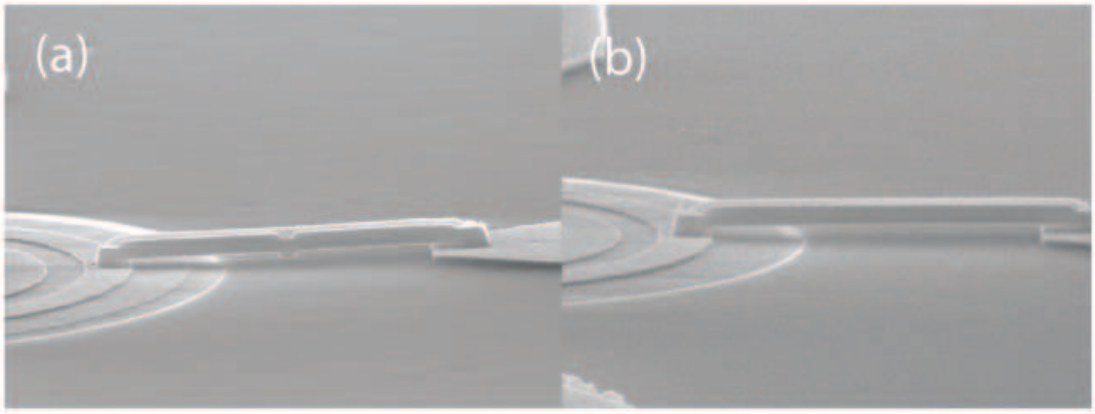

Fig. A.2: Bridge structures used for the Corbino sturctures. Because of the length of bridges used, bridges with supporting posts (a) made of cross-linked PMMA (insulating) was used. However for some structures, bridges (Figure A.2.b.) are stable enough without needing the extra posts.

A.1 Fabrication Details

The Corbino structure and four-terminal configuration was used for canceling spurious effects coming from contact resistance. Because of the latter, the conductance fluctuations can be attributed to scattering and localization processes within the material. The disadvantage of this structure is that the Hall effect is shorted and cannot be measured in this geometry. The design of the main four-terminal device is shown in Figure A.1

The device is composed of four rings, where the current is applied in rings R1 and R4 with the voltage drop measured along rings R2 and R3, following the normal four-terminal measurement configuration. These rings are 1μm in width, which necessitate the need of a suspended metallic connection from the rings to bigger bond pads while avoiding the conducting substrate. The bridge step refers to the technique by [Borz 05]. The cross-linked PMMA step was included to ensure that the structures (long bridges) do not short to the conducting substrate, but has been proven unnecessary because of the stability of the bridge structures.

The gradient of dose factors are to correct for the proximity effect. Lower dose causes left-over resist to form clumps under the contacts and increase contact resistances. (Figure A.1) Another effect of incorrect dose calibration is difficulties in lifting off the metal in between rings without using an ultra-sonic bath. Because of the closed smooth (no corners) structure, lifting off metal from this structure is very challenging. A good calibration of the e-beam dosage would result in a resist profile where the metal can easily

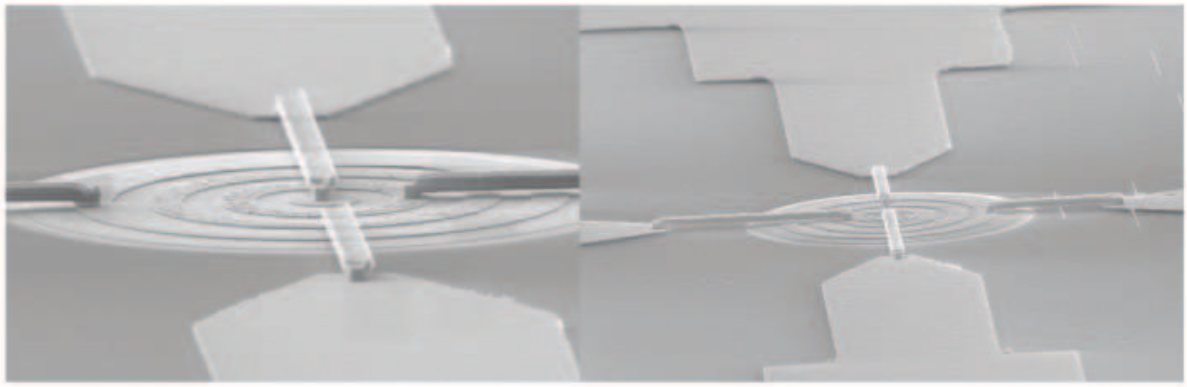

Fig. A.3: Typical errors encountered while making the device. On the right shows underexposed rings. The left-over resist form clumps on top of the rings, increasing the contact resistance dramatically. On the right shows leftover metal trapped between rings.

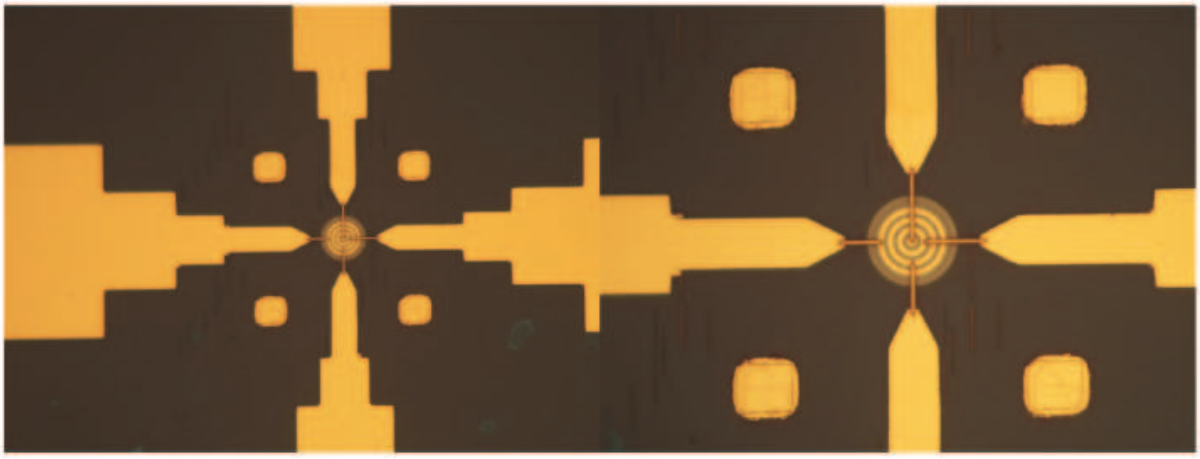

Fig. A.4: Optical images of final four-terminal Corbino device.

be lifted off. (Figure A.3)

After all fabrication processes, the final devices are bonded via soft-bonding or wedge bonding, depending in the adhesion of the gold bond pads on the isolating oxide. A finished device is shown in Figure A.4.

A.2 Optimized final process

Notes:
Baking is always done on hotplate.
Water is always DI-water with resistance higher than $18M\Omega$cm.

IPA = isopropanol
NEP = N-ethyl-2-pyrrolidon
MIBK = methyl isobutyl ketone (AR 600.56: MIBK:IPA = 2:3)
WF = write field
WD = working distance
Evap = Metallization

Processing steps	
Cleaning	30min acetone 50°C, IPA, water
Ring Structure	600K 4% 5000 rpm for 40s, 5 mins at 130°C 950K 3% 6500 rpm 40s, 5 mins at 120°C Expose ring structure and global and local alignment marks 30 kV, WD = 10 mm, aperture 10 μm, WF: 81.92 μm Step size: 4px (870x magnification) Dose: 460$\frac{\mu C}{cm^2}$ Dose factor for rings (see Figure): R1 and R2: 1.05, R3: 1.1, R4: 1.2 Developer: AR 600.56:IPA 1:1, 1min Rinse in IPA, 1min
Evap 1	3nm Ti + 50nm Au Lift-off, Acetone at 50°C
Mesa	HMDS wait 20s dry, 5000rpm for 40 s ARU-4060 5000rpm for 40s, 15min at 90°C Note: Do not expose to monitor-light! Expose mesa 30 kV, WD = 10 mm, aperture 10 μm, WF: 81.92 μm, Step Size 10nm (870x magnification) Dose: 300 $\frac{\mu C}{cm^2}$ Reversal bake: 10 minutes at 105C Flood exposure: 25 seconds under UV light (Karl-Suss MJB Mask Aligner) Develop: AR300-26 1:4, 1 min Rinse in water 1min
Mesa etch	Chemical etching: 1:8:500 H2SO4:H2O2:H2O etchant Etch rate: 60 nm/min at T = 25°C Dip in etchant for 1 minute
PECVD	Deposit 100 nm of SiO2 for isolation of bonding pads Note: Cover some area of the substrate with Si wafer for back-gate
Cleaning	NEP 80°C, several hours
Bonding pads	600K 4% 5000 rpm for 40s, 5 mins at 130°C

	950K 3% 6500 rpm 40s, 5 mins at 120°C Expose Bond pad structure 30 kV, WD = 10 mm, aperture 60 μm, WF: 819.2 μm Step size: 2px (87x magnification) Dose: $650\frac{\mu C}{cm^2}$ Developer: AR 600.56:IPA 1:1, 1min Rinse in IPA, 1min
Evap 2	10nm Ti + 120nm Au Lift-off, Acetone 50°C
Backside contacts	ARU-4040 5000rpm for 40s, 2min at 94°C Align on top of n-Si substrate, exposure 14 seconds UV light (Karl-Suss MJB Mask Aligner) Develop: AR300-26 1:4, 1 min Rinse in water 1min
Evap 3	10nm Ti + 120nm Au
Windows	950K 3% 5000 rpm for 40s, 1 mins at 130°C Repeat 2x: 950K 5% 5000 rpm 40s, 10 mins at 130°C Expose resist windows for resist height measurement 30 kV, WD = 10 mm, aperture 30 μm, WF: 81.92 μm Step size: 4px (870x magnification) Dose: $1000\frac{\mu C}{cm^2}$ Developer: AR 600.56:IPA 1:1, 4min During development, put in ultrasonics every 1 minute for 3s Rinse in IPA, 1min
Bridges	Expose bridges (post and span) Post: 30 kV, WD = 10 mm, aperture 10 μm, WF: 81.92 μm Step size: 4px (870x magnification) Dose: $1000\frac{\mu C}{cm^2}$ Span: (see resist height vs voltage chart, must leave at least 200 nm gap between post and span) WD = 10 mm, aperture 10 μm, WF: 81.92 μm Step size: 4px (845x magnification) Dose: $500\frac{\mu C}{cm^2}$ Developer: AR 600.56:IPA 1:1, 4min During development, put in ultrasonics every 1 minute for 3s Rinse in IPA, 1min [Optional] support post (cross-linked PMMA): 30 kV, WD = 10 mm, aperture 10 μm, WF: 81.92 μm Step size: 4px (870x magnification) Dose: $100\frac{\mu C}{cm^2}$, 100 loops

	Developer: AR 600.56:IPA 1:1, 4min During development, put in ultrasonics every 1 minute for 3s Rinse in IPA, 1min
Evap 4	10nm Ti + 420nm Au Lift-off, Acetone at RT overnight

Appendix B

Epitaxial lift-off technique

The epitaxial lift-off technique was used in this work for observing changes in the magneto-transport characteristics in thin film (Ga,Mn)As on different candidate gating substrates and preliminary testing of different barrier materials for future gating experiments. The following table shows the basic steps used in this work for ELO-processing (Ga,Mn)As thin films.

Notes:
Baking is always done on hotplate.
Water is always DI-water with resistance higher than $18M\Omega$cm.
IPA = isopropanol
NEP = N-ethyl-2-pyrrolidon
TCE = Trichloroethylene
MIBK = methyl isobutyl ketone (AR 600.56: MIBK:IPA = 2:3)
Evap = Metal evaporation/deposition
CAIBE = Chemically-Assisted Ion Beam Etching

For the device processing, a photoresist dry etch mask is used since HF etches the STO layer. The ELO-layer, depending on the process, can have gaps wherein the HF can reach and etch-off the barrier layer.

ELO Processing steps	
Cleaning	5 mins acetone ultrasonic bath 5 mins IPA ultrasonic bath Nitrogen gas dry
Apiezon Wax	1 drop of Apiezon:TCE mixture on top of layer 15 minutes dry on air 30 minutes baking at 100° Scrape off with clean scalpel extra Apiezon wax on the side to ensure

	that the etching channel (sacrificial layer) is exposed
HF Dip	1:20 HF:DI H_2O for 8 - 10 hours (i.e. 4mmx4mm sample) Use cryostat bath set at 0°C for etchant cooling. Lift-off, Acetone at 50°C Check every two hours for side-curl If there is no curling of the wax at the side, take out he sample from HF bath and scrape off extra wax. from sides to ensure etch channel exposure
HF removal	One you see freely-floating film with wax: Remove from cryostat and HF bath Dip sample holder in least six beakers with DI H_2O, 1 minute each (rinsing) Catch floating film with new substrate Dry in air for at least 24 hours
Cleaning	Chemical removal of Apiezon wax with TCE After fully removing wax, gently rinse with Acetone and IPA. (no ultrasonic allowed at this point)
Device Processing steps	
Bonding pads	ECI-300 5000rpm for 40s, 2min at 80°C Align on top of lifted-off layer, exposure 7 seconds UV light (Karl-Suss MJB Mask Aligner) Develop: AZ-726, 22s Rinse in water 1min
Evap 1	10nm Ti + 120nm Au Lift-off, Acetone 50°C
Mesa	ECI-300 5000rpm for 40s, 2min at 80°C Align on top of contacts, exposure 7 seconds UV light (Karl-Suss MJB Mask Aligner) Develop: AZ-726, 22s Rinse in water, 1min
Dry etching	CAIBE parameters: Cl_2 gas, 400V, 150W, 25°C Etch rates: Si: 70 nm/min, Ti: 25 nm/min Etch time: 3- 5 minutes Rinse in water for 10 minutes Resist removal: NEP at 80°C for several hours
Backside contacts	ARU-4040 5000rpm for 40s, 2min at 94°C Align on top of n-type substrate, exposure 14 seconds UV light (Karl-Suss MJB Mask Aligner) Develop: AR300-26 1:4, 1 min

	Rinse in water 1min
Evap 2	10nm Ti + 120nm Au Lift-off, Acetone 50°C
Wire	Glue bonding with silver paste mixture Final baking at 130°C for 15 minutes

Bibliography

[Abra 96] E. Abrahams and G. Kotliar. *Science*, Vol. 274, No. 5294, pp. 1853–1854, 1996.

[Ahar 98] A. Aharoni. *Journal of applied physics*, Vol. 83, No. 6, pp. 3432–3434, 1998.

[Bak 80] P. Bak and M. H. Jensen. *Journal of Physics C: Solid State Physics*, Vol. 13, No. 31, p. L881, 1980.

[Baue 12] A. Bauer and C. Pfleiderer. *Phys. Rev. B*, Vol. 85, No. 21, pp. 214418–, 2012.

[Baxt 02] D. V. Baxter, D. Ruzmetov, J. Scherschligt, Y. Sasaki, X. Liu, J. K. Furdyna, and C. H. Mielke. *Phys. Rev. B*, Vol. 65, No. 21, pp. 212407–, 2002.

[Berr 84] M. V. Berry. *Proceedings of the Royal Society of London. A. Mathematical and Physical Sciences*, Vol. 392, No. 1802, pp. 45–57, 1984.

[Binz 06a] B. Binz and A. Vishwanath. *Phys. Rev. B*, Vol. 74, No. 21, pp. 214408–, 2006.

[Binz 06b] B. Binz, A. Vishwanath, and V. Aji. *Phys. Rev. Lett.*, Vol. 96, No. 20, pp. 207202–, 2006.

[Binz 07] B. Binz and A. Vishwanath. *Journal of Magnetism and Magnetic Materials*, Vol. 310, No. 2, Part 2, pp. 1062–1064, 2007.

[Binz 08] B. Binz and A. Vishwanath. *Physica B: Condensed Matter*, Vol. 403, No. 59, pp. 1336–1340, 2008.

[Bogd 01] A. N. Bogdanov and U. K. Rler. *Phys. Rev. Lett.*, Vol. 87, No. 3, pp. 037203–, 2001.

[Bogd 02] A. N. Bogdanov, U. K. Rler, M. Wolf, and K.-H. Mller. *Phys. Rev. B*, Vol. 66, No. 21, pp. 214410–, 2002.

[Bogd 05] A. Bogdanov, U. Rssler, and C. Pfleiderer. *Physica B: Condensed Matter*, Vol. 359361, No. 0, pp. 1162–1164, 2005.

[Bogd 99] A. N. Bogdanov and A. A. Shestakov. *Low Temp. Phys.*, Vol. 25, No. 1, pp. 76–78, 1999.

[Borz 05] T. Borzenko, V. Hock, D. Supp, C. Gould, G. Schmidt, and L. Molenkamp. *Microelectronic Engineering*, Vol. 7879, No. 0, pp. 374–380, 2005.

[Brin 70] W. Brinkman, R. Dynes, and J. Rowell. *Journal of applied physics*, Vol. 41, No. 5, pp. 1915–1921, 1970.

[Bute 10] A. B. Butenko, A. A. Leonov, U. K. Rler, and A. N. Bogdanov. *Phys. Rev. B*, Vol. 82, No. 5, pp. 052403–, 2010.

[Camp 82] I. Campbell and A. Fert. *Vol. 3North-Holland, Amsterdam*, p. 747, 1982.

[Cane 00] C. Canedy, H. Li, S. Alpay, L. Salamanca-Riba, A. Roytburd, and R. Ramesh. *Applied Physics Letters*, Vol. 77, p. 1695, 2000.

[Cham 01] S. Chambers, Y. Liang, Z. Yu, R. Droopad, and J. Ramdani. *Journal of Vacuum Science & Technology A: Vacuum, Surfaces, and Films*, Vol. 19, No. 3, pp. 934–939, 2001.

[Chib 03] D. Chiba, M. Yamanouchi, F. Matsukura, and H. Ohno. *Science*, Vol. 301, No. 5635, pp. 943–945, 2003.

[Chib 04] D. Chiba, Y. Sato, T. Kita, F. Matsukura, and H. Ohno. *Phys. Rev. Lett.*, Vol. 93, No. 21, pp. 216602–, 2004.

[Chib 06a] D. Chiba. *Applied Physics Letters*, Vol. 89, No. 16, pp. 162505–, 2006.

[Chib 06b] D. Chiba, M. Yamanouchi, F. Matsukura, T. Dietl, and H. Ohno. *Phys. Rev. Lett.*, Vol. 96, No. 9, pp. 096602–, 2006.

[Chib 08] D. Chiba, M. Sawicki, Y. Nishitani, Y. Nakatani, F. Matsukura, and H. Ohno. *Nature*, Vol. 455, No. 7212, pp. 515–518, 2008.

[Diet 00] T. Dietl, H. Ohno, F. Matsukura, J. Cibert, and D. Ferrand. *Science*, Vol. 287, No. 5455, pp. 1019–1022, 2000.

[Diet 01a] T. Dietl. *Journal of Applied Physics*, Vol. 89, No. 11, pp. 7437–, 2001.

[Diet 01b] T. Dietl, H. Ohno, and F. Matsukura. *Phys. Rev. B*, Vol. 63, No. 19, pp. 195205–, 2001.

[Diet 08] T. Dietl. *Journal of Applied Physics*, Vol. 103, No. 7, pp. 07D111–, 2008.

[Diet 13] T. Dietl and H. Ohno. *arXiv preprint arXiv:1307.3429*, 2013.

[Duan 08] C.-G. Duan, J. P. Velev, R. F. Sabirianov, W.-N. Mei, S. S. Jaswal, and E. Y. Tsymbal. *Applied Physics Letters*, Vol. 92, No. 12, pp. 122905–122905, 2008.

[Dzya 58] I. Dzyaloshinsky. *Journal of Physics and Chemistry of Solids*, Vol. 4, No. 4, pp. 241–255, 1958.

[Dzya 64] I. Dzyaloshinskii. *Sov. Phys. JETP*, Vol. 19, pp. 960–971, 1964.

[Edmo 02] K. Edmonds. *Applied Physics Letters*, Vol. 81, No. 26, pp. 4991–, 2002.

[Edmo 03] K. Edmonds. *Journal of Applied Physics*, Vol. 93, No. 10, pp. 6787–, 2003.

[Edmo 04] K. W. Edmonds, P. Bogusawski, K. Y. Wang, R. P. Campion, S. N. Novikov, N. R. S. Farley, B. L. Gallagher, C. T. Foxon, M. Sawicki, T. Dietl, M. Buongiorno Nardelli, and J. Bernholc. *Phys. Rev. Lett.*, Vol. 92, No. 3, pp. 037201–, 2004.

[Efro 75] A. Efros and B. Shklovskii. *Journal of Physics C: Solid State Physics*, Vol. 8, No. 4, p. L49, 1975.

[Eise 00] K. Eisenbeiser, J. Finder, Z. Yu, J. Ramdani, J. Curless, J. Hallmark, R. Droopad, W. Ooms, L. Salem, S. Bradshaw, *et al. Applied Physics Letters*, Vol. 76, No. 10, pp. 1324–1326, 2000.

[Eise 02] K. Eisenbeiser, R. Emrick, R. Droopad, Z. Yu, J. Finder, S. Rockwell, J. Holmes, C. Overgaard, and W. Ooms. *Electron Device Letters, IEEE*, Vol. 23, No. 6, pp. 300–302, 2002.

[Enge 12] J. Engelke, T. Reimann, L. Hoffmann, S. Gass, D. Menzel, and S. Süllow. *Journal of the Physical Society of Japan*, Vol. 81, No. 12, p. 124709, 2012.

[Fert 13] A. Fert, V. Cros, and J. Sampaio. *Nat Nano*, Vol. 8, No. 3, pp. 152–156, 2013.

[Frie 06] K.-J. Friedland, M. Bowen, J. Herfort, H. P. Schnherr, and K. H. Ploog. *Journal of Physics: Condensed Matter*, Vol. 18, No. 9, pp. 2641–, 2006.

[Fth 99] M. Fth, S. Freisem, A. A. Menovsky, Y. Tomioka, J. Aarts, and J. A. Mydosh. *Science*, Vol. 285, No. 5433, pp. 1540–1542, 1999.

[Gare 10] R. Gareev, A. Petukhov, M. Schlapps, J. Sadowski, and W. Wegscheider. *Applied Physics Letters*, Vol. 96, No. 5, pp. 052114–052114, 2010.

[Gerb 02] A. Gerber, A. Milner, L. Goldshmit, M. Karpovski, B. Lemke, H.-U. Habermeier, and A. Sulpice. *Physical Review B*, Vol. 65, No. 5, p. 054426, 2002.

[Gira 07] R. Giraud, L. Vila, A. Lemaitre, and G. Faini. *Applied Surface Science*, Vol. 254, No. 1, pp. 343–346, 2007.

[Golo 13] T. Golod, A. Rydh, P. Svedlindh, and V. M. Krasnov. *Phys. Rev. B*, Vol. 87, No. 10, pp. 104407–, 2013.

[Goul 02] C. Gould, G. Schmidt, G. Richter, R. Fiederling, P. Grabs, and L. Molenkamp. *Applied Surface Science*, Vol. 190, No. 1-4, pp. 395–402, 2002.

[Goul 04] C. Gould, C. Rster, T. Jungwirth, E. Girgis, G. M. Schott, R. Giraud, K. Brunner, G. Schmidt, and L. W. Molenkamp. *Phys. Rev. Lett.*, Vol. 93, No. 11, pp. 117203–, 2004.

[Goul 07] C. Gould, K. Pappert, G. Schmidt, and L. Molenkamp. *Adv. Mater.*, Vol. 19, No. 3, pp. 323–340, 2007.

[Goul 08] C. Gould, S. Mark, K. Pappert, R. Dengel, J. Wenisch, R. Campion, A. Rushforth, D. Chiba, Z. Li, X. Liu, *et al. New Journal of Physics*, Vol. 10, No. 5, p. 055007, 2008.

[Greu 11] F. Greullet, L. Ebel, F. Munzhuber, S. Mark, G. Astakhov, T. KieBling, C. Schumacher, C. Gould, K. Brunner, W. Ossau, *et al. Applied Physics Letters*, Vol. 98, No. 23, pp. 231903–231903, 2011.

[Grig 06a] S. V. Grigoriev, S. V. Maleyev, A. I. Okorokov, Y. O. Chetverikov, P. Bni, R. Georgii, D. Lamago, H. Eckerlebe, and K. Pranzas. *Phys. Rev. B*, Vol. 74, No. 21, pp. 214414–, 2006.

[Grig 06b] S. V. Grigoriev, S. V. Maleyev, A. I. Okorokov, Y. O. Chetverikov, and H. Eckerlebe. *Phys. Rev. B*, Vol. 73, No. 22, pp. 224440–, 2006.

[Grig 09] S. V. Grigoriev, D. Chernyshov, V. A. Dyadkin, V. Dmitriev, S. V. Maleyev, E. V. Moskvin, D. Menzel, J. Schoenes, and H. Eckerlebe. *Phys. Rev. Lett.*, Vol. 102, No. 3, pp. 037204–, 2009.

[Grig 10] S. V. Grigoriev, S. V. Maleyev, E. V. Moskvin, V. A. Dyadkin, P. Fouquet, and H. Eckerlebe. *Phys. Rev. B*, Vol. 81, No. 14, pp. 144413–, 2010.

[Heur 03] J. Heurich, J. König, and A. MacDonald. *Physical Review B*, Vol. 68, No. 6, p. 064406, 2003.

[Higg 10] J. M. Higgins, R. Ding, J. P. DeGrave, and S. Jin. *Nano Lett.*, Vol. 10, No. 5, pp. 1605–1610, 2010.

[Hort 07] M. Hortamani, P. Kratzer, and M. Scheffler. *Phys. Rev. B*, Vol. 76, No. 23, pp. 235426–, 2007.

[Hort 08] M. Hortamani, L. Sandratskii, P. Kratzer, I. Mertig, and M. Scheffler. *Phys. Rev. B*, Vol. 78, No. 10, pp. 104402–, 2008.

[Huan 06] Y. S. Huang, C. C. Wang, and A. O. Adeyeye. *J. Appl. Phys.*, Vol. 100, No. 1, pp. 013909–4, 2006.

[Hugh 96] R. J. F. Hughes, A. K. Savchenko, J. E. F. Frost, E. H. Linfield, J. T. Nicholls, M. Pepper, E. Kogan, and M. Kaveh. *Phys. Rev. B*, Vol. 54, No. 3, pp. 2091–2100, 1996.

[Hump 07] S. Humpfner, K. Pappert, J. Wenisch, K. Brunner, C. Gould, G. Schmidt, L. Molenkamp, M. Sawicki, and T. Dietl. *Applied Physics Letters*, Vol. 90, No. 10, pp. 102102–102102, 2007.

[Hurd 72] C. M. Hurd. *The Hall effect in metals and alloys.* Plenum Press New York, 1972.

[Ishi 77] Y. Ishikawa, G. Shirane, J. A. Tarvin, and M. Kohgi. *Phys. Rev. B*, Vol. 16, No. 11, pp. 4956–4970, 1977.

[Ishi 85] M. Ishida, Y. Endoh, S. Mitsuda, Y. Ishikawa, and M. Tanaka. *Journal of the Physical Society of Japan*, Vol. 54, No. 8, pp. 2975–2982, 1985.

[Jan 57] J.-P. Jan. *Solid State Physics*, Vol. 5, pp. 1–96, 1957.

[Jeon 04] T. Jeong and W. E. Pickett. *Phys. Rev. B*, Vol. 70, No. 7, pp. 075114–, 2004.

[Joni 10] F. Jonietz, S. Mhlbauer, C. Pfleiderer, A. Neubauer, W. Mnzer, A. Bauer, T. Adams, R. Georgii, P. Bni, R. A. Duine, K. Everschor, M. Garst, and A. Rosch. *Science*, Vol. 330, No. 6011, pp. 1648–1651, 2010.

[Jung 06] T. Jungwirth, J. Sinova, J. Maek, J. Ku?era, and A. H. MacDonald. *Rev. Mod. Phys.*, Vol. 78, No. 3, pp. 809–, 2006.

[Kami 02] A. Kaminski and S. Das Sarma. *Phys. Rev. Lett.*, Vol. 88, No. 24, pp. 247202–, 2002.

[Kami 03] A. Kaminski and S. Das Sarma. *Phys. Rev. B*, Vol. 68, No. 23, pp. 235210–, 2003.

[Karh 10] E. Karhu, S. Kahwaji, T. L. Monchesky, C. Parsons, M. D. Robertson, and C. Maunders. *Phys. Rev. B*, Vol. 82, No. 18, pp. 184417–, 2010.

[Karh 11] E. A. Karhu, S. Kahwaji, M. D. Robertson, H. Fritzsche, B. J. Kirby, C. F. Majkrzak, and T. L. Monchesky. *Phys. Rev. B*, Vol. 84, No. 6, pp. 060404–, 2011.

[Karh 12] E. A. Karhu, U. K. Rler, A. N. Bogdanov, S. Kahwaji, B. J. Kirby, H. Fritzsche, M. D. Robertson, C. F. Majkrzak, and T. L. Monchesky. *Phys. Rev. B*, Vol. 85, No. 9, pp. 094429–, 2012.

[Kasu 59] T. Kasuya. *Progress of theoretical physics*, Vol. 22, No. 2, pp. 227–246, 1959.

[Kona 78] M. Konagai, M. Sugimoto, and K. Takahashi. *Journal of crystal growth*, Vol. 45, pp. 277–280, 1978.

[Lee 07] M. Lee, Y. Onose, Y. Tokura, and N. P. Ong. *Phys. Rev. B*, Vol. 75, No. 17, pp. 172403–, 2007.

[Lee 09] M. Lee, W. Kang, Y. Onose, Y. Tokura, and N. P. Ong. *Phys. Rev. Lett.*, Vol. 102, No. 18, pp. 186601–, 2009.

[Lee 85] P. A. Lee and T. Ramakrishnan. *Reviews of Modern Physics*, Vol. 57, No. 2, p. 287, 1985.

[Li 07] A. P. Li, C. Zeng, K. van Benthem, M. F. Chisholm, J. Shen, S. V. S. Nageswara Rao, S. K. Dixit, L. C. Feldman, A. G. Petukhov, M. Foygel, and H. H. Weitering. *Phys. Rev. B*, Vol. 75, No. 20, pp. 201201–, 2007.

[Li 13] Y. Li, N. Kanazawa, X. Z. Yu, A. Tsukazaki, M. Kawasaki, M. Ichikawa, X. F. Jin, F. Kagawa, and Y. Tokura. *Phys. Rev. Lett.*, Vol. 110, No. 11, pp. 117202–, 2013.

[Lin 10] Y.-C. Lin, Y. Chen, A. Shailos, and Y. Huang. *Nano Lett.*, Vol. 10, No. 6, pp. 2281–2287, 2010.

[MacD 05] A. MacDonald, P. Schiffer, and N. Samarth. *Nature Materials*, Vol. 4, No. 3, pp. 195–202, 2005.

[Mach 10] Y. Machida, S. Nakatsuji, S. Onoda, T. Tayama, and T. Sakakibara. *Nature*, Vol. 463, No. 7278, pp. 210–213, 2010.

[Magn 10] E. Magnano, F. Bondino, C. Cepek, F. Parmigiani, and M. C. Mozzati. *Appl. Phys. Lett.*, Vol. 96, No. 15, pp. 152503–3, 2010.

[Mark 11] S. Mark, P. Dürrenfeld, K. Pappert, L. Ebel, K. Brunner, C. Gould, and L. Molenkamp. *Physical Review Letters*, Vol. 106, No. 5, p. 057204, 2011.

[Mats 04] F. Matsukura, M. Sawicki, T. Dietl, D. Chiba, and H. Ohno. *Physica E: Low-dimensional Systems and Nanostructures*, Vol. 21, No. 2-4, pp. 1032–1036, 2004.

[Mats 98] F. Matsukura, H. Ohno, A. Shen, and Y. Sugawara. *Phys. Rev. B*, Vol. 57, No. 4, pp. R2037–, 1998.

[McGu 75] T. McGuire and R. Potter. *Magnetics, IEEE Transactions on*, Vol. 11, No. 4, pp. 1018–1038, 1975.

[Mena 03] F. P. Mena, D. van der Marel, A. Damascelli, M. Fth, A. A. Menovsky, and J. A. Mydosh. *Phys. Rev. B*, Vol. 67, No. 24, pp. 241101–, 2003.

[Mori 60] T. Moriya. *Phys. Rev.*, Vol. 120, No. 1, pp. 91–98, 1960.

[Mori 76] T. Moriya. *Solid State Communications*, Vol. 20, No. 3, pp. 291–294, 1976.

[Mori 79] T. Moriya. *Journal of Magnetism and Magnetic Materials*, Vol. 14, No. 1, pp. 1–46, 1979.

[Mori 85] T. Moriya. *Springer series in solid-state sciences*, Vol. 56, 1985.

[Mott 67] N. Mott. *Advances in Physics*, Vol. 16, No. 61, pp. 49–144, 1967.

[Mott 68a] N. F. Mott. *Philosophical Magazine*, Vol. 17, No. 150, pp. 1259–1268, 1968.

[Mott 68b] N. F. Mott. *Rev. Mod. Phys.*, Vol. 40, No. 4, pp. 677–, 1968.

[Mott 72] N. Mott. *Advances in Physics*, Vol. 21, No. 94, pp. 785–823, 1972.

[Mott 76] N. F. Mott. *Philosophical Magazine*, Vol. 34, No. 4, pp. 643–645, 1976.

[Mudu 05] P. K. Muduli, K.-J. Friedland, J. Herfort, H.-P. Schnherr, and K. H. Ploog. *Phys. Rev. B*, Vol. 72, No. 10, pp. 104430–, 2005.

[Mueh 09] S. Muehlbauer, B. Binz, F. Jonietz, C. Pfleiderer, A. Rosch, A. Neubauer, R. Georgii, and P. Bni. *Science*, Vol. 323, No. 5916, pp. 915–919, 2009.

[Mull 04] D. A. Muller, N. Nakagawa, A. Ohtomo, J. L. Grazul, and H. Y. Hwang. *Nature*, Vol. 430, No. 7000, pp. 657–661, 2004.

[Mull 79] K. Müller and H. Burkard. *Physical Review B*, Vol. 19, No. 7, p. 3593, 1979.

[Naga 10] N. Nagaosa, J. Sinova, S. Onoda, A. H. MacDonald, and N. P. Ong. *Rev. Mod. Phys.*, Vol. 82, No. 2, pp. 1539–1592, 2010.

[Naka 80] O. Nakanishi, A. Yanase, A. Hasegawa, and M. Kataoka. *Solid State Communications*, Vol. 35, No. 12, pp. 995–998, 1980.

[Neub 09a] A. Neubauer, C. Pfleiderer, B. Binz, A. Rosch, R. Ritz, P. G. Niklowitz, and P. Bni. *Phys. Rev. Lett.*, Vol. 102, No. 18, pp. 186602–, 2009.

[Neub 09b] A. Neubauer, C. Pfleiderer, R. Ritz, P. Niklowitz, and P. Bni. *Physica B: Condensed Matter*, Vol. 404, No. 19, pp. 3163–3166, 2009.

[Ohno 00] H. Ohno, D. Chiba, F. Matsukura, T. Omiya, E. Abe, T. Dietl, Y. Ohno, and K. Ohtani. *Nature*, Vol. 408, No. 6815, pp. 944–946, 2000.

[Ohno 96] H. Ohno. *Applied Physics Letters*, Vol. 69, No. 3, pp. 363–, 1996.

[Olej 08] K. Olejnk, M. H. S. Owen, V. Novk, J. Maek, A. C. Irvine, J. Wunderlich, and T. Jungwirth. *Phys. Rev. B*, Vol. 78, No. 5, pp. 054403–, 2008.

[Onsa 31a] L. Onsager. *Phys. Rev.*, Vol. 37, No. 4, pp. 405–426, 1931.

[Onsa 31b] L. Onsager. *Phys. Rev.*, Vol. 38, No. 12, pp. 2265–2279, 1931.

[Owen 09] M. Owen, J. Wunderlich, V. Novák, K. Olejník, J. Zemen, K. Vỳbornỳ, S. Ogawa, A. Irvine, A. Ferguson, H. Sirringhaus, *et al. New journal of Physics*, Vol. 11, No. 2, p. 023008, 2009.

[Papp 06] K. Pappert, M. J. Schmidt, S. Hmpfner, C. Rster, G. M. Schott, K. Brunner, C. Gould, G. Schmidt, and L. W. Molenkamp. *Phys. Rev. Lett.*, Vol. 97, No. 18, pp. 186402–, 2006.

[Papp 07a] K. Pappert. *Applied Physics Letters*, Vol. 90, No. 6, pp. 062109–, 2007.

[Papp 07b] K. Pappert, C. Gould, M. Sawicki, J. Wenisch, K. Brunner, G. Schmidt, and L. Molenkamp. *New Journal of Physics*, Vol. 9, No. 9, p. 354, 2007.

[Papp 07c] K. Pappert, S. Humpfner, C. Gould, J. Wenisch, K. Brunner, G. Schmidt, and L. W. Molenkamp. *Nat Phys*, Vol. 3, No. 8, pp. 573–578, 2007.

[Papp 09] C. Pappas, E. Lelivre-Berna, P. Falus, P. M. Bentley, E. Moskvin, S. Grigoriev, P. Fouquet, and B. Farago. *Phys. Rev. Lett.*, Vol. 102, No. 19, pp. 197202–, 2009.

[Petr 06] A. E. Petrova, E. D. Bauer, V. Krasnorussky, and S. M. Stishov. *Phys. Rev. B*, Vol. 74, No. 9, pp. 092401–, 2006.

[Petr 11] A. E. Petrova, V. N. Krasnorussky, W. M. Yuhasz, T. A. Lograsso, and S. M. Stishov. *Journal of Physics: Conference Series*, Vol. 273, No. 1, pp. 012056–, 2011.

[Pfle 01] C. Pfleiderer, S. R. Julian, and G. G. Lonzarich. *Nature*, Vol. 414, No. 6862, pp. 427–430, 2001.

[Pfle 04] C. Pfleiderer, D. Reznik, L. Pintschovius, H. v. Löhneysen, M. Garst, and A. Rosch. *Nature*, Vol. 427, No. 6971, pp. 227–231, 2004.

[Pfle 09] C. Pfleiderer, A. Neubauer, S. Mhlbauer, F. Jonietz, M. Janoschek, S. Legl, R. Ritz, W. Mnzer, C. Franz, P. G. Niklowitz, T. Keller, R. Georgii, P. Bni, B. Binz, A. Rosch, U. K. Rler, and A. N. Bogdanov. *Journal of Physics: Condensed Matter*, Vol. 21, No. 16, pp. 164215–, 2009.

[Pfle 10a] C. Pfleiderer, T. Adams, A. Bauer, W. Biberacher, B. Binz, F. Birkelbach, P. Bni, C. Franz, R. Georgii, M. Janoschek, F. Jonietz, T. Keller, R. Ritz, S. Mhlbauer, W. Mnzer, A. Neubauer, B. Pedersen, and A. Rosch. *Journal of Physics: Condensed Matter*, Vol. 22, No. 16, pp. 164207–, 2010.

[Pfle 10b] C. Pfleiderer and A. Rosch. *Nature*, Vol. 465, No. 7300, pp. 880–881, 2010.

[Pisk 04] S. Piskunov, E. Heifets, R. Eglitis, and G. Borstel. *Computational Materials Science*, Vol. 29, No. 2, pp. 165–178, 2004.

[Plum 81] M. L. Plumer and M. B. Walker. *Journal of Physics C: Solid State Physics*, Vol. 14, No. 31, pp. 4689–, 1981.

[Plum 82] M. L. Plumer and M. B. Walker. *Journal of Physics C: Solid State Physics*, Vol. 15, No. 35, pp. 7181–, 1982.

[Pohl 13] C. Pohl. *Silicon Based MBE of Manganese-Silicide and Silicon-Suboxide*. PhD thesis, Wu?rzburg, Universita?t Wu?rzburg, Diss., 2013, 2013.

[Popo 90] D. Popović, A. Fowler, S. Washburn, and P. Stiles. *Physical Review B*, Vol. 42, No. 3, p. 1759, 1990.

[Raik 87] M. Raikh and I. Ruzin. *Zh. Eksp. Teor. Fiz*, Vol. 92, pp. 2257–2276, 1987.

[Reag 05] D. W. Reagor and V. Y. Butko. *Nature Materials*, Vol. 4, No. 8, pp. 593–596, 2005.

[Rich 10] A. Richardella, P. Roushan, S. Mack, B. Zhou, D. A. Huse, D. D. Awschalom, and A. Yazdani. *Science*, Vol. 327, No. 5966, pp. 665–669, 2010.

[Rikk 05] G. L. J. A. Rikken and P. Wyder. *Phys. Rev. Lett.*, Vol. 94, No. 1, pp. 016601–, 2005.

[Ritz 13a] R. Ritz, M. Halder, C. Franz, A. Bauer, M. Wagner, R. Bamler, A. Rosch, and C. Pfleiderer. *Phys. Rev. B*, Vol. 87, No. 13, pp. 134424–, 2013.

[Ritz 13b] R. Ritz, M. Halder, M. Wagner, C. Franz, A. Bauer, and C. Pfleiderer. *Nature*, Vol. 497, No. 7448, pp. 231–234, 2013.

[Rler 10] U. K. Rler, A. A. Leonov, and A. N. Bogdanov. *Journal of Physics: Conference Series*, Vol. 200, No. 2, pp. 022029–, 2010.

[Robe 02] J. Robertson. *Applied surface science*, Vol. 190, No. 1, pp. 2–10, 2002.

[Robe 06] J. Robertson. *Reports on Progress in Physics*, Vol. 69, No. 2, p. 327, 2006.

[Roes 11] U. K. Roessler, A. A. Leonov, and A. N. Bogdanov. *Journal of Physics: Conference Series*, Vol. 303, No. 1, pp. 012105–, 2011.

[Romm 13] N. Romming, C. Hanneken, M. Menzel, J. E. Bickel, B. Wolter, K. von Bergmann, A. Kubetzka, and R. Wiesendanger. *Science*, Vol. 341, No. 6146, pp. 636–639, 2013.

[Rose 83] T. F. Rosenbaum, R. F. Milligan, M. A. Paalanen, G. A. Thomas, R. N. Bhatt, and W. Lin. *Phys. Rev. B*, Vol. 27, No. 12, pp. 7509–, 1983.

[Rste 05] C. Rster. *Journal of Applied Physics*, Vol. 97, No. 10, pp. 10C506–, 2005.

[Rush 06] A. W. Rushforth, A. D. Giddings, K. W. Edmonds, R. P. Campion, C. T. Foxon, and B. L. Gallagher. *Phys. Status Solidi (c)*, Vol. 3, No. 12, pp. 4078–4081, 2006.

[Rush 07] A. W. Rushforth, K. Vborn, C. S. King, K. W. Edmonds, R. P. Campion, C. T. Foxon, J. Wunderlich, A. C. Irvine, P. Vaek, V. Novk, K. Olejnk, J. Sinova, T. Jungwirth, and B. L. Gallagher. *Phys. Rev. Lett.*, Vol. 99, No. 14, pp. 147207–, 2007.

[Rush 09] A. Rushforth, K. Vborn, C. King, K. Edmonds, R. Campion, C. Foxon, J. Wunderlich, A. Irvine, V. Novk, K. Olejnk, A. Kovalev, J. Sinova, T. Jungwirth, and B. Gallagher. *Journal of Magnetism and Magnetic Materials*, Vol. 321, No. 8, pp. 1001–1008, 2009.

[Sawi 04] M. Sawicki, F. Matsukura, A. Idziaszek, T. Dietl, G. M. Schott, C. Ruester, C. Gould, G. Karczewski, G. Schmidt, and L. W. Molenkamp. *Phys. Rev. B*, Vol. 70, No. 24, pp. 245325–, 2004.

[Sawi 05] M. Sawicki, K.-Y. Wang, K. W. Edmonds, R. P. Campion, C. R. Staddon, N. R. S. Farley, C. T. Foxon, E. Papis, E. Kamiska, A. Piotrowska, T. Dietl, and B. L. Gallagher. *Phys. Rev. B*, Vol. 71, No. 12, pp. 121302–, 2005.

[Sawi 10] M. Sawicki, D. Chiba, A. Korbecka, Y. Nishitani, J. A. Majewski, F. Matsukura, T. Dietl, and H. Ohno. *Nat Phys*, Vol. 6, No. 1, pp. 22–25, 2010.

[Schm 07] M. J. Schmidt, K. Pappert, C. Gould, G. Schmidt, R. Oppermann, and L. W. Molenkamp. *Phys. Rev. B*, Vol. 76, No. 3, pp. 035204–, 2007.

[Schu 12] T. Schulz, R. Ritz, A. Bauer, M. Halder, M. Wagner, C. Franz, C. Pfleiderer, K. Everschor, M. Garst, and A. Rosch. *Nat Phys*, Vol. 8, No. 4, pp. 301–304, 2012.

[Seki 12] S. Seki, X. Z. Yu, S. Ishiwata, and Y. Tokura. *Science*, Vol. 336, No. 6078, pp. 198–201, 2012.

[Seo 10] K. Seo, H. Yoon, S.-W. Ryu, S. Lee, Y. Jo, M.-H. Jung, J. Kim, Y.-K. Choi, and B. Kim. *ACS Nano*, Vol. 4, No. 5, pp. 2569–2576, 2010.

[Sheu 07] B. L. Sheu, R. C. Myers, J.-M. Tang, N. Samarth, D. D. Awschalom, P. Schiffer, and M. E. Flatt. *Phys. Rev. Lett.*, Vol. 99, No. 22, pp. 227205–, 2007.

[Shio 12] Y. Shiomi, S. Iguchi, and Y. Tokura. *Phys. Rev. B*, Vol. 86, No. 18, pp. 180404–, 2012.

[Shio 13] Y. Shiomi, N. Kanazawa, K. Shibata, Y. Onose, and Y. Tokura. *Phys. Rev. B*, Vol. 88, No. 6, pp. 064409–, 2013.

[Shkl 79] B. I. Shklovskii and A. L. Efros. *Moscow Izdatel Nauka*, Vol. 1, 1979.

[Skyr 62] T. Skyrme. *Nuclear Physics*, Vol. 31, No. 0, pp. 556–569, 1962.

[Suto 09] H. Suto, K. Imai, S. Fujii, S.-i. Honda, and M. Katayama. *Surface Science*, Vol. 603, No. 1, pp. 226–231, 2009.

[Suzu 00] T. Suzuki, Y. Nishi, and M. Fujimoto. *Philosophical Magazine A*, Vol. 80, No. 3, pp. 621–637, 2000.

[Tagu 09] K. Taguchi and G. Tatara. *Phys. Rev. B*, Vol. 79, No. 5, pp. 054423–, 2009.

[Tana 85] M. Tanaka, H. Takayoshi, M. Ishida, and Y. Endoh. *Journal of the Physical Society of Japan*, Vol. 54, No. 8, pp. 2970–2974, 1985.

[Tata 02] G. Tatara and H. Kawamura. *Journal of the Physical Society of Japan*, Vol. 71, No. 11, pp. 2613–2616, 2002.

[Thou 74] D. Thouless. *Physics Reports*, Vol. 13, No. 3, pp. 93–142, 1974.

[Tono 12] A. Tonomura, X. Yu, K. Yanagisawa, T. Matsuda, Y. Onose, N. Kanazawa, H. S. Park, and Y. Tokura. *Nano Lett.*, Vol. 12, No. 3, pp. 1673–1677, 2012.

[Vila 07] L. Vila, R. Giraud, L. Thevenard, A. Lemaître, F. Pierre, J. Dufouleur, D. Mailly, B. Barbara, and G. Faini. *Physical review letters*, Vol. 98, No. 2, p. 027204, 2007.

[Vonc 02] M. Voncken, J. Schermer, G. Maduro, G. Bauhuis, P. Mulder, and P. Larsen. *Materials Science and Engineering: B*, Vol. 95, No. 3, pp. 242–248, 2002.

[Webb 86] R. Webb, A. Fowler, A. Hartstein, and J. Wainer. *Surface Science*, Vol. 170, No. 1-2, pp. 14–27, 1986.

[Weni 07] J. Wenisch, C. Gould, L. Ebel, J. Storz, K. Pappert, M. J. Schmidt, C. Kumpf, G. Schmidt, K. Brunner, and L. W. Molenkamp. *Phys. Rev. Lett.*, Vol. 99, No. 7, pp. 077201–, 2007.

[Wies 77] H. Wiesmann, M. Gurvitch, H. Lutz, A. Ghosh, B. Schwarz, M. Strongin, P. B. Allen, and J. W. Halley. *Phys. Rev. Lett.*, Vol. 38, No. 14, pp. 782–785, 1977.

[Wils 12] M. N. Wilson, E. A. Karhu, A. S. Quigley, U. K. Rler, A. B. Butenko, A. N. Bogdanov, M. D. Robertson, and T. L. Monchesky. *Phys. Rev. B*, Vol. 86, No. 14, pp. 144420–, 2012.

[Wils 13] M. Wilson, E. Karhu, D. Lake, A. Quigley, A. Bogdanov, U. Rößler, and T. Monchesky. *arXiv preprint arXiv:1305.5196*, 2013.

[Wind 12] Y. W. Windsor, A. Gerber, and M. Karpovski. *Phys. Rev. B*, Vol. 85, No. 6, pp. 064409–, 2012.

[Wolf 12] E. L. Wolf. *Principles of electron tunneling spectroscopy*. Vol. 152, Oxford University Press, 2012.

[Xu 09] Q. Xu, S. Zhou, B. Schmidt, A. Mcklich, and H. Schmidt. *Nuclear Instruments and Methods in Physics Research Section B: Beam Interactions with Materials and Atoms*, Vol. 267, No. 2122, pp. 3558–3561, 2009.

[Yabl 87] E. Yablonovitch, T. Gmitter, J. Harbison, and R. Bhat. *Applied Physics Letters*, Vol. 51, p. 2222, 1987.

[Yabl 90] E. Yablonovitch, D. Hwang, T. Gmitter, L. Florez, and J. Harbison. *Applied physics letters*, Vol. 56, No. 24, pp. 2419–2421, 1990.

[Yi 09] S. D. Yi, S. Onoda, N. Nagaosa, and J. H. Han. *Phys. Rev. B*, Vol. 80, No. 5, pp. 054416–, 2009.

[Yu 02] K. M. Yu, W. Walukiewicz, T. Wojtowicz, I. Kuryliszyn, X. Liu, Y. Sasaki, and J. K. Furdyna. *Phys. Rev. B*, Vol. 65, No. 20, pp. 201303–, 2002.

[Yu 10] X. Z. Yu, Y. Onose, N. Kanazawa, J. H. Park, J. H. Han, Y. Matsui, N. Nagaosa, and Y. Tokura. *Nature*, Vol. 465, No. 7300, pp. 901–904, 2010.

[Yu 11] X. Z. Yu, N. Kanazawa, Y. Onose, K. Kimoto, W. Z. Zhang, S. Ishiwata, Y. Matsui, and Y. Tokura. *Nat Mater*, Vol. 10, No. 2, pp. 106–109, 2011.

[Yu 12] X. Yu, M. Mostovoy, Y. Tokunaga, W. Zhang, K. Kimoto, Y. Matsui, Y. Kaneko, N. Nagaosa, and Y. Tokura. *Proceedings of the National Academy of Sciences*, Vol. 109, No. 23, pp. 8856–8860, 2012.

[Yu 13] X. Yu, J. P. DeGrave, Y. Hara, T. Hara, S. Jin, and Y. Tokura. *Nano Lett.*, Vol. 13, No. 8, pp. 3755–3759, 2013.

[Zeng 08] L. Zeng, E. Helgren, M. Rahimi, F. Hellman, R. Islam, B. Wilkens, R. Culbertson, and D. J. Smith. *Physical Review B*, Vol. 77, No. 7, p. 073306, 2008.

[Zhan 02] Q. Zhang, M. Tanaka, M. Takeguchi, and K. Furuya. *Surface science*, Vol. 507, pp. 453–457, 2002.

Acknowledgements

- First of all I would like to express my gratitude to Prof. Dr. Laurens W. Molenkamp the head of the EP3 chair and the spintronics group for giving me the opportunity to work in his group.

  I also want to especially thank the following groups of people:

  • PD Dr. Charles Gould for allowing me to work as part of his team and for the helpful corrections and suggestions for this thesis. Prof. Dr. Matthias Bode and Prof. Dr. Reinhold Oppermann for agreeing to be my Gutachters in such short notice and their help with this thesis. The Faculty for accelerating the process due to my numerous visa issues.
  • The C113 people: Dr. Fanny Greullet, Tsvetelina Naydenova, Marjan Samiepour, Thomas Wagner and honorary office mate Shijin Babu - thank you very much for the good memories and the enormous help during experiments, in doing data analysis and trying to relax.
  • The C114a people: Dr. Stefan Mark, Philip Hartmann, Dr. Michael Rüth, Gabriel Radu-Dengel and Thorsten Kloß, thank you very much for your kindness and help during experiments.
  • MBE guys Dr. Lars Ebel for growing the (Ga,Mn)As wafers and Dr. Christoph Pohl for the MnSi thin films. Florian Pfaff and from EP4 and his students for the PLD STO growth and Dr. Michael Sing and Prof. Dr. Ralph Claessen for allowing me to use their samples. Dr. Bastian Büttner, Philipp Dürrenfeld, Philip Hartmann, Fabian Dürr and Oliver Hermann for the help in translating some parts of this thesis. Thanks to Tanja Borzenko and Volkmar Hock for all the help and answering my questions during device fabrication.
  • To everybody else in EP3, thanks for your kindness to a stranger in a strange land.
  • I also would like to gratefully acknowledge the opportunity provided to me by the European Commission through the Marie Curie Program FP7 as an Early Stage Researcher.
  • To my family, who are always patiently waiting for me to stop this nonsense and come home.
  • Last but not the least, I would like to thank whatever higher power put me here, because this experience made me realize what is truly important in life.